

# POLITECNICO DI MILANO

Facoltà di Ingegneria Industriale

Corso di Laurea in  
Ingegneria Spaziale



## Preliminary Study on a Vibration Suppression System for a Large Flexible Space Structure

Relatore: Prof. Michéle LAVAGNA

Tesi di Laurea di:

Alessandro DIPAOLA Matr. 735267

Dario DONATIELLO Matr. 725548

Anno Accademico 2011-2012



# Abstract

The subject of the present thesis is a preliminary analysis of the vibrational issues of a large flexible structure, that can represent the skeleton structure of a wide class of Space Solar Power (SSP) satellites. Due to the huge dimensions of such structures, their first natural frequencies turn out to be far lower than those of the common satellites and a significant control-structure interaction issue may arise. Even though the orbital and attitude control systems may be designed to be low bandwidth regulators, particular operative conditions could excite the lowest structural modes. Once excited, providing a mean to extinguish the vibrations appear to be appropriate, in order to guarantee the oscillations to be damped. In this context, the objective of this work is to study the interactions between the orbital/attitude control systems and the flexible structure. Hence, an orbital/attitude control system is designed in order to satisfy prescribed requirements related to station keeping and pointing of such a class of spacecraft. Furthermore, a possible approach in developing a preliminary vibration suppression system is carried out, referring to the class of the direct output feedback controllers, utilizing properly distributed ion thrusters. It is shown that, considering the developed orbital/attitude controllers, there exists considerable interaction problems during the operative life of the spacecraft. Eventually, the proposed vibration suppression system is proved to be able to considerably mitigate the effects of these, potentially dangerous, interactions.

**Keywords** Space Solar Power satellites. Control of large flexible structure. Direct output feedback control. Collocated control. Geostationary satellite station keeping. Attitude control.

# Sommario

Oggetto del presente lavoro è l'analisi preliminare delle problematiche legate alle vibrazioni di una grande struttura flessibile atta a rappresentare la struttura portante di una vasta classe di Space Solar Power (SSP) satellites. A causa delle enormi dimensioni di tali strutture, le loro prime frequenze naturali risultano essere di gran lunga inferiori a quelle dei satelliti comuni, facendo sì che possa sorgere un significativo problema di interazione tra controllo e struttura. Benché i sistemi di controllo d'orbita e d'assetto possano essere progettati in modo tale da avere una banda passante molto bassa, particolari condizioni operative, potrebbero eccitare i modi di vibrare a più bassa frequenza. Risulta dunque indicato, in questa situazione, fornire uno strumento per smorzare le vibrazioni strutturali. In questo contesto, l'obiettivo della tesi è quello di studiare l'interazione tra i sistemi di controllo orbitale e d'assetto e la struttura flessibile. Pertanto, è stato progettato un sistema di controllo d'orbita e d'assetto in grado di soddisfare i requisiti imposti sulla posizione e sul puntamento del satellite. Inoltre è proposto lo sviluppo preliminare di un sistema di soppressione delle vibrazioni, basandosi sulla classe dei controllori a retroazione diretta dell'uscita e utilizzando propulsori a bassa spinta propriamente distribuiti. Si dimostra che, nell'ipotesi di impiegare i regolatori progettati, possano sorgere significativi problemi di interazione durante la vita operativa del satellite. Infine, si verifica come il sistema di soppressione delle vibrazioni proposto, sia in grado di mitigare gli effetti, potenzialmente pericolosi, di tali interazioni.

**Parole chiave** Space Solar Power satellites. Controllo di grandi strutture flessibili. Controllo subottimo. Controllo collocato. Mantenimento di satelliti geostazionari. Controllo d'assetto.

# Contents

<b>1</b>	<b>Introduction</b>	<b>2</b>
1.1	Reasons For The SSP Research . . . . .	2
1.2	Design Concepts . . . . .	3
1.2.1	The Sun Tower Satellite . . . . .	3
1.2.2	The Tethered Solar Power Satellite . . . . .	4
1.2.3	The Abacus Reflector . . . . .	5
1.3	Rationale for a Structural Vibration-Suppression System . . . . .	7
1.4	Thesis Structure . . . . .	9
<b>2</b>	<b>Orbital Dynamics and Control</b>	<b>11</b>
2.1	Time Measure . . . . .	11
2.1.1	Sidereal Time and Universal Time . . . . .	11
2.1.2	Epoch and Calendar Date . . . . .	12
2.2	Reference Frames and Coordinate Systems . . . . .	13
2.2.1	Earth Centered Inertial Reference Frame and Coordinate System (RFCS) . . . . .	13
2.2.2	Earth Centered Earth Fixed RFCS . . . . .	14
2.2.3	Gaussian RFCS . . . . .	14
2.2.4	Geostationary Clohessy-Wiltshire RFCS . . . . .	14
2.3	Satellite State Representation . . . . .	17
2.3.1	Position and Velocity . . . . .	17
2.3.2	Classical Orbital Elements . . . . .	18
2.3.3	Equinoctial Orbital Elements . . . . .	20
2.4	Environmental Perturbations . . . . .	21
2.4.1	Earth's Gravitational Field . . . . .	22
2.4.2	Gravity Attraction of the Sun and the Moon . . . . .	24
2.4.3	Solar Radiation Pressure . . . . .	25
2.5	Translational Dynamics of GEO Satellites . . . . .	28
2.5.1	Non-Linear Geostationary Orbit Model . . . . .	29
2.5.2	A Linearised Geostationary Orbit Model . . . . .	30
2.6	GEO Satellite Station Keeping . . . . .	32

2.6.1	GEO Satellite Orbital Requirements . . . . .	32
2.6.2	Orbit Control System . . . . .	33
<b>3</b>	<b>Attitude dynamics</b>	<b>40</b>
3.1	Reference Frames and Coordinate Systems . . . . .	40
3.2	Attitude configurations . . . . .	41
3.2.1	Attitude Dynamics Requirements . . . . .	42
3.2.2	The Sun Pointing (SP) Configuration . . . . .	42
3.2.3	The Sun Facing (SF) Configuration . . . . .	42
3.2.4	The Transmitting Pointing Configurations . . . . .	43
3.3	Attitude State Representation . . . . .	43
3.4	Environmental Disturbances . . . . .	45
3.4.1	The Gravity Gradient Torque . . . . .	46
3.4.2	The Solar Radiation Torque . . . . .	46
3.5	Attitude Uncontrolled Motion . . . . .	47
3.6	Attitude Control Regulators . . . . .	47
3.6.1	Proportional Integrative Derivative Regulator . . . . .	47
3.6.2	Optimal Linear Quadratic Regulator . . . . .	48
3.6.3	Cyclic Disturbance Rejection . . . . .	49
3.7	Attitude Control System . . . . .	49
3.7.1	The Attitude Zero Initial Condition (AZIC) . . . . .	50
3.7.2	Attitude Perturbed Initial Condition (APIC) . . . . .	52
<b>4</b>	<b>Structural Model</b>	<b>54</b>
4.1	Finite Element Model . . . . .	54
4.1.1	The Bidimensional Reference Configuration . . . . .	54
4.1.2	The Structural Reference Systems . . . . .	55
4.1.3	The Finite Element Model . . . . .	56
4.1.4	Dynamic Problem . . . . .	57
4.1.5	Global Degrees of Freedom . . . . .	58
4.1.6	Structural Model Comparison . . . . .	61
4.2	State-Space Realization . . . . .	65
<b>5</b>	<b>Model reduction</b>	<b>66</b>
5.1	Preliminary Concepts . . . . .	66
5.2	Model Reduction by Truncation . . . . .	67
5.2.1	Minimal Transfer Equivalent Realization . . . . .	68
5.2.2	Modal Truncation . . . . .	69
5.2.3	Singular Perturbation Approximation . . . . .	70
5.2.4	Matching Frequency and Power Moments . . . . .	71
5.2.5	Balanced Truncation . . . . .	73

## CONTENTS

---

5.3	Application of the Reduction Algorithms . . . . .	74
<b>6</b>	<b>Vibration Suppression System</b>	<b>80</b>
6.1	Linear Output Feedback Control . . . . .	80
6.1.1	Stability Analysis . . . . .	81
6.1.2	Stability Robustness Analysis . . . . .	82
6.2	Unstructured Suboptimal Control . . . . .	83
6.2.1	Gain Matrix Computation Algorithm . . . . .	84
6.3	Simulation results . . . . .	85
6.3.1	Unstructured Suboptimal Regulator . . . . .	87
6.3.2	Comparison with LQR . . . . .	89
<b>7</b>	<b>Integrated System Simulation Comparisons and Results</b>	<b>93</b>
7.1	The Uncontrolled Structural Dynamics (USD) Condition . . . . .	94
7.1.1	The Zero Initial Conditions (ZIC) Configuration . . . . .	95
7.1.2	The Perturbed Initial Conditions (PIC) Configuration . . . . .	96
7.2	The Controlled Structural Dynamics (CSD) Condition . . . . .	101
<b>8</b>	<b>Conclusions</b>	<b>116</b>
8.1	Thesis Contributions . . . . .	116
8.2	Further Developments . . . . .	117
<b>A</b>	<b>Electric Propulsion Systems</b>	<b>119</b>
A.0.1	Electrothermal propulsion . . . . .	119
A.0.2	Electrostatic propulsion . . . . .	120
A.0.3	Electromagnetic propulsion . . . . .	120
<b>B</b>	<b>Linear System Properties</b>	<b>123</b>
B.1	Transfer Function Matrix . . . . .	123
B.2	State-Space Models Versus Transfer Functions . . . . .	124
B.3	Controllability and Observability . . . . .	124
B.4	Frequency Moments and Markov Parameters . . . . .	125
B.5	Output Correlation and Power Moments . . . . .	126
B.6	$\mathcal{H}_2$ and $\mathcal{H}_\infty$ Norms . . . . .	126
	<b>Bibliography</b>	<b>131</b>

# List of Figures

1.1	An example a single Solar Tower (STW) unit [Man99]. . . . .	4
1.2	The Tethered Solar Power (TSP) concept [Sas06]. . . . .	5
1.3	The Abacus Reflector (ARF) concept [WR01]. . . . .	6
2.1	Vernal and autumn equinoxes, and Earth's precession and nutation.	12
2.2	The Earth Centered Inertial (ECI) reference frame, and the Cartesian and spherical inertial coordinates. . . . .	15
2.3	Earth Centered Earth Fixed (ECEF) reference frame and Gaussian reference frame. . . . .	16
2.4	Geostationary Clohessy-Wiltshire (GCW) reference frame. . . . .	17
2.5	Classical Orbital Elements (COEs). . . . .	19
2.6	True and eccentric anomalies for elliptic motion. . . . .	20
2.7	Eccentricity and inclination equinoctial components and true longitude. . . . .	21
2.8	Perturbing acceleration due to Earth's non-homogeneous gravitational field, computed during a period of one day. . . . .	24
2.9	Earth, Sun, Moon and spacecraft relative positions. . . . .	26
2.10	Perturbing acceleration due to gravity attraction of the Sun and the Moon, computed during a period of one day. . . . .	27
2.11	Solar radiation pressure force acting on an ideal flat surface. . . . .	27
2.12	Perturbing acceleration due to solar radiation pressure, computed during a period of one day. . . . .	28
2.13	Satellite motion relative to ECI and GCW reference frames. . . . .	31
2.14	Deadband rectangular box in $(\lambda, \varphi)$ plane. . . . .	33
2.15	Tolerance ranges along $Y_G$ and $Z_G$ axes of the geostationary GCW reference frame. . . . .	34
2.16	Actuators pattern employed for the orbital control system. . . . .	35
2.17	Time history of the requested control forces expressed in the GCW reference frame. . . . .	36

LIST OF FIGURES

---

2.18	Time history of spacecraft longitude and latitude obtained integrating the linearised orbital equations over a period of twenty orbits. . . . .	38
2.19	Time history of the control forces exerted by actuators. . . . .	39
3.1	Environmental torques. . . . .	46
3.2	Full attitude state in the uncontrolled dynamics. . . . .	48
3.3	The cyclic-disturbance accommodating control for the $Z_E$ axis [WR01]	49
3.4	$\alpha$ in the ZIC. . . . .	51
3.5	Control torque in the AZIC . . . . .	51
3.6	$\alpha$ in the APIC. . . . .	52
3.7	Control torque in the APIC. . . . .	52
3.8	Actuator #1 in the APIC. . . . .	53
4.1	The ARF satellite modelled as a frame structure. . . . .	55
4.2	Frame element in local and global coordinates . . . . .	58
4.3	Comparison of the first modal mode . . . . .	62
4.4	Comparison of the second modal mode . . . . .	62
4.5	Comparison of the third modal mode . . . . .	63
4.6	Comparison of the fourth modal mode . . . . .	63
4.7	Comparison of the fifth modal mode . . . . .	63
4.8	Comparison of the sixth modal mode . . . . .	64
4.9	Comparison of the seventh modal mode . . . . .	64
4.10	Comparison of the eighth modal mode . . . . .	64
5.1	Actuators pattern employed in generating the minimal structural model of order 56. . . . .	75
5.2	Hankel Singular Values for the considered full dynamical system of the 56 <sup>th</sup> order. . . . .	76
5.3	Bode plots of the full order model, 56 <sup>th</sup> order. From input 4 to output 4. . . . .	77
5.4	Bode plots of the reduced order models. Modal truncation, 8 <sup>th</sup> and 12 <sup>th</sup> order. From input 4 to output 4. . . . .	77
5.5	Bode plots of the reduced order models. Singular perturbation approximation, 8 <sup>th</sup> and 12 <sup>th</sup> order. From input 4 to output 4. . . . .	78
5.6	Bode plots of the reduced order models. Matching moments, 8 <sup>th</sup> and 12 <sup>th</sup> order. From input 4 to output 4. . . . .	78
5.7	Bode plots of the reduced order models. Balanced reduction, 8 <sup>th</sup> and 12 <sup>th</sup> order. From input 4 to output 4. . . . .	78
5.8	Bode plots of the final considered reduced order model. Modal truncation, 14 <sup>th</sup> order. From input 4 to output 4. . . . .	79

6.1	Actuators pattern used for the vibration suppression system. . . .	86
6.2	Open-loop eigenvalues of the reduced order system in the complex plane. . . . .	87
6.3	Uncontrolled structural vibrations with respect to the imposition of initial conditions. Mode 3. . . . .	88
6.4	Closed-loop eigenvalues of the reduced order system in the complex plane. . . . .	89
6.5	Controlled structural vibrations with respect to the imposition of initial conditions. Unstructured suboptimal regulator. Mode 3. . .	89
6.6	Controlled structural vibrations with respect to the imposition of initial conditions. LQR. Mode 3. . . . .	90
6.7	Comparison between the control force provided by actuator #1. . .	92
7.1	Actuators pattern employed for the orbital and attitude control system. . . . .	95
7.2	Actuators pattern employed for the vibration suppression system. .	96
7.3	Time history of spacecraft longitude and latitude in the USD condition and the ZIC configuration. . . . .	97
7.4	Force on the actuator #1 requested for the orbit control in the USD condition and the ZIC configuration. . . . .	97
7.5	Attitude angles $\alpha$ in the USD condition and the ZIC configuration.	98
7.6	Force on the actuator #6 requested for the attitude control in the USD condition and the ZIC configuration. . . . .	98
7.7	The second modal coordinate in the USD condition and the ZIC configuration. . . . .	99
7.8	The first modal coordinate in the USD condition and the ZIC configuration. . . . .	99
7.9	The sixth modal coordinate in the USD condition and the ZIC configuration. . . . .	100
7.10	The seventh modal coordinate in the USD condition and the ZIC configuration. . . . .	100
7.11	Time history of spacecraft longitude and latitude in the USD condition and the PIC configuration. . . . .	101
7.12	Force on the actuator #1 requested for the orbit control in the USD condition and the PIC configuration. . . . .	102
7.13	Attitude angles $\alpha$ in the USD condition and the PIC configuration.	102
7.14	Force on the actuator #6 requested for the attitude control in the USD condition and the PIC configuration. . . . .	103
7.15	The fifth modal coordinate in the USD condition and the PIC configuration. . . . .	103

---

## LIST OF FIGURES

---

7.16	The sixth modal coordinate in the USD condition and the PIC configuration. . . . .	104
7.17	The seventh modal coordinate in the USD condition and the PIC configuration. . . . .	104
7.18	Time history of spacecraft longitude and latitude in the CSD condition. . . . .	106
7.19	Force on the actuator #1 requested for the orbit control in the CSD condition. . . . .	106
7.20	Attitude angles $\alpha$ in the CSD condition.. . . .	107
7.21	Force on the actuator #6 requested for the attitude control in the CSD condition. . . . .	107
7.22	The sixth modal coordinate in the CSD condition. . . . .	108
7.23	The first modal coordinate in the CSD condition, for the initial time interval. . . . .	108
7.24	The second modal coordinate in the CSD condition, for the initial time interval. . . . .	109
7.25	The third modal coordinate in the CSD condition, for the initial time interval. . . . .	109
7.26	The fourth modal coordinate in the CSD condition, for the initial time interval. . . . .	110
7.27	The fifth modal coordinate in the CSD condition, for the initial time interval. . . . .	110
7.28	The sixth modal coordinate in the CSD condition, for the initial time interval. . . . .	111
7.29	The seventh modal coordinate in the CSD condition, for the initial time interval. . . . .	111
7.30	Force on the #1S actuator in the CSD condition, for the initial time interval. . . . .	112
7.31	Force on the #2S actuator in the CSD condition, for the initial time interval. . . . .	112
7.32	Force on the #3S actuator in the CSD condition, for the initial time interval. . . . .	113
7.33	Force on the #4S actuator in the CSD condition, for the initial time interval. . . . .	113
7.34	Force on the #5S actuator in the CSD condition, for the initial time interval. . . . .	114
7.35	Force on the #6S actuator in the CSD condition, for the initial time interval. . . . .	114
A.1	Schematic diagram of an electrostatic ion thruster. . . . .	122

# Chapter 1

## Introduction

The Space Solar Power (SSP) satellite was first suggested by P. E. Glaser in 1968 [Gla68]. It was initially proposed as a large satellite orbiting around the Earth providing continuous power to the planet by collecting the solar energy. The concept is not exclusively related to a terrestrial usage, but it can be extended to a variety of potential applications. These include several missions involving outer planet robotic science, commercial applications, and human exploration. The SSP satellite is generally made of a large solar-energy collecting device. Although the most common solution is to employ one single big solar arrays panel, some concepts involve a combination of concentrating mirrors and solar arrays panels in order to minimize the mass and to optimize the power collection.

Secondly, a power transmission system is necessary to transfer the energy from the SSP satellite to the desired receiving station. With respect to the present technology, a microwave transmitting system is more reliable compared to the alternative laser system. However, a potential benefits of the laser system include smaller land area requirements for the receiving station, the elimination of radio frequency interference, and reduction of biological and ecological impacts [dep79]. In the end a receiving station is required in order to convert the microwave beam into electricity. A rectifying-antenna, (rectenna) is the common primary power receiver and link to terrestrial power distribution.

### 1.1 Reasons For The SSP Research

The concept of the SSP satellite was initially developed as an alternative to the nuclear and fossil-fuel sources for Earth consumption. Although there has been little progress, the finiteness of the fossil fuel energy and the storage of toxic product coming from the nuclear reaction are still big issues.

Secondly a SSP satellite may help overcome some of the drawbacks of generating solar power on Earth such as the absorption of solar energy by the atmosphere,

the limited utilization at night, the low solar angles and obscuration by clouds. Nowadays, the SSP satellite is far to be a feasible solution for the terrestrial power supply in terms of price per unit energy, if compared to other sources. A competitive result, in terms of cost effectiveness, may be achieved if the launch cost will drop from the present 10000-25000 \$/kg to about 500 \$/kg. At the same time, the production cost of a typical space hardware should be reduced from the present 25000-50000 \$/kg to about 1000 \$/kg [Seb04].

Beyond the economic feasibility, some technical and environmental aspects should be considered. The assembly and the maintenance of such a big structure for a period of time of about 30 years represents a very big issue. Secondly, some of the major uncertainties are the impact on the radio frequency spectrum of other terrestrial users and the atmospheric impacts such as ionospheric disruptions caused by microwave heating.

Despite the economic, technical and environmental issues related to the SSP satellites for terrestrial power supply, the studies on such an alternative energy source is an interesting challenge and stimulus for future development and for several commercial and science applications.

## 1.2 Design Concepts

Some critical aspects should be examined in order to identify the most competitive design. First of all the orbit should insure that the satellite receiving area would be most of the time exposed to the Sun, the photovoltaic devices should convert the solar energy with high efficiency, the transmitters should be able to beam an Earth-receiving station in a spectral region where minimum atmospheric absorption and scattering would be encountered. In the end modularity and simplicity may be exploited in order to reduce the initial cost and the risks related to such a project. In the end, for the purpose of developing a preliminary control system the most generic geometry and simple architecture is preferable. Three concepts have been compared: the Solar Tower (STW), the Tethered Solar Power (TSP) and the Abacus Reflector (ARF) satellites. Each one has been chosen as representative of a family of SSP satellites.

### 1.2.1 The Sun Tower Satellite

The STW concept was first introduced in 1997 [Man97]. It is a constellation of medium-scale, gravity gradient-stabilized space solar power systems. Each satellite resembles a large, Earth-pointing sunflower in which the face of the flower is the transmitter array, and the leaves on the stalk are the light-weight, inflatable and deployable solar collectors. They are placed along the power-transmitting

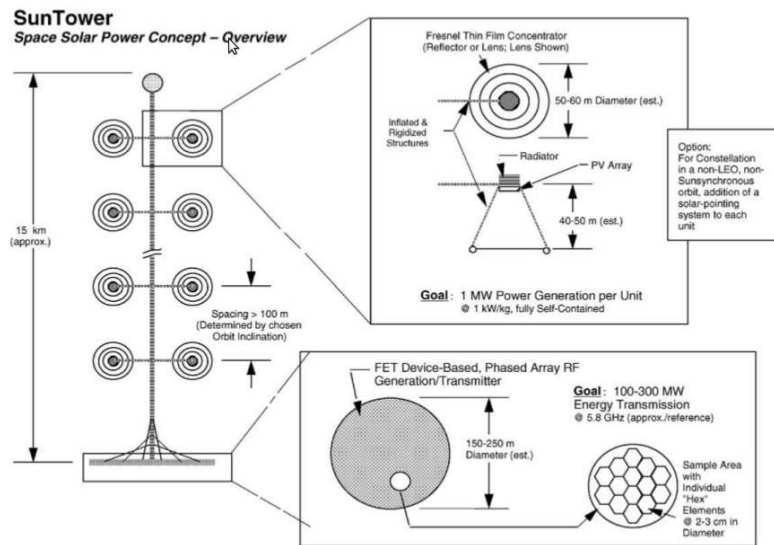


Figure 1.1: An example a single STW unit [Man99].

backbone which conveys the power generated to the transmitter. A single satellite would be about 15 km long and would be sized to approximately 100-400 MW scale. Figure 1.1 depicts a possible architecture for a single STW unit.

The STW satellite concept exploit several innovative approaches to reduce the development and life cycle cost of the SSP, while at the same time broadening market flexibility. It involves the use of highly-modularized power generation and power transmission, thus supporting the goal of low cost manufacturing.

Concerning the orbit, it may be deployed into any one of several specific orbits: sun-synchronous Low Earth Orbit (LEO), Medium Earth Orbit (MEO) and Geo-stationary Earth Orbit (GEO). The lowest cost choice is that of a constellation in a sun-synchronous LEO, inclined at an angle of about  $95^\circ$  and at an altitude of about 1500 km. In order to achieve the maximum coverage,  $\pm 30^\circ$  electronic beam steering capability was planned, and a formation of 18 SSP was assumed [Man99].

The satellite-internal power distribution is one of the biggest issue in terms of the mass of wire required to link the power generation system to the microwave transmitter and in terms of power loss.

### 1.2.2 The Tethered Solar Power Satellite

The TSP satellite was introduced in 2006 [Sas06]. It is a tethered solar power satellite consisting of two main units: a large panel ( $2 \times 1.9 \times 0.1$  km) and a bus system, connected each other by multi-wires approximately 10 km long (Figure 1.2). It resumes the idea of the sandwich power generation/transmission panel

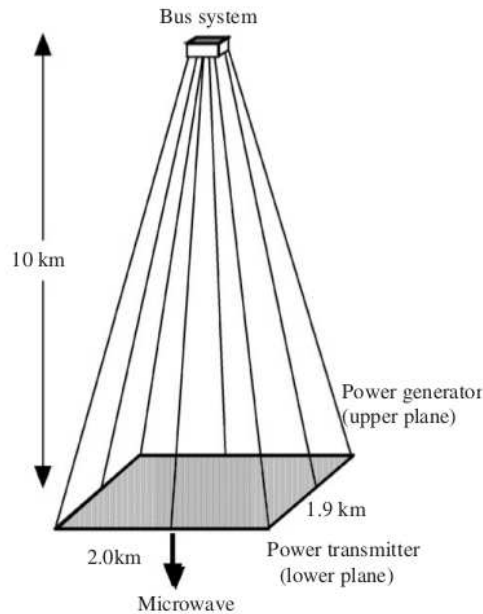


**Figure 1.2:** The TSP concept [Sas06].

introduced in 1979, where each solar array unit is packed with a microwave transmitting antenna to form a unique thin panel [dep79]. As a consequence there is no moving structure, which makes the system highly robust and stable.

The TSP satellite involves the use of highly modularized and easy integrated units. Indeed the main generation/transmission panel is composed of equivalent smaller functional units ( $100 \times 95$  m) assembled and placed in GEO. The satellite is pointing towards the Earth in order to be always visible from the same ground station, and it is kept stabilized by the gravity gradient torque without any significant active attitude control.

Although the satellite is capable of 1.2 GW of maximum power supply and 0.75 GW average on the ground, the total power efficiency is about 36% lower than the other sun-pointing SSP satellite, since the system has no mechanism to track the sun for the power generation [Sas06].

### 1.2.3 The Abacus Reflector

The ARF satellite was introduced in the late 90's. It is a square two-dimensional solar array structure ( $2 \times 1.9 \times 0.1$  km) with a total dry mass of about  $25 \times 10^6$  kg [WR01]. The solar array surface should be kept as much as possible facing the solar rays. The transmitter is located at one of its side and it's made of a stationary microwave antenna with a diameter of 500 m, and a large rotating re-

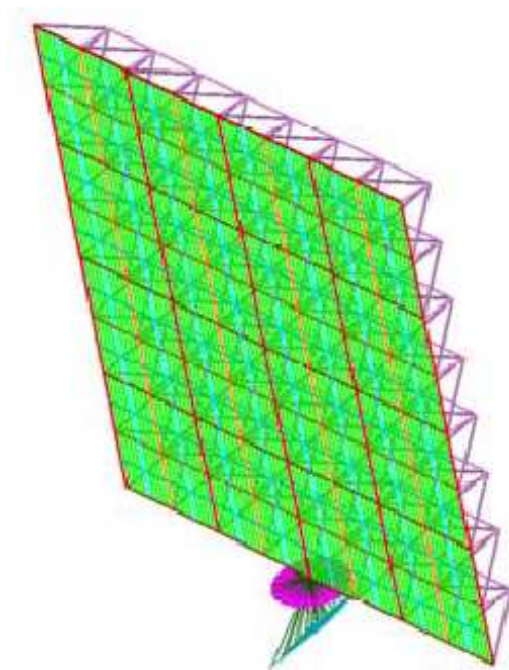


**Figure 1.3:** The ARF concept [WR01].

flector ( $500 \times 700$  m) to redirect the microwave energy to the Earth (Figure 1.3). Compared to the original concept of 1979, the ARF avoids the single infeasible rotating joint that was expected to move the antenna ([dep79], [FC03]).

The satellite is placed in GEO in order to deliver a continuous level of power of about 1.2 GW to the same receiving station on Earth. Another attractive plus is its simplicity and highly modularity that has benefits for its packaging, assembly and maintenance.

Besides these aspects, some critical points should be mentioned. The assembly and maintenance does not seem to be trivial due to the large dimensions of such a structure. Secondly, the power transmission line of GW level from the solar array panels to the transmitter requires a huge amount of conductor or super-conduction system to avoid a serious Joule loss.

Eventually, the ARF satellite is considered to be one of the most relatively low-cost SSP concept due to its modularity and simplicity. Furthermore, the highly general bi-dimensional geometry makes the vibration control design interesting for a preliminary study, since all the concepts analysed in this survey share the common feature of being characterized by one or more large surfaces. As a consequence, the ARF is chosen to be the reference SSP concept for developing a structural vibration suppression system.

## 1.3 Rationale for a Structural Vibration-Suppression System

The subject of the present thesis is a preliminary analysis of the vibrational issues regarding a large flexible structure during its operative life. In particular, the orbit and attitude control system together with the structural vibration suppression system should be capable to assure the ARF satellite of fulfilling the operativeness and functionality of the system. Beside the fact that the solar arrays should be pointed towards the Sun, the most restrictive requirements involved the transmission of the power, collected in space, to a precise point on the Earth. Especially, in the nominal condition, the SSP satellite should be kept in GEO with  $0.1^\circ$  longitude and  $0.05^\circ$  latitude accuracies, while the attitude control should guarantee  $0.08^\circ$  pointing accuracy.

These requirements have to be satisfied in the presence of large external disturbances. The orbital main disturbances are caused by the non-spherical shape of the Earth, the gravitational attraction of the Sun and the Moon and the solar radiation pressure, while the attitude disturbances are mainly induced by the gravity gradient torque and the solar radiation torque. Considering the real system behaviour, internal disturbances may be caused by uncertainties on the center of mass and the principal moment of inertia directions. Furthermore, possible rotatory-device motions, fuel sloshing or other subsystems interactions may induce unexpected perturbations.

Moreover, due to the significant mass involved in such a large spacecraft, that is about  $25 \times 10^6$  kg, the classical station keeping strategies based on impulsive manoeuvres are expected to be not exploitable. As a consequence, the continuous orbit and attitude control actions are requested to satisfy the aforementioned requirements. In this context, the use of electric thrusters with high specific impulse becomes mandatory [WR01].

This previous discussion regards only the satellite rigid motions. However, since the ARF satellite is a large flexible structure, the structural behaviour should not be neglected a priori. Significant vibrations may be induced by environmental disturbances such as the solar radiation pressures and internal disturbances due to the orbit and attitude control interactions. Moreover, the problems associated with the vibrations and their suppression should not be independently treated for the following reasons:

- The first natural frequencies of the structure are expected to be low. Therefore, the modal behaviour of the structure should be analysed.
- The orbit and attitude control may excite the low frequency modes of the structure.

### 1.3 Rationale for a Structural Vibration-Suppression System

---

- The flexibility of the structure may allow small sensors and actuators displacements and disorientation.
- The control force generated by a realistic vibration suppression system may influence the orbit and attitude configurations.

As a consequence, the purpose of the present thesis is to develop an integrated system where the orbit and attitude controls are interacting with a proper vibration suppression system. For the purpose of this preliminary study the following hypothesis are stated:

- The orbital disturbances are caused by the major environmental disturbances previously described, together with the disturbances coming from the attitude and the vibration suppression control actions.
- The attitude is affected by the gravity gradient torque and the solar radiation torque together with the disturbances coming from the orbit and the vibration suppression control actions.
- The structural vibrations are only influenced by the orbit and the attitude control actions.
- The gravity field is not considered to be of significant influence on the structural vibrations due to its very slow fluctuation.
- The thermal distortions and structural vibrations due to solar heating are not considered, because, due to its inherent modelling difficulty, is an excessive refinement for the purpose of this preliminary study. Nevertheless, since its potential criticality further study on this topic should be carried out.
- The actuators are not supposed to change the directions with respect to the undeformed structure.

In the present work, after the orbit and attitude controls have been designed, the simulations with a proper vibration suppression system are compared with the ones coming from considering the uncontrolled structural vibration dynamics. It will be exhibited that two kind of structural oscillations arise: large very low frequency oscillations, that are the natural consequence of the structural flexibility due to the nominal trend of the orbit and attitude control force, and much higher frequency vibrations in correspondence to the modal frequencies of the structure. Although the first kind of oscillations present a large amplitude, they are not considered to be dangerous for the structure, while the second kind need to be damped.

The final results show that, if the structural dynamics is left uncontrolled, the

---

structural high frequency vibrations may be excited by the orbit and attitude control actions. Contrary, the vibration suppression system developed in this work is able to damped this kind of undesired oscillations.

## 1.4 Thesis Structure

The thesis is structured following the natural development of the study.

**Chapter 1:** some concepts concerning the SSP project are introduced. Among them the ARF satellite is chosen to be the reference SSP concept for developing a structural vibration suppression system. In the end, the hypothesis and the final results are briefly described.

**Chapter 2:** an orbit control system is developed for the GEO Space Solar Power (SSP) satellite model basing upon a continuous, low thrust control action. In particular a Linear Quadratic Regulator (LQR) is designed specific requirements.

**Chapter 3:** an attitude control system is developed in order to keep the satellite in the desired attitude. Two kind of regulators are designed and compared in terms of performance and control inputs: the Proportional Integrative Derivative (PID) and the Linear Quadratic (LQ) regulator.

**Chapter 4:** an Finite Element (FE) model of the Abacus-like structure is developed as a bi-dimensional frame. The geometric properties are chosen such that some important features of the reference Abacus concept, inertial characteristics and the first modal frequency, are met [WR01]. The modal analysis results are compared with those obtained from an analogous model developed with another software for FE analysis.

**Chapter 5:** several reduction techniques of the high-order dynamical systems coming from finite element analysis of the flexible structures are discussed. In the end, it is performed the order reduction of the structural model of the satellite employing the introduced methods.

**Chapter 6:** since a direct state feedback control cannot be employed for such a large system, a direct output feedback controller, with the objective of suppressing the structural vibrations, is designed. In the end, the results, obtained employing the developed suboptimal control law, are presented.

**Chapter 7:** in this chapter the simulations with a proper vibration suppression system are compared with the ones coming from considering the uncontrolled structural vibration dynamics.

**Chapter 8:** the contributions coming from the present work are summarized and critically discussed. In the end, possible areas of future works are suggested.

# Chapter 2

## Orbital Dynamics and Control

It is underlined in Chapter 1 that the objective of the present thesis is to study the issues related to the vibrations which could be triggered during the operative life of a SSP satellite, especially considering the effects of the forces introduced into the structure by the orbital/attitude control systems. Hence first of all, an orbit control system is developed for the GEO SSP satellite model basing upon a continuous, low thrust control action. A quick background on time measure systems is firstly given. Then the different reference frames employed for the perturbed orbital dynamics analysis are introduced. Once presented several equivalent techniques for representing the state of a satellite (considered as punctiform) along its orbit, the main environmental orbital perturbations acting on a GEO satellite are surveyed. The fully non-linear equations holding the translational dynamics of a satellite in its motion along the perturbed orbit are compared with a linearised model based on the Clohessy-Wiltshire equations for the relative orbital motion. After discussing the requirements on the orbital position of a SSP in GEO orbit, it is presented a Linear Quadratic Regulator (LQR) approach in designing a control law able to fulfil the aforementioned requirements.

### 2.1 Time Measure

In the following sections the time conventions useful in developing the orbital dynamic model are introduced.

#### 2.1.1 Sidereal Time and Universal Time

Sidereal time is a system of timekeeping based on the rotation of the Earth with respect to the fixed stars in the sky. More specifically the Local Apparent Sidereal Time (LAST), is defined as the hour angle of the vernal equinox at that locality. The equinoxes, as can be seen in Figure 2.1a, are the two instants in which the

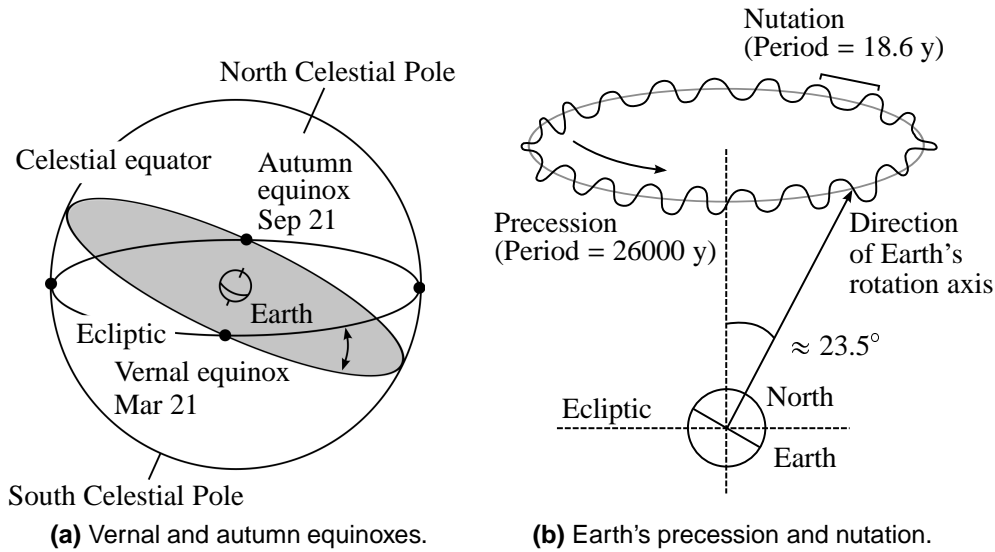


**Figure 2.1:** Vernal and autumn equinoxes, and Earth's precession and nutation.

Sun, in its apparent motion about the Earth, crosses the intersection between the the equator plane and the ecliptic plane, namely the line of nodes. Among the two, the vernal equinox is the one in which the Sun's path crosses the line of nodes moving south to north, defining the First Point of Aries (symbol  $\Upsilon$ ). Due to the effect of precession, the First Point of Aries is not a fixed point in space but it moves along the ecliptic at a rate of roughly one degree every seventy years.

Apparent Sidereal Time differs from Mean Sidereal Time by an amount due to nutation, the nodding motion of the Earth's axis of rotation superimposed on that of precession (see Figure 2.1b). When the measurements are made with respect to the prime meridian at Greenwich, the times are referred to as Greenwich Apparent Sidereal Time (GAST) and Greenwich Mean Sidereal Time (GMST). The latter will be important in the developments of the present work.

Universal Time (UT), more precisely its variations UT1, is based on a fictitious mean Sun exhibiting uniform motion in right ascension (see Section 2.2) along the equator and is related to the mean solar time at Greenwich. The Coordinated Universal Time (UTC), a time scale determined using highly precise atomic clocks, was introduced as a convenient approximation of UT1 and is the basis for the worldwide system of civil time which all satellite operations refer to.

### 2.1.2 Epoch and Calendar Date

The moment in which an event occurs is referred as to the epoch of the event. The epoch indicates a particular instant designated with a calendar date expressed following the convention

⟨ year month day hours minutes seconds ⟩

For example the date

$$\langle 2012 \ 1 \ 1 \ 12 \ 0 \ 0.0 \rangle$$

designates January 1, 2012 at 12<sup>h</sup> 00' 00.0" UTC.

Another way to designate a date (useful in defining the celestial body ephemerides) is in terms of decimal number of days since a reference epoch. When the considered reference date is January 1, 4713 BC at noon, the Julian Date (JD) is computed. In order to deal with dates of handier orders of magnitude, the epoch designated by the date January 1, 2000 at 00<sup>h</sup> 00' 00.0" UTC of beginning of a Julian year, is taken as the reference date. Its connection with the Julian Date is directly computed as

$$JD_{2000} = JD - 2451544.5 \quad (2.1)$$

A Julian year is the solar year of 365.25 days, which implies one extra day every four years.

Given this framework for the measure of time, the approximate GMST at any epoch can be calculated, with a loss of precision of 0.1 second per century, using the following formula,

$$GMST = 18.697374558 + 24.06570982441908D \quad (2.2)$$

where  $D$  are the number of days and fraction since January 1, 2000 at 12<sup>h</sup> 00' 00.0" UTC and GMST needs to be reduced in the range 0<sup>h</sup> to 24<sup>h</sup> [Kap81].

## 2.2 Reference Frames and Coordinate Systems

### 2.2.1 Earth Centered Inertial RFCS

ECI reference frame  $XYZ$  (Figure 2.2a) has its origin at the center of mass of the Earth and the fundamental plane coinciding with the Earth's equatorial plane. The  $X$  axis is aligned with the line of nodes directed towards the First Point of Aries  $\Upsilon$ , the  $Z$  axis points to the North Pole and  $Y$  completes a right-handed orthogonal coordinate system.

Earth Centered Inertial (ECI) frame is not truly inertial, due to the fact that the vernal equinox and equatorial plane vary slightly over time. The gravitational attraction of the Sun and Moon on the Earth's equatorial bulge cause the rotational axis of the Earth to precess in space. Nutation is the smaller amplitude shorter period wobble superposed on the precessional motion that is caused by the shorter period fluctuations in the strength of the torque exerted on Earth's equatorial bulge by the sun, moon, and planets.

In order to achieve a sufficiently inertial coordinate system, the equinoxes and equator are specified at a particular epoch. From 1984 the most commonly used

reference epoch is January 1, 2000 at 12<sup>h</sup> 00' 00.0" UTC.

The position of a point in the ECI frame, as can be seen in Figure 2.2b can be specified by either Cartesian coordinates  $x, y, z$  or using spherical coordinates, i.e. geocentric distance  $r$ , right ascension  $\alpha$  and declination  $\delta$ .

### 2.2.2 Earth Centered Earth Fixed RFCS

ECEF reference frame  $X_F Y_F Z_F$  is a geocentric coordinate system which is allowed to rotate with the Earth. The fundamental plane is the Earth's equatorial plane. The  $Z_F$  axis coincides with  $Z$  whilst  $X_F$  is always aligned with the Greenwich meridian.

Position in this coordinate frame is given defining the geocentric distance  $r$ , the geographical longitude  $\lambda$  and the geocentric latitude  $\varphi$  (Figure 2.3a). Longitude  $\lambda$  is counted positively towards the East, and differs from the right ascension  $\alpha$  by the right ascension  $\Theta$  of the Greenwich meridian.

$$\lambda = \alpha - \Theta. \quad (2.3)$$

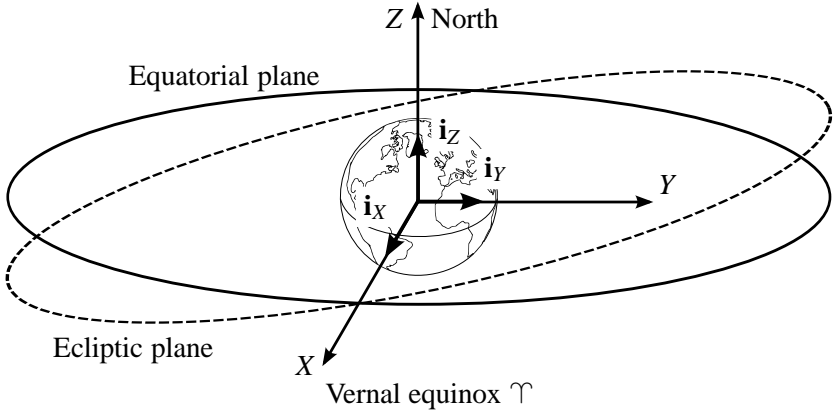
The right ascension  $\Theta$  of the Greenwich meridian at a certain time (in the UTC system) is equal to GMST and can be computed using (2.2).

### 2.2.3 Gaussian RFCS

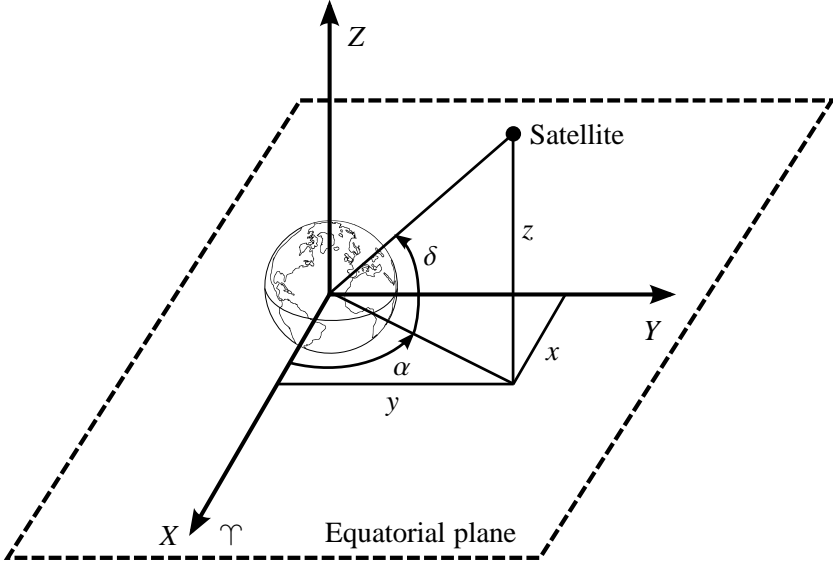
Gaussian reference frame is a reference system designed by  $RTN$  axes with the origin fixed to the position of the spacecraft considered as punctiform. The unit vectors  $\mathbf{i}_R$ ,  $\mathbf{i}_T$  and  $\mathbf{i}_N$  of its orthonormal basis have the same directions of the  $R$ ,  $T$ ,  $N$  axes (see Figure 2.3b). Axis  $R$  is defined as always pointing from the Earth's center along the radius vector toward the satellite as it moves through the orbit. The  $N$  axis is normal to the orbit plane with direction of the satellite angular momentum vector and the  $T$  axis is perpendicular to  $R$  in the orbit plane and with the direction toward the satellite movement. It completes, with the unit vectors  $\mathbf{i}_R$  and  $\mathbf{i}_N$ , a right-handed orthogonal basis.

### 2.2.4 Geostationary Clohessy-Wiltshire RFCS

GCW frame with  $X_G Y_G Z_G$  axes is a non-inertial reference frame rotating with the Earth (see Figure 2.4). The reference plane is the equatorial plane and the origin of this coordinate system is in the point of perfect geostationary orbit. The  $X_G$  axis lies along the radial direction pointing in opposite direction of the Earth, the  $Z_G$  axis is normal to the equatorial plane towards North and  $Y_G$  completes a right-handed orthogonal coordinate system.

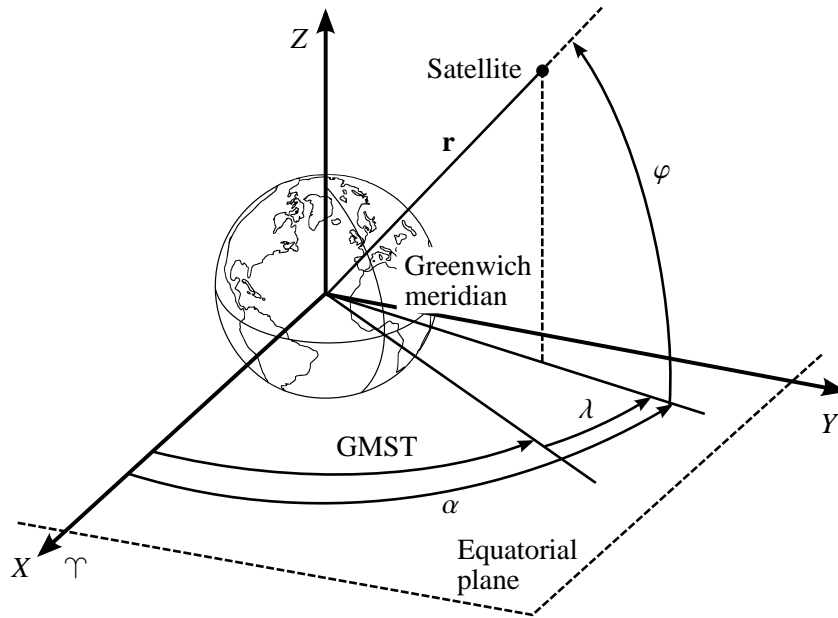


(a) ECI reference frame.

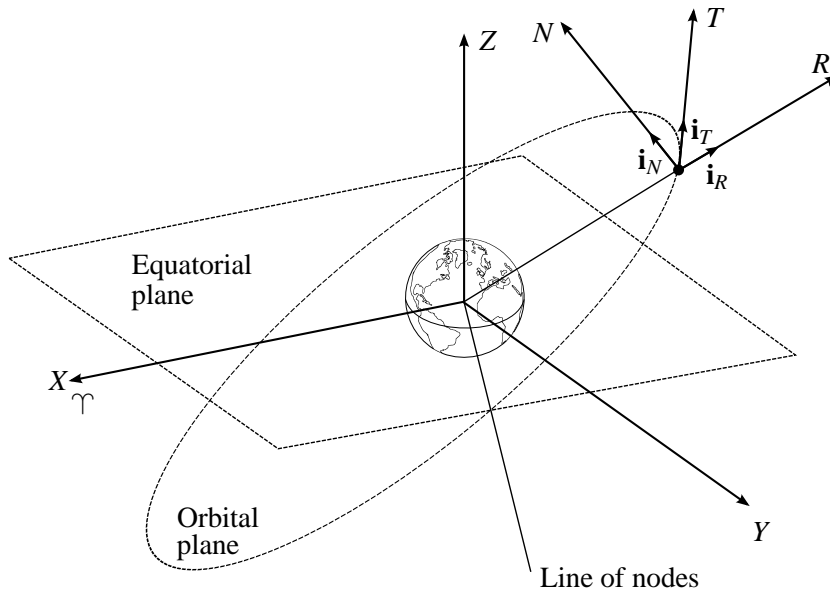


(b) Cartesian and spherical inertial coordinates within the ECI frame.

**Figure 2.2:** The ECI reference frame, and the Cartesian and spherical inertial coordinates.



(a) ECEF reference frame.



(b) Gaussian reference frame.

Figure 2.3: ECEF reference frame and Gaussian reference frame.

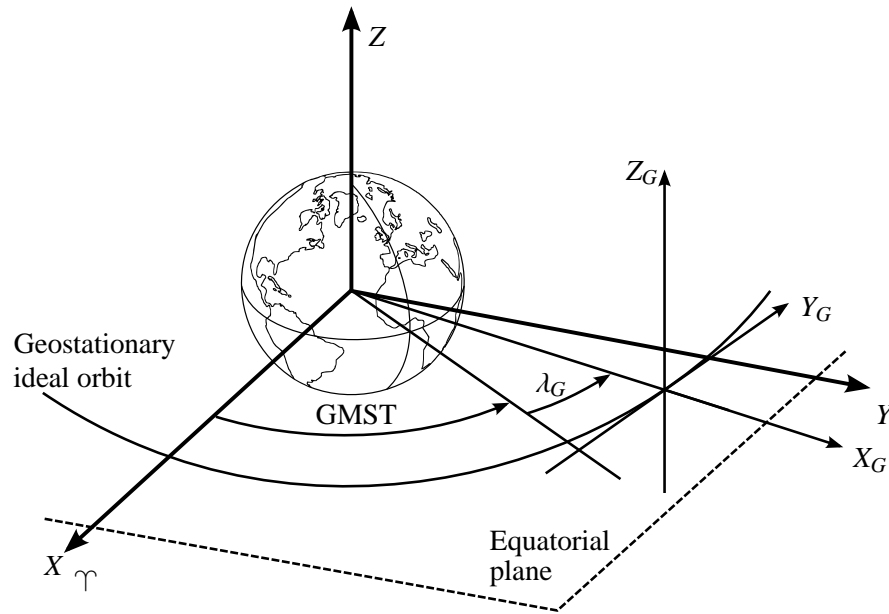


**Figure 2.4:** GCW reference frame.

The position of a point in the GCW frame is specified by Cartesian coordinates  $x_G$ ,  $y_G$  and  $z_G$ .

## 2.3 Satellite State Representation

This section describes some equivalent forms in which the state of a satellite in space can be expressed. For this state to be completely defined six quantities need to be specified. The collection of these quantities is referred to as either a state vector or a set of orbital elements referenced to a particular frame.

The following sections consider a spacecraft subjected only to the gravitational attraction of the Earth with punctiform mass (unperturbed motion).

### 2.3.1 Position and Velocity

In the ECI frame position and velocity vectors of a spacecraft can be simply denoted as follows,

$$\mathbf{r} = [x \quad y \quad z]^T \quad (2.4a)$$

$$\mathbf{v} = \dot{\mathbf{r}} = [\dot{x} \quad \dot{y} \quad \dot{z}]^T \quad (2.4b)$$

and the acceleration of the spacecraft satisfies the second-order vector differential equation governing the relative motion of two bodies in space.

$$\ddot{\mathbf{r}} = -\frac{\mu_{\oplus}}{r^3}\mathbf{r} \quad (2.5)$$

where  $\mu_{\oplus}$  is the gravitational parameter of the Earth. Therefore, the state representation by position and velocity of a spacecraft is expressed by,

$$\mathbf{x} = [x \ y \ z \ \dot{x} \ \dot{y} \ \dot{z}]^T \quad (2.6)$$

### 2.3.2 Classical Orbital Elements

The two-body system characterized by (2.5) has three degrees of freedom, and the orbit is uniquely determined if six initial conditions are specified, three of which are associated with  $r$  at some initial time, and three of which are associated with velocity  $v$ .

In orbital mechanics the constants of integration, or various functions thereof, are also referred to as elements of the orbit and such initial conditions can be considered as six possible orbital elements.

A common set of scalars often employed to describe a satellite orbit is the Classical Orbital Elements (COEs) set. It consists of five independent quantities, which are sufficient to completely describe the size, shape, and orientation (with respect to the ECI frame) of an orbit, and one quantity required to pinpoint the position of a satellite along the orbit at any particular time. The six parameters are (Figure 2.5) the following

- Semi-major axis  $a$ : it specifies the size of the orbit.
- Eccentricity  $e$ : it specifies the shape of the orbit.
- Inclination of the orbit plane  $i$ : specifies the tilt of the orbit plane with respect to the Earth's equatorial plane.
- Right ascension of the ascending node  $\Omega$ : it is the angle from the positive  $X$  axis to the line of node, that is the intersection between the equatorial plane and the orbital plane, where the orbit crosses from south to north.
- Argument of the perigee  $\omega$ : it is the angle measured from the ascending node to the perigee.
- True anomaly  $f$ : it specifies the position of the satellite within its orbit and it is the angle between the perigee and the current position vector  $r$ .

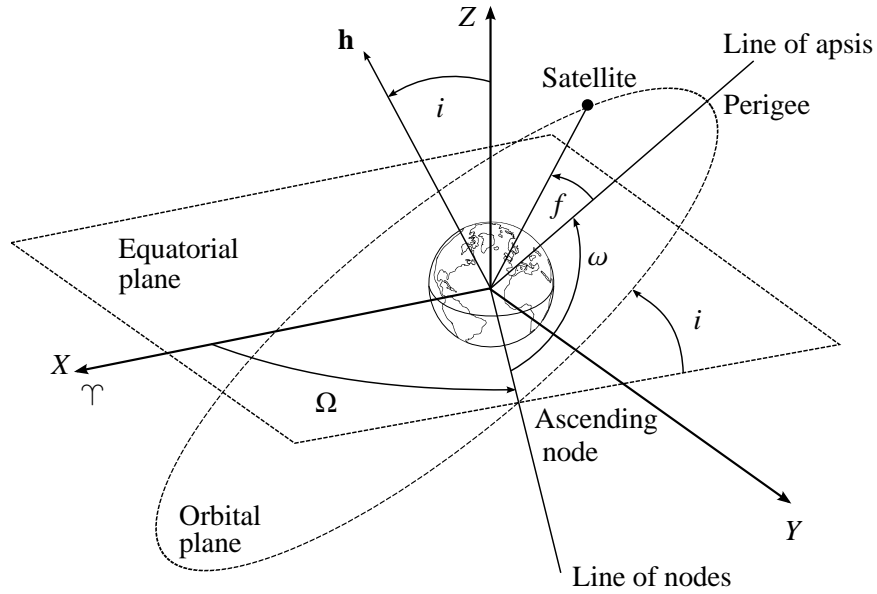


**Figure 2.5:** Classical Orbital Elements (COEs).

Other quantities can be used instead of the true anomaly to describe the satellite position on the orbit. One choice is the eccentric anomaly  $E$  which is the angle defined on the auxiliary circle of radius  $a$  as in Figure 2.6. It is related to the true anomaly by means of the following relation,

$$\tan \frac{f}{2} = \sqrt{\frac{1+e}{1-e}} \tan \frac{E}{2} \quad (2.7)$$

Eccentric anomaly can be used to express the position of a satellite as a function of time,

$$E - e \sin E = \sqrt{\frac{\mu_{\oplus}}{a^3}} (t - t_p) = n (t - t_p) \quad (2.8)$$

where  $n$  is the mean motion  $t_p$  is the time of pericenter passage. Defining the mean anomaly  $M = n (t - t_p)$ , Kepler's time equation can be written as

$$M = E - e \sin E. \quad (2.9)$$

Satellite state representation in terms of classical orbital elements is then denoted as follows,

$$\mathbf{x}_{COE} = [a \ e \ i \ \Omega \ \omega \ \text{anomaly}]^T \quad (2.10)$$

where the anomaly component can be one among  $f$ ,  $E$  and  $M$ .

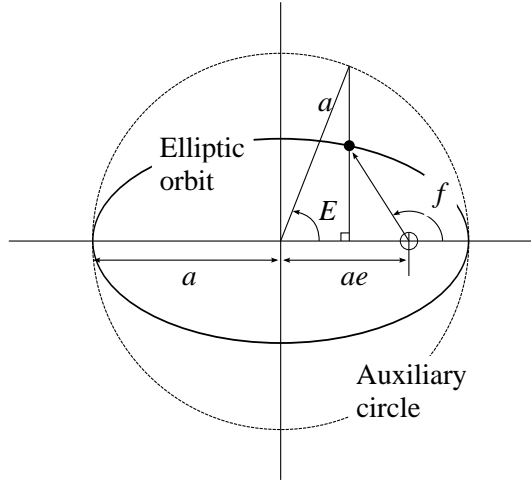


**Figure 2.6:** True and eccentric anomalies for elliptic motion.

### 2.3.3 Equinoctial Orbital Elements

COEs suffer from two main singularities. The first is when the orbit is circular, i.e., when the eccentricity is zero ( $e = 0$ ). In this case the line of apsis is undefined and also the argument of perigee  $\omega$ . The second occurs when the orbit is equatorial, i.e., when the inclination is zero ( $i = 0$ ). In this case the ascending node is undefined and also the right ascension of the ascending node  $\Omega$ . In order to deal with non-singular elements when analysing geostationary orbits, one must search for combinations of the COEs to define a new set of parameters, known as Equinoctial Orbital Elements (EOEs).

The EOEs avoid the singularities encountered when using the classical orbital elements. Their definitions in terms of Keplerian elements are given by the following equations [BC71],

$$a, \quad (2.11a)$$

$$P_1 = e \sin(\omega + \Omega), \quad (2.11b)$$

$$P_2 = e \cos(\omega + \Omega), \quad (2.11c)$$

$$Q_1 = \tan \frac{i}{2} \sin \Omega, \quad (2.11d)$$

$$Q_2 = \tan \frac{i}{2} \cos \Omega, \quad (2.11e)$$

$$L = \Omega + \omega + f. \quad (2.11f)$$

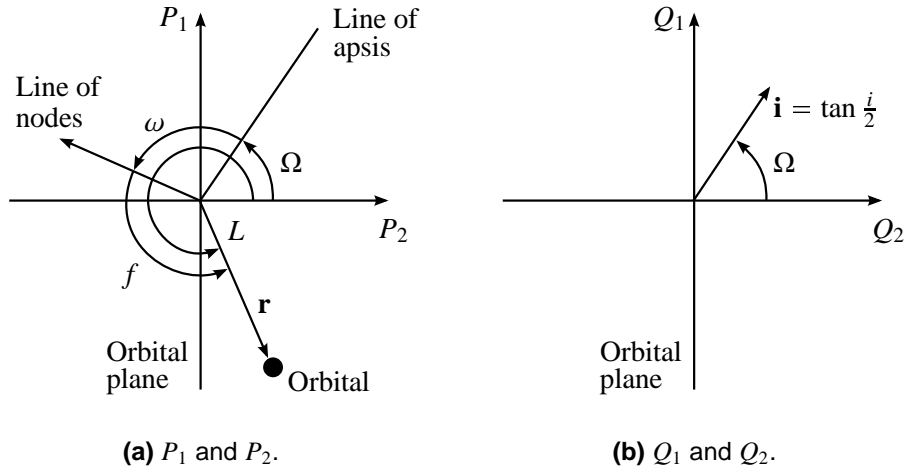


**Figure 2.7:** Eccentricity and inclination equinoctial components and true longitude.

The latter equation defines the true longitude  $L$ . Similarly to what happens with the COEs, the true longitude (function of the true anomaly) can be replaced by functions of either the eccentric or the mean anomaly, namely  $E$  and  $M$ . Employing these anomaly leads to the definition of the eccentric longitude and the mean longitude,

$$K = \Omega + \omega + E, \quad (2.12a)$$

$$l = \Omega + \omega + M. \quad (2.12b)$$

GEO satellite state representation in terms of Equinoctial Orbital Elements (EOEs) will be denoted as follows,

$$\mathbf{x}_{EOE} = [a \ P_1 \ P_2 \ Q_1 \ Q_2 \ \text{anomaly}]^T, \quad (2.13)$$

where the anomaly component can be one among  $L$ ,  $K$  and  $l$ .

In the equinoctial frame, depicted in Figure 2.7 the elements  $P_1$  and  $P_2$  represent the projection of the eccentricity vector onto the axes. The elements  $Q_1$  and  $Q_2$  represent the projection of the vector oriented in the direction of the ascending node with magnitude  $\tan(i/2)$  (see [CL]).

## 2.4 Environmental Perturbations

Thus far an ideal two body problem, held by (2.5), has been considered. This section deals with the analysis of the orbital dynamics when orbital perturbation are taken into account. For geostationary satellites, the disturbing accelerations that need to be considered are related to

- Non-spherical shape of the Earth.
- Gravitational attraction of the Sun and the Moon.
- Solar radiation pressure.

Due to perturbing accelerations, the equation that holds the non-Keplerian orbit dynamics becomes,

$$\ddot{\mathbf{r}} + \frac{\mu_{\oplus}}{r^3} \mathbf{r} = \mathbf{a}_p, \quad (2.14)$$

in which  $\mathbf{a}_p$ , the perturbing acceleration, represents the resultant perturbing force per unit mass acting on the satellite.

$$\mathbf{a}_p = \mathbf{a}_e + \mathbf{a}_g + \mathbf{a}_r, \quad (2.15)$$

where  $\mathbf{a}_e$  is caused by the asymmetric gravity attraction of the Earth,  $\mathbf{a}_g$  by the gravity attraction of the Sun and the Moon and  $\mathbf{a}_r$  is due to the solar radiation pressure.

### 2.4.1 Earth's Gravitational Field

The gravitational field of a continuous and non-homogeneous distribution of mass can be conveniently described by its potential function  $V_e$ .

$$V_e(r, \lambda, \varphi) = \frac{\mu_{\oplus}}{r} + \tilde{V}_e(r, \lambda, \varphi). \quad (2.16)$$

in which  $\tilde{V}_e$  is the perturbing gravitational potential expressed by,

$$\tilde{V}_e(r, \lambda, \varphi) = \frac{\mu_{\oplus}}{r} \sum_{n=2}^{\infty} \sum_{m=0}^n \left( \frac{R_{\oplus}}{r} \right)^n P_{nm}(\sin \varphi) [C_{nm} \cos(m\lambda) + S_{nm} \sin(m\lambda)]. \quad (2.17)$$

In the previous expression  $C_{nm}$  and  $S_{nm}$  are the tesseral ( $n \neq m$ ), sectoral ( $n = m$ ) and zonal ( $m = 0$ ) harmonic coefficients characterizing the Earth's mass distribution, and  $P_{nm}$  is the associated Legendre function of degree  $n$  and order  $m$ . In the present work only the primary zonal ( $C_{20}$  and  $S_{20}$ ) and sectoral ( $C_{22}$  and  $S_{22}$ ) effects are taken into account whilst the higher degree and order harmonics are neglected. In particular, the Earth's elliptical equator, described by the primary sectoral harmonics, gives rise to a gravitational acceleration that causes a drift in the longitudinal position of geostationary satellites, which is a major perturbation that must be dealt with. There are four equilibrium points separated by approximately  $90^\circ$  along the equator, two stable points and two unstable points. The effect of the triaxiality is to cause geosynchronous satellites to oscillate about the nearest stable point on the minor axis. These two stable points, at about  $75^\circ$  E longitude

**Table 2.1:** Geopotential coefficients and the corresponding Legendre functions.

$n$	$m$	$C_{nm}$	$S_{nm}$	$P_{nm}(\sin \varphi)$
2	0	$-1.08 \times 10^{-3}$	0	$\frac{3}{2} \sin^2 \varphi - \frac{1}{2}$
2	2	$-1.57 \times 10^{-6}$	$-9.03 \times 10^{-7}$	$3 \cos^2 \varphi$

and  $105^\circ$  W longitude, are called gravitational valleys.

Table 2.1 shows the values of the coefficients and the related Legendre function for the considered harmonics [M<sup>+</sup>88]. The components of the acceleration vector

$$\mathbf{a}_e = a_{eX} \mathbf{i}_X + a_{eY} \mathbf{i}_Y + a_{eZ} \mathbf{i}_Z, \quad (2.18)$$

induced by the perturbing potential function  $\tilde{V}_e$  and expressed in the ECI reference frame are obtained calculating the partial derivative of  $\tilde{V}_e$  with respect to the inertial coordinates.

$$\mathbf{a}_e = \nabla \tilde{V}_e. \quad (2.19)$$

The acceleration components are decomposed as follows,

$$a_{eX} = \mu_{\oplus} R_{\oplus}^2 (a_{eX}^{20} + a_{eX}^{22}), \quad (2.20a)$$

$$a_{eY} = \mu_{\oplus} R_{\oplus}^2 (a_{eY}^{20} + a_{eY}^{22}), \quad (2.20b)$$

$$a_{eZ} = \mu_{\oplus} R_{\oplus}^2 (a_{eZ}^{20} + a_{eZ}^{22}). \quad (2.20c)$$

where the expressions of the normalized acceleration components, in function of the ECI coordinates  $x, y, z$ , are given in [Los07] as,

$$a_{eX}^{20} = \frac{3C_{20}}{2} \frac{x(x^2 + y^2 - 4z^2)}{(x^2 + y^2 + z^2)^{7/2}}, \quad (2.21a)$$

$$a_{eY}^{20} = \frac{3C_{20}}{2} \frac{y(x^2 + y^2 - 4z^2)}{(x^2 + y^2 + z^2)^{7/2}}, \quad (2.21b)$$

$$a_{eZ}^{20} = \frac{3C_{20}}{2} \frac{z(3x^2 + 3y^2 - 2z^2)}{(x^2 + y^2 + z^2)^{7/2}}. \quad (2.21c)$$

As regards the disturbing acceleration caused by the effect of the triaxiality of the Earth,

$$a_{eX}^{22} = \frac{6(y^3 + yz^2 - 4x^2y) F_{22}^+(\Theta) + 3(2xz^2 - 3x^3 + 7xy^2) F_{22}^-(\Theta)}{(x^2 + y^2 + z^2)^{7/2}}, \quad (2.22a)$$

$$a_{eY}^{22} = \frac{6(x^3 + xz^2 - 4y^2x) F_{22}^+(\Theta) - 3(2yz^2 - 3y^3 + 7yx^2) F_{22}^-(\Theta)}{(x^2 + y^2 + z^2)^{7/2}}, \quad (2.22b)$$

$$a_{eZ}^{22} = \frac{-30xyz F_{22}^+(\Theta) + 15z(y^2 - x^2) F_{22}^-(\Theta)}{(x^2 + y^2 + z^2)^{7/2}}. \quad (2.22c)$$

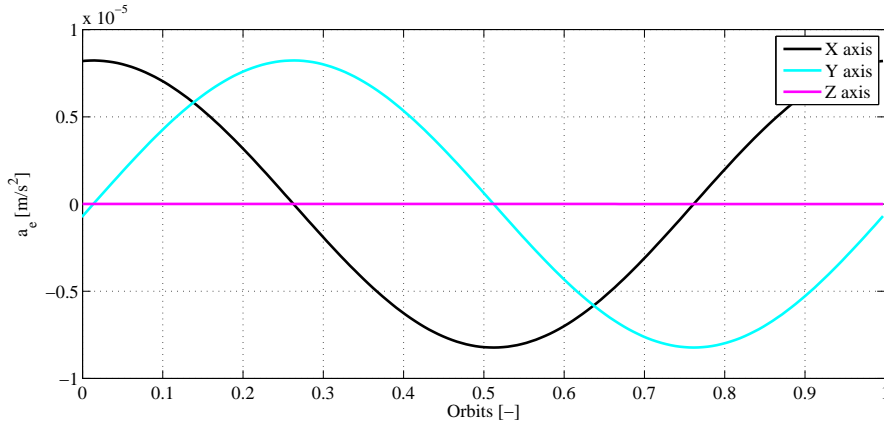


**Figure 2.8:** Perturbing acceleration due to Earth's non-homogeneous gravitational field, computed during a period of one day.

where

$$F_{22}^+(\Theta) = C_{22} \sin(2\Theta) + S_{22} \cos(2\Theta), \quad (2.23a)$$

$$F_{22}^-(\Theta) = C_{22} \cos(2\Theta) - S_{22} \sin(2\Theta). \quad (2.23b)$$

## 2.4.2 Gravity Attraction of the Sun and the Moon

In order to obtain a sufficiently accurate model of the dynamics of a geostationary satellite, the attractions exerted by the Sun and the Moon must be considered as third-body perturbing accelerations acting on the spacecraft.

The perturbing acceleration  $\mathbf{a}_g$  caused by the luni-solar gravitational effects on the satellite is described by,

$$\mathbf{a}_g = -\mu_{\odot} \left( \frac{\mathbf{r}_S}{r_S^3} + \frac{\mathbf{r}_{\odot}}{r_{\odot}^3} \right) - \mu_{\zeta} \left( \frac{\mathbf{r}_M}{r_M^3} + \frac{\mathbf{r}_{\zeta}}{r_{\zeta}^3} \right), \quad (2.24)$$

where  $\mathbf{r}_S$  and  $\mathbf{r}_M$  are the position vectors of the satellite from the Sun and the Moon, and  $\mathbf{r}_{\odot}$  and  $\mathbf{r}_{\zeta}$  are the position vectors of the Sun and the Moon, all of them measured in the ECI reference frame.

As it appears clearly, for the computation of the solar and lunar gravity attraction it is necessary to express the positions of the Sun and the Moon in the ECI reference frame as functions of time. This can be done by means of their ephemerides which tabulate the position of the Sun and the Moon, in terms of right ascension and declination, as functions of time.

After some manipulations, the components of the disturbing acceleration, given

by (2.24), can be easily expressed in function of the inertial coordinates as follows [WR01],

$$a_{gx} = \frac{\mu_{\odot}}{r_{\odot}^3} \left( -x + \frac{3r}{r_{\odot}} \left[ \cos \theta_{\odot} + \frac{r}{2r_{\odot}} (5 \cos^2 \theta_{\odot} - 1) \right] (r_{\odot x} - x) \right) + \frac{\mu_{\zeta}}{r_{\zeta}^3} \left( -x + \frac{3r}{r_{\zeta}} \left[ \cos \theta_{\zeta} + \frac{r}{2r_{\zeta}} (5 \cos^2 \theta_{\zeta} - 1) \right] (r_{\zeta x} - x) \right), \quad (2.25a)$$

$$a_{gy} = \frac{\mu_{\odot}}{r_{\odot}^3} \left( -y + \frac{3r}{r_{\odot}} \left[ \cos \theta_{\odot} + \frac{r}{2r_{\odot}} (5 \cos^2 \theta_{\odot} - 1) \right] (r_{\odot y} - y) \right) + \frac{\mu_{\zeta}}{r_{\zeta}^3} \left( -y + \frac{3r}{r_{\zeta}} \left[ \cos \theta_{\zeta} + \frac{r}{2r_{\zeta}} (5 \cos^2 \theta_{\zeta} - 1) \right] (r_{\zeta y} - y) \right), \quad (2.25b)$$

$$a_{gz} = \frac{\mu_{\odot}}{r_{\odot}^3} \left( -z + \frac{3r}{r_{\odot}} \left[ \cos \theta_{\odot} + \frac{r}{2r_{\odot}} (5 \cos^2 \theta_{\odot} - 1) \right] (r_{\odot z} - z) \right) + \frac{\mu_{\zeta}}{r_{\zeta}^3} \left( -z + \frac{3r}{r_{\zeta}} \left[ \cos \theta_{\zeta} + \frac{r}{2r_{\zeta}} (5 \cos^2 \theta_{\zeta} - 1) \right] (r_{\zeta z} - z) \right), \quad (2.25c)$$

where  $\theta_{\odot}$  is the angle between the Earth-satellite line and the Earth-Sun line and  $\theta_{\zeta}$  is the angle between the Earth-satellite line and the Earth-Moon line, as depicted in Figure 2.9.

### 2.4.3 Solar Radiation Pressure

A satellite exposed to solar radiation experiences a small force that arises due to photons impinging on its surface, as illustrated in Figure 2.11. It is assumed that a fraction,  $\epsilon_r$ , of the impinging photons is specularly reflected, a fraction,  $\epsilon_d$ , is diffusely reflected, and a fraction,  $\epsilon_a$ , is absorbed by the surface,

$$\epsilon_r + \epsilon_d + \epsilon_a = 1. \quad (2.26)$$

The solar radiation pressure acceleration acting on a flat surface is then expressed as,

$$\mathbf{a}_r = P_{\odot} \frac{A_s}{m_s} (\mathbf{n}_s \cdot \mathbf{r}_S) \left[ (1 - \epsilon_r) \mathbf{r}_S + \left( 2\epsilon_r (\mathbf{n}_s \cdot \mathbf{r}_S) + \frac{2}{3} \epsilon_d \right) \mathbf{n}_s \right]. \quad (2.27)$$

where coefficient  $P_{\odot} \approx 4.56 \times 10^{-6} \text{ N/m}^2$  is the nominal solar radiation pressure constant,  $A_s$  and  $m_s$  are the satellite surface and mass,  $\mathbf{n}_s$  is a unit vector normal to the surface and  $\mathbf{r}_S$  is, as previously stated, the position vector of the satellite with

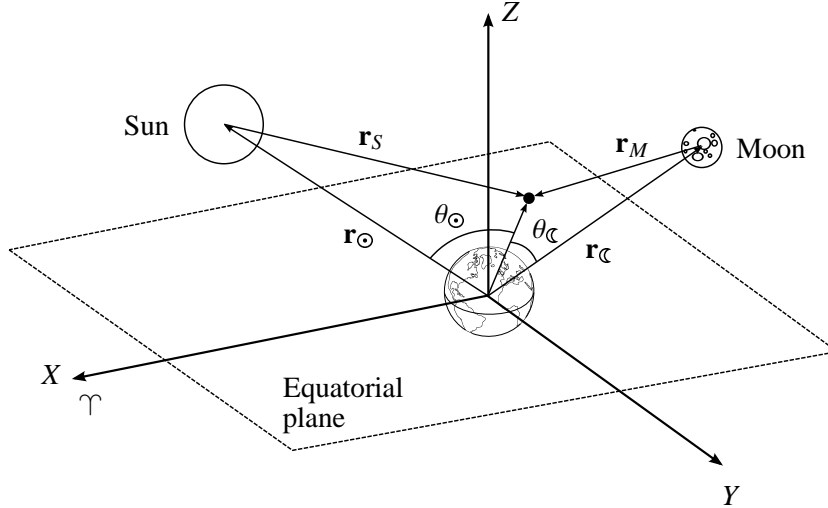


**Figure 2.9:** Earth, Sun, Moon and spacecraft relative positions.

respect to the Sun.

In contrast to the gravitational perturbations so far discussed, the acceleration due to the solar radiation depends on the spacecraft mass and surface area. Moreover its computation involves the determination of the precise location of the Sun, the correct satellite orbital attitude, the exact value of the solar radiation pressure coefficient, the effective time-varying cross-sectional area exposed to the incoming radiation, the correct and usually time-varying coefficients that model the spacecraft reflectivity.

For an ideal case of a perfect mirror with  $\epsilon_d = \epsilon_a = 0$  and  $\epsilon_r = 1$ , the resulting acceleration is directed normally to the surface,

$$\mathbf{a}_r = 2P_{\odot} \frac{A_s}{m_s} \cos^2 \phi \mathbf{n}_s. \quad (2.28)$$

Also for an ideal case of a black body with  $\epsilon_r = \epsilon_d = 0$  and  $\epsilon_a = 1$ , the effect of solar radiation is,

$$\mathbf{a}_r = P_{\odot} \frac{A_s}{m_s} \cos^2 \phi \frac{\mathbf{r}_S}{r_S}. \quad (2.29)$$

where  $A_s \cos \phi$  is usually referred as to the projected area of the surface under consideration.

For most practical cases a simplified expression of the solar radiation acceleration,

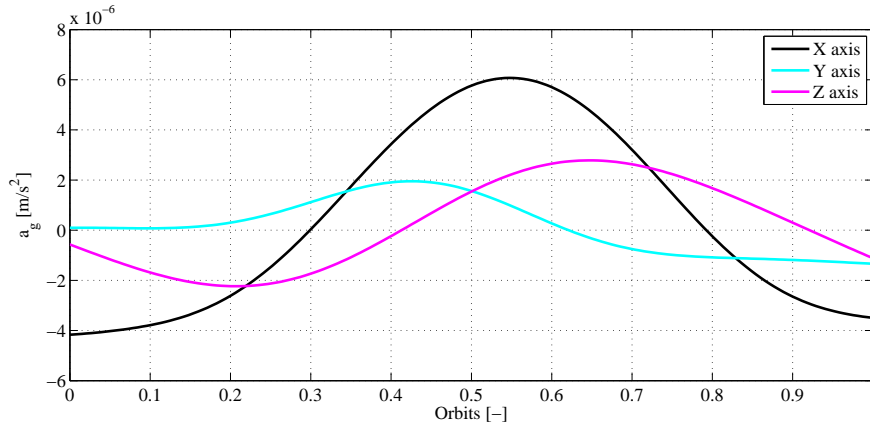


**Figure 2.10:** Perturbing acceleration due to gravity attraction of the Sun and the Moon, computed during a period of one day.

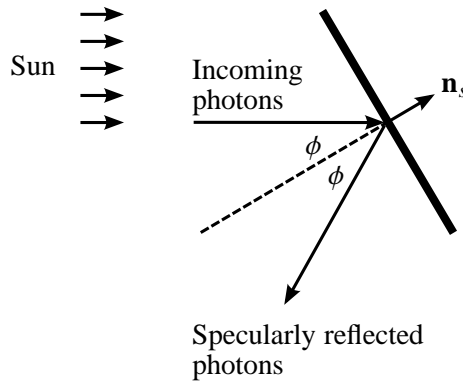


**Figure 2.11:** Solar radiation pressure force acting on an ideal flat surface.

commonly used for numerical simulations (see [Val01]), is adopted,

$$\mathbf{a}_r = (1 + \epsilon) P_{\odot} \frac{A_s \mathbf{r}_S}{m_s r_S^2}, \quad (2.30)$$

in which  $\epsilon$  is the overall surface reflectance. Equation (2.30) is a simplification of the rigorous solar radiation pressure acceleration formula (2.27) under the assumption that the unit vector normal to the surface points always in the direction of the Sun, i.e. the satellite surface is always perpendicular to the incoming radiation. This simplified version is commonly used in orbit determination programs with the option of estimating the surface reflectance  $\epsilon$  as a free parameter. Orbital perturbations due to the solar radiation pressure may thus be accounted for with high precision, even if no details of the satellite structure, orientation and reflec-

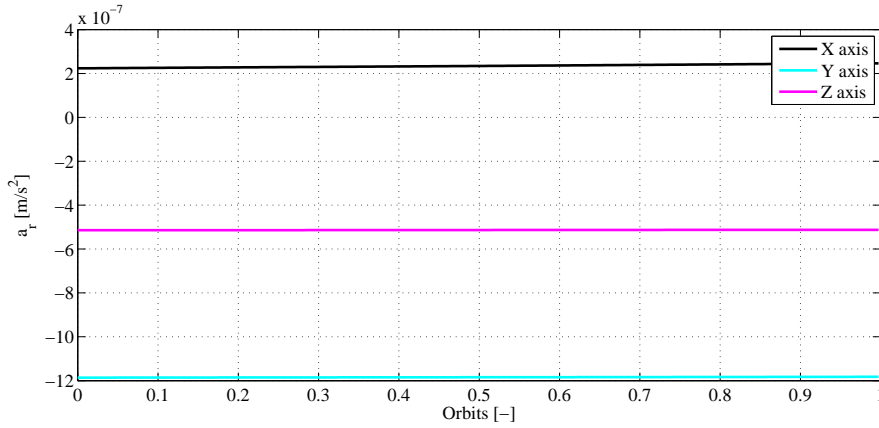


**Figure 2.12:** Perturbing acceleration due to solar radiation pressure, computed during a period of one day.

tivity are known. In the present work a reflectivity coefficient  $\epsilon = 0.3$  is assumed. The acceleration vector  $\mathbf{a}_r$  can be expressed in the ECI reference frame as,

$$\mathbf{a}_r = a_{rX}\mathbf{i}_X + a_{rY}\mathbf{i}_Y + a_{rZ}\mathbf{i}_Z, \quad (2.31)$$

where the components  $a_{rX}$ ,  $a_{rY}$  and  $a_{rZ}$  along the axes can be obtained as the partial derivatives of a pseudo-potential function  $\tilde{V}_r(x, y, z, t)$  of radiation pressure (see [Los07]),

$$a_{rX} = -(1 + \epsilon) P_{\odot} \frac{A_s}{m_s} \frac{x_S - x}{\sqrt{(x_S - x)^2 + (y_S - y)^2 + (z_S - z)^2}}, \quad (2.32a)$$

$$a_{rY} = -(1 + \epsilon) P_{\odot} \frac{A_s}{m_s} \frac{y_S - y}{\sqrt{(y_S - y)^2 + (x_S - x)^2 + (z_S - z)^2}}, \quad (2.32b)$$

$$a_{rZ} = -(1 + \epsilon) P_{\odot} \frac{A_s}{m_s} \frac{z_S - z}{\sqrt{(z_S - z)^2 + (y_S - y)^2 + (x_S - x)^2}}. \quad (2.32c)$$

## 2.5 Translational Dynamics of GEO Satellites

This section introduces the equations that hold the translational dynamics of a GEO satellite. Firstly the fully non linear equations are recalled, then a linearised model is

### 2.5.1 Non-Linear Geostationary Orbit Model

The fully non-linear equations of orbital motion under perturbed conditions are here introduced by means of the Variation Of Parameter (VOP) equations. VOP equations of motion are a system of first-order differential equations that describe the rate of change for the time-varying orbital equinoctial element vector  $\mathbf{x}_{EOE}$ . Referring to [BC71], these equations can be expressed as follows,

$$\dot{\mathbf{x}}_{EOE} = \mathbf{A}_{EOE}(\mathbf{x}_{EOE}) \mathbf{a}_p^{RTN} + \mathbf{b}_{EOE}, \quad (2.33)$$

where  $\mathbf{a}_p^{RTN}$  is the perturbing acceleration vector expressed in the *RTN* reference frame,

$$\mathbf{a}_p = a_{pR} \mathbf{i}_R + a_{pT} \mathbf{i}_T + a_{pN} \mathbf{i}_N. \quad (2.34)$$

The matrix  $\mathbf{A}_{EOE}(\mathbf{x}_{EOE})$ , direct function of the orbital parameters themselves, and the vector  $\mathbf{b}_{EOE}$  are conveniently defined considering the following equations,

$$\frac{da}{dt} = \frac{2a^2}{h} (P_2 \sin L - P_1 \cos L) a_{pR} + \frac{2a^2 p}{h r} a_{pT}, \quad (2.35)$$

$$\begin{aligned} \frac{dP_1}{dt} = & -\frac{p}{h} \cos L a_{pR} + \frac{r}{h} \left[ P_1 + \left(1 + \frac{p}{r}\right) \sin L \right] a_{pT} \\ & - \frac{r}{h} P_2 (Q_1 \cos L - Q_2 \sin L) a_{pN}, \end{aligned} \quad (2.36)$$

$$\begin{aligned} \frac{dP_2}{dt} = & \frac{p}{h} \sin L a_{pR} + \frac{r}{h} \left[ P_2 + \left(1 + \frac{p}{r}\right) \cos L \right] a_{pT} \\ & + \frac{r}{h} P_1 (Q_1 \cos L - Q_2 \sin L) a_{pN}, \end{aligned} \quad (2.37)$$

$$\frac{dQ_1}{dt} = \frac{r}{2h} (1 + Q_1^2 + Q_2^2) \sin L a_{pN}, \quad (2.38)$$

$$\frac{dQ_2}{dt} = \frac{r}{2h} (1 + Q_1^2 + Q_2^2) \cos L a_{pN}, \quad (2.39)$$

$$\begin{aligned} \frac{dl}{dt} = & n - \frac{r}{h} \left\{ \left[ \frac{a}{a+b} \left(\frac{p}{r}\right) (P_1 \sin L + P_2 \cos L) + \frac{2b}{a} \right] a_{pR} \right. \\ & + \frac{a}{a+b} \left(1 + \frac{p}{r}\right) (P_1 \cos L + P_2 \sin L) a_{pT} \\ & \left. + \frac{r}{h} (Q_1 \cos L - Q_2 \sin L) a_{pN} \right\}, \end{aligned} \quad (2.40)$$

where the quantities  $p$ ,  $h$  and  $b$  are defined as follows,

$$p = a(1 - e^2), \quad (2.41)$$

$$h = \sqrt{p\mu_{\oplus}}, \quad (2.42)$$

$$b = a\sqrt{1 - P_1^2 - P_2^2}. \quad (2.43)$$

### 2.5.2 A Linearised Geostationary Orbit Model

The precise orbit propagation means that the fully non-linear equations of orbital motion are numerically integrated to produce the position and velocity vectors at an arbitrary time.

An alternative is to obtain the solution of the relative motion with respect to a known reference orbit [PC93, A<sup>+</sup>10]. The Geostationary Clohessy-Wiltshire (GCW) reference frame described in Section 2.2.4 is centered at the ideal geostationary position with station longitude  $\lambda_G$  and describes a perfect geostationary orbit. This circular orbit can be selected as a reference orbit and the motion in the perturbed orbit can be described with respect to the GCW frame in terms of a set of linear differential equations called the Clohessy-Wiltshire equations [NC05].

The non-linear equations of orbital motion are generally written as in (2.14),

$$\ddot{\mathbf{r}} + \frac{\mu_{\oplus}}{r^3}\mathbf{r} = \mathbf{a}_p, \quad (2.44)$$

where  $\mathbf{r}$  is the position vector of the satellite in the ECI frame and  $\mathbf{a}_p$  is the perturbing accelerations vector which includes, as previously mentioned, the contributes from the Earth's gravitational harmonics, the solar and lunar attraction and the solar radiation pressure.

Referring to Figure 2.13, the relative position vector  $\mathbf{r}_G$  of the satellite with respect to the ideal geostationary orbit is defined as,

$$\mathbf{r}_G = \mathbf{r} - \mathbf{r}_{CW} = x_G\mathbf{i}_{X_G} + y_G\mathbf{i}_{Y_G} + z_G\mathbf{i}_{Z_G}, \quad (2.45)$$

where  $\mathbf{r}_{CW}$  is the position vector of the GCW frame's origin within the fixed ECI frame. Introducing (2.45) in (2.44) and after linearisation about the ideal geosynchronous orbit as a reference, the Clohessy-Wiltshire equations can be written as,

$$\ddot{x}_G = 3\omega_{\oplus}^2 x_G + 2\omega_{\oplus} \dot{y}_G + a_p^{X_G}, \quad (2.46a)$$

$$\ddot{y}_G = -2\omega_{\oplus} \dot{x}_G + a_p^{Y_G}, \quad (2.46b)$$

$$\ddot{z}_G = -\omega_{\oplus}^2 z_G + a_p^{Z_G}, \quad (2.46c)$$

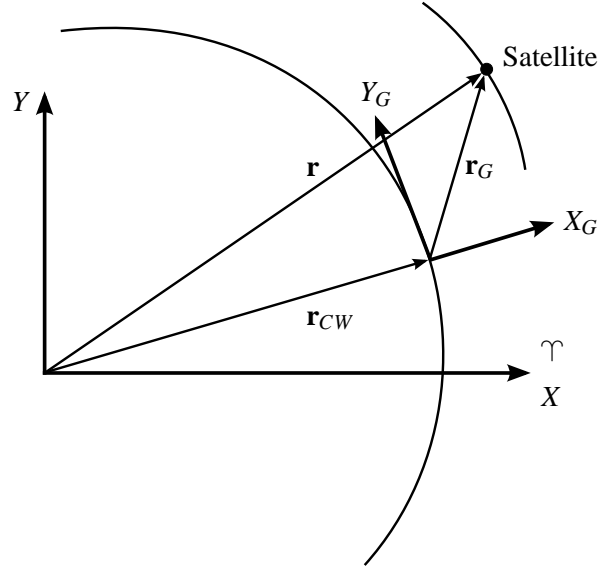


**Figure 2.13:** Satellite motion relative to ECI and GCW reference frames.

in which the components of the disturbing vector need to be expressed relatively to the GCW reference frame. Defining the state vector  $\xi$  as,

$$\xi = [x_G \quad y_G \quad z_G \quad \dot{x}_G \quad \dot{y}_G \quad \dot{z}_G]^T, \quad (2.47)$$

the Clohessy-Wiltshire equations are readily written in their state-space form.

$$\frac{d\xi}{dt} = \mathbf{A}_{CW}\xi + \mathbf{B}_{CW}\mathbf{a}_p^{CW}, \quad (2.48)$$

where,

$$\mathbf{A}_{CW} = \begin{bmatrix} \mathbf{0}_3 & \mathbf{I}_3 \\ 3\omega_\oplus^2 & 0 & 0 & 0 & 2\omega_\oplus & 0 \\ 0 & 0 & 0 & -2\omega_\oplus & 0 & 0 \\ 0 & 0 & -\omega_\oplus^2 & 0 & 0 & 0 \end{bmatrix}, \quad (2.49a)$$

$$\mathbf{B}_{CW} = \begin{bmatrix} \mathbf{0}_3 \\ \mathbf{I}_3 \end{bmatrix}, \quad (2.49b)$$

$$\mathbf{a}_p^{CW} = [a_p^{X_G} \quad a_p^{Y_G} \quad a_p^{Z_G}]^T. \quad (2.49c)$$

The inertial Cartesian components of the Earth's gravity acceleration  $\mathbf{a}_e$ , of the Sun's and Moon's gravity acceleration  $\mathbf{a}_g$  and of the solar radiation pressure  $\mathbf{a}_r$  can be expressed in the GCW Cartesian coordinates by means of the transformation that connects the GCW frame to the ECI frame.

$$\begin{Bmatrix} a_p^X \\ a_p^Y \\ a_p^Z \end{Bmatrix} = \mathcal{R}_3(\Theta + \lambda_G) \begin{Bmatrix} a_p^{X_G} \\ a_p^{Y_G} \\ a_p^{Z_G} \end{Bmatrix}, \quad (2.50)$$

where  $\mathcal{R}_3(\Theta + \lambda_G)$  indicates a rotation of  $\Theta + \lambda_G$  about the third axis of an orthogonal coordinate system.

## 2.6 GEO Satellite Station Keeping

This section describes the satellite station keeping problem underlying the requirements that need to be fulfilled. Moreover a state feedback regulator, designed to meet these constraints, is discussed.

### 2.6.1 GEO Satellite Orbital Requirements

The main requirement of a geostationary satellite consists in having, during its whole life, longitudinal and latitudinal position confined in a deadband box in the  $(\lambda, \varphi)$  plane centered in  $(\lambda_G, 0)$  and with dimensions prescribed by the maximum acceptable deviations in longitude and latitude, namely  $\lambda_{\max}$  and  $\varphi_{\max}$  (see Figure 2.14).

$$-\lambda_{\max} \leq \lambda - \lambda_G \leq \lambda_{\max}, \quad (2.51a)$$

$$-\varphi_{\max} \leq \varphi \leq \varphi_{\max}. \quad (2.51b)$$

A circular confinement area may also be prescribed, but this is usually handled like the previous case by using the square box inscribed in the circle.

The angular constraints on geographic longitude and latitude expressed by (2.51) can also be related to constraints on the displacements of the spacecraft measured in the GCW reference frame, i.e. displacements along the  $X_G$ ,  $Y_G$  and  $Z_G$  axes. Consequently, as depicted in Figure 2.15, an allowed range in longitude given by (2.51a) entails an allowed range along the  $Y_G$  axis given by,

$$-r_G \tan \lambda_{\max} \leq y_G \leq r_G \tan \lambda_{\max}, \quad (2.52)$$

where  $r_G$  is the modulus of the position vector of the center of the GCW frame, that is the radius of the ideal geostationary orbit. On the other hand, an allowed

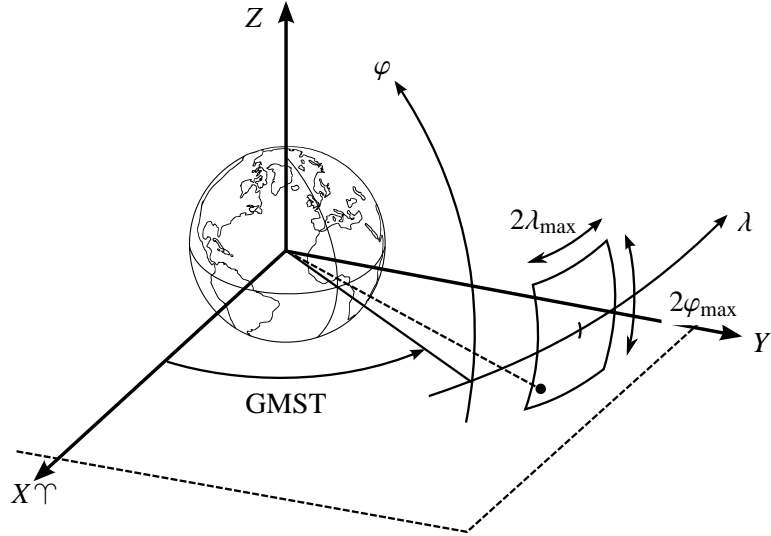


**Figure 2.14:** Deadband rectangular box in  $(\lambda, \varphi)$  plane.

range in latitude given by (2.51b) entails an allowed range along the  $Z_G$  axis given by,

$$-r_G \tan \varphi_{\max} \leq z_G \leq r_G \tan \varphi_{\max}. \quad (2.53)$$

Following the guidelines given in [WR01], in the present work the bounds on longitude and latitude are taken as,

$$\lambda_{\max} = 0.1^\circ, \quad \text{and} \quad \varphi_{\max} = 0.05^\circ.$$

This deadband box in the  $(\lambda, \varphi)$  plane entails a rectangular box in the  $(Y_G, Z_G)$  plane with sides nearly equal to 73.6 km and 36.8 km.

## 2.6.2 Orbit Control System

A state feedback regulator is designed in order to assure that the deviation of the satellite position from the ideal geostationary orbit remains within the prescribed limits. A LQR approach based on the linearised dynamical model of a GEO satellite is chosen.

$$\frac{d\xi}{dt} = \mathbf{A}_{cw}\xi + \mathbf{B}_{cw}\mathbf{a}_c^{cw}. \quad (2.54)$$

Control accelerations  $\mathbf{a}_c^{cw}$  turn out to be proportional to the states  $\xi$  through the gain matrix  $\mathbf{K}_{orb}$ ,

$$\mathbf{a}_c^{cw} = -\mathbf{K}_{orb}\xi. \quad (2.55)$$

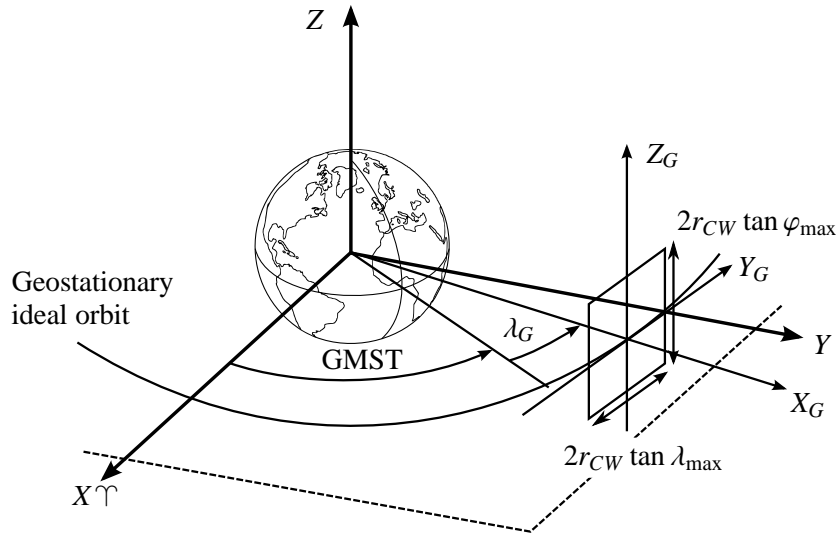


**Figure 2.15:** Tolerance ranges along  $Y_G$  and  $Z_G$  axes of the geostationary GCW reference frame.

The gain matrix is eventually obtained minimizing the quadratic cost function,

$$J_{\text{orb}} = \int_0^{\infty} \left( \boldsymbol{\xi}^T \mathbf{Q}_{\text{orb}} \boldsymbol{\xi} + \mathbf{a}_c^{CW^T} \mathbf{R}_{\text{orb}} \mathbf{a}_c^{CW} \right) dt. \quad (2.56)$$

The weight matrix on the states is a diagonal matrix with different penalties on the positions and on the velocities.

$$\mathbf{Q}_{\text{orb}} = \begin{bmatrix} 3 \times 10^{-14} & 0 & 0 & 0 & 0 & 0 \\ 0 & 3 \times 10^{-14} & 0 & 0 & 0 & 0 \\ 0 & 0 & 3 \times 10^{-14} & 0 & 0 & 0 \\ 0 & 0 & 0 & 10^{-9} & 0 & 0 \\ 0 & 0 & 0 & 0 & 10^{-9} & 0 \\ 0 & 0 & 0 & 0 & 0 & 10^{-9} \end{bmatrix}. \quad (2.57)$$

On the other hand, control actions have all equal penalties, chosen as follows,

$$\mathbf{R}_{\text{orb}} = \begin{bmatrix} 10^6 & 0 & 0 \\ 0 & 10^6 & 0 \\ 0 & 0 & 10^6 \end{bmatrix}. \quad (2.58)$$

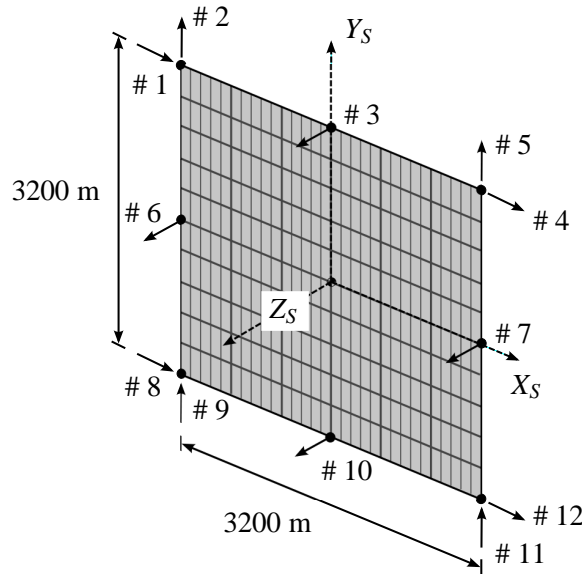


**Figure 2.16:** Actuators pattern employed for the orbital control system.

Using the MATLAB<sup>®</sup> function `lqr` to solve the minimization problem, the gain results as follows,

$$\mathbf{K}_{\text{orb}} = \begin{bmatrix} 0.0000107 & -0.0000006 & 0 & 0.0447490 & 0.0713248 & 0 \\ 0.0000573 & -0.0000021 & 0 & 0.0713248 & 0.4131018 & 0 \\ 0 & 0 & 0.0000003 & 0 & 0 & 0.0750131 \end{bmatrix} \times 10^{-4}. \quad (2.59)$$

The dynamical behaviour of the controlled system is finally held by,

$$\frac{d\xi}{dt} = (\mathbf{A}_{CW} - \mathbf{B}_{CW}\mathbf{K}_{\text{orb}})\xi + \mathbf{B}_{CW}\mathbf{a}_p^{CW}. \quad (2.60)$$

It is already underlined that, due to the significant mass of spacecraft, about  $25 \times 10^6$  kg, a classical station keeping strategies, based on impulsive manoeuvres are expected to be not exploitable. As a consequence the use of electric thrusters, with high specific impulse and throttling capability, becomes mandatory (for further details see Appendix A). In order to provide the necessary resulting control accelerations, the control system is provided with twelve actuation stations, distributed as illustrated in Figure 2.16.

In Figures 2.17 - 2.19 are given the results obtained integrating over twenty orbits

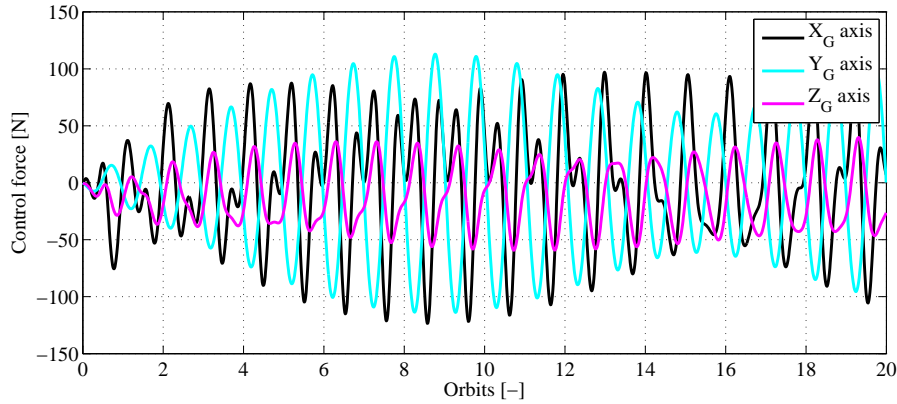


**Figure 2.17:** Time history of the requested control forces expressed in the GCW reference frame.

the vector equation (2.60) with initial conditions equal to,

$$\xi(t_0) = \begin{Bmatrix} x_G(t_0) \\ y_G(t_0) \\ z_G(t_0) \\ \dot{x}_G(t_0) \\ \dot{y}_G(t_0) \\ \dot{z}_G(t_0) \end{Bmatrix} = \begin{Bmatrix} 0 \\ 0 \\ 0 \\ 0 \\ 0 \\ 0 \end{Bmatrix}. \quad (2.61)$$

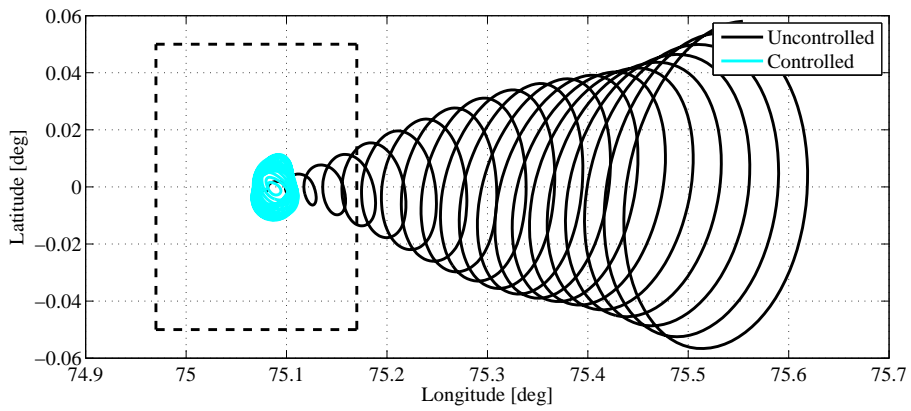
at the initial epoch  $t_0$  corresponding to the date January 1, 2012 at 12<sup>h</sup> 00' 00.0" UTC with the satellite located at nominal longitude  $\lambda_G = 75.07^\circ$  (one of the stable longitude). Orbit control simulation results are obtained taking into account the effects of Earth's oblateness and triaxiality, luni-solar perturbations, 60 N solar pressure force and employing the continuous orbit control described in this section.

In Figure 2.17 is reported the time history of the needed control forces, expressed in the GCW frame. These have to be rotated into a local satellite reference frame in order to properly adjust the actions of each actuator. The rotation is carried out by means of the combination of a series of rotations matrices taking into account the time-varying attitude at each instant. Once expressed into the  $X_S Y_S Z_S$  reference frame, the control forces are equally distributed among the available actuators, four for each direction.

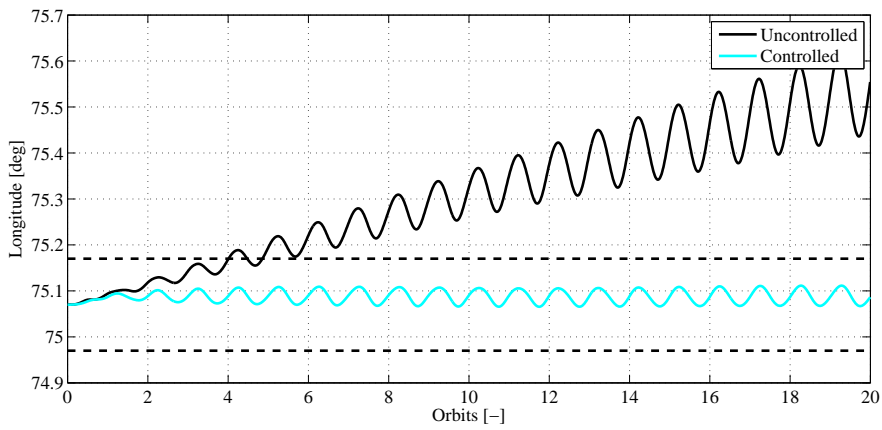
It can be noticed that both the longitude and the latitude are maintained into the prescribed deadbands box defined by  $\lambda_{\max}$  and  $\varphi_{\max}$ . As expected, the longitudinal drift mainly caused by the triaxiality of the Earth is the most prominent perturbation effect and needs a relatively strong control action alongside the  $X_G$  and  $Y_G$  axes. It has to be underlined that these contributions are also required in order

to counteract the disturbances that would increase the eccentricity of the circular orbit. On the other hand, the out of plane disturbances are less significant, this yielding the latitude to be more controllable with less effort.

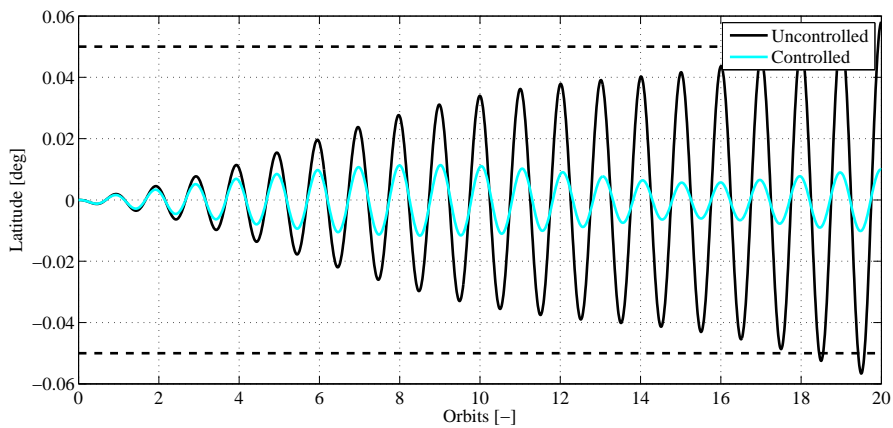
Indeed, Figure 2.19 shows the control actions exerted by the actuators placed in the actuation stations of Figure 2.16. It can be noticed that the needed control actions are of the order of the tens of Newtons at each station with a peak of almost 35 N along the  $X_S$  direction, i.e. actuators # 1, # 4, # 8 and # 12.



(a) Spacecraft trajectory in the  $(\lambda, \varphi)$  plane.

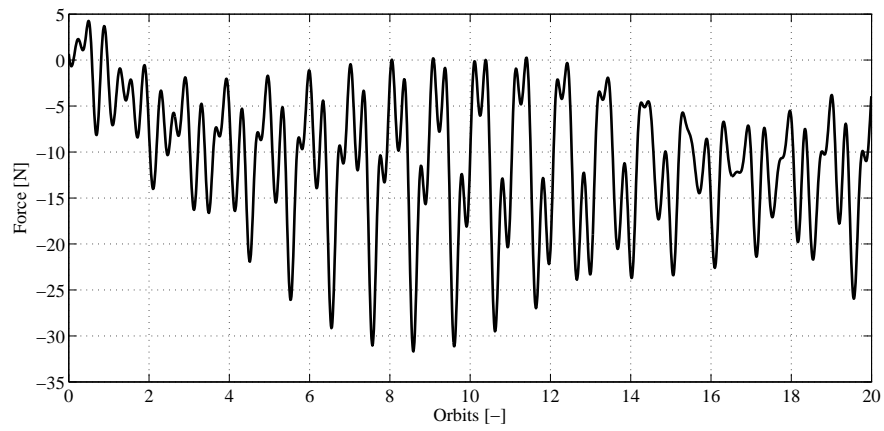


(b) Spacecraft longitude.

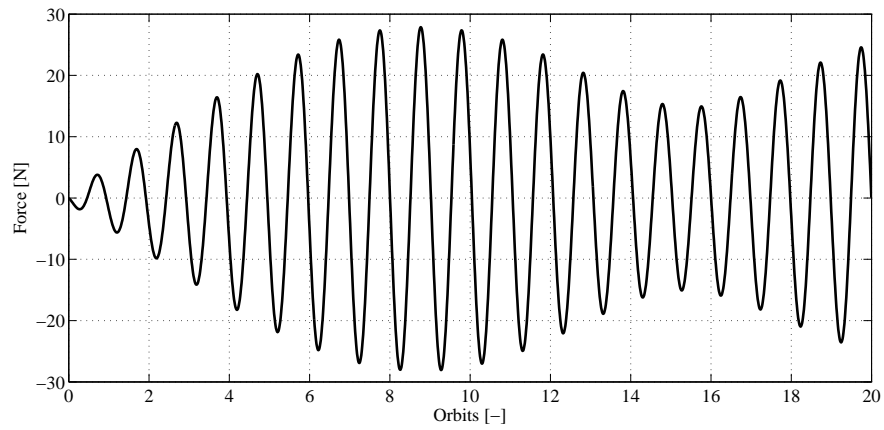


(c) Spacecraft latitude.

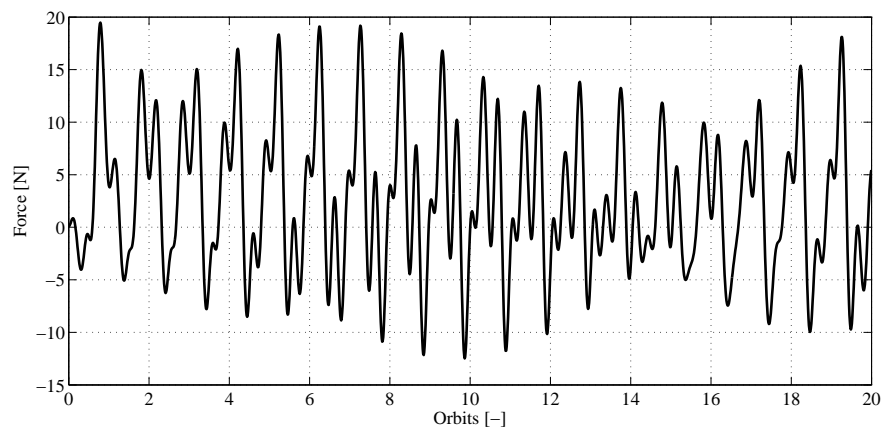
**Figure 2.18:** Time history of spacecraft longitude and latitude obtained integrating the linearised orbital equations over a period of twenty orbits.



(a) Actuators # 1, # 4, # 8 and # 12 along the  $X_S$  direction.



(b) Actuators # 2, # 5, # 9 and # 11 along the  $Y_S$  direction.



(c) Actuators # 3, # 6, # 7 and # 10 along the  $Z_S$  direction.

**Figure 2.19:** Time history of the control forces exerted by actuators.

# Chapter 3

## Attitude dynamics

An attitude control system capable of guaranteeing the operativeness and functionality of the SSP satellite has been designed, in order to investigate the interaction with the structure during the operative life. Operational requirements impose that the SSP satellite must collect as much energy as possible from the Sun, and at the same time transfer continuous power to the Earth by keeping the microwave antenna pointed in the direction of the receiving station.

Once that the most suitable configuration has been chosen, the desired attitude has to be guaranteed as much accurately as possible to improve the transfer of energy to the Earth. Consequently, high control torques have to be expected in order to counteract external disturbances. The major disturbances involved during the operative life are the environmental disturbances such as the solar radiation torque and the gravity gradient torque together with the internal disturbance torques coming from other subsystems. Between all of them the gravity gradient torque is expected to be the most critical. Secondly, the attitude control must show enough authority to bring the SSP satellite from a perturbed to the desired configuration in a time of the order of days. Furthermore, an attitude control system that shows reasonable value of the maximum torque is preferable in order to minimize the mass of the system architecture.

### 3.1 Reference Frames and Coordinate Systems

The reference frames considered for the attitude dynamic and control system are the Body Centered Sun Pointing (BCSP), the Body Centered Sun Facing (BCSF), the Earth Centered Sun Facing (ECSF), the Structural Global (SG) and the Body Principal Inertial (BPI) frames.

The BCSP frame is a non-inertial frame with its origin on the body, defined by the  $X_P Y_P Z_P$  axes.  $X_P$  is a Sun-pointing axis, while  $Y_P$  lies on the equatorial plane.  $Z_P$  is placed such to define a right-handed orthogonal coordinate system with positive

direction towards the North Pole.

The BCSF frame is a non-inertial frame centered on the body defined by  $X_{SF}Y_{SF}Z_{SF}$ . The  $Z_{SF}$  axis is normal to the equatorial plane towards the North Pole, the  $X_{SF}$  axis lies on the plane that includes the Sun and the  $Z_{SF}$  axis.  $Y_{SF}$  is placed such that it completes the right-handed orthogonal coordinate system.

The ECSF frame is a non-inertial Earth centered frame defined by  $X_EY_EZ_E$ . The  $Z_E$  axis is normal to the equatorial plane towards the North, the  $X_E$  axis lies on the plane including the Sun and  $Z_E$ .  $Y_E$  is placed such that it completes the right-handed orthogonal coordinate system.

The ECSF frame is approximately coincident with the BCSF frame, apart that it does not consider the relative motion of the satellite around the Earth. In the worst case, the approximation involves an error of about  $0.016^\circ$  around the  $Z_E$  axis. For this purpose of this work, this error can be neglected and the ECSF and the BCSF frame can be indifferently considered. In particular, the ECSF frame is preferable because it can be simply defined as a rotation of the ECI frame around the  $Z$  axis. The SG frame is defined by  $X_SY_SZ_S$  and it is centered in one of the corner of the square platform of the satellite.  $X_S$  and  $Y_S$  are the in-plane axes along the side-directions, while  $Z_S$  is in the out-of-plane direction such to define a right-handed orthogonal coordinate system. In particular  $X_S$  lies along the side that contains a possible microwave antenna. The frame is centered in one of the corner of the square platform as described in Figure 2.16.

The BPI frame is a non-inertial satellite-barycentric frame, defined by the principal axes of inertia  $X_IY_I Z_I$ , where  $Y_I$  and  $Z_I$  are the in-plane axes, while  $X_I$  is the out-of-plane axis with respect to the planar platform of the satellite. In particular,  $X_I$ ,  $Y_I$  and  $Z_I$  are respectively coincident with  $Z_S$ ,  $X_S$  and  $Y_S$ . The dynamic equations are expressed with respect to this last frame in order to simplify the system.

## 3.2 Attitude configurations

The choice of the attitude configuration should guarantee the effectiveness of the mission and the feasibility of a possible attitude control system at the same time. Although the main goal is to collect as much energy as possible by keeping the solar array always perpendicular to the Sun, and to provide continuous power to the Earth, it's necessary to analyse the possibility of designing it.

For this reason two main configurations have been compared: the SP and the SF configurations, which differ in terms of the desired orientation. Between them, two options should also be analysed concerning the independent degrees of freedom of a possible microwave transmitting system: the Independent Transmitter Pointing (ITP) and One Axis Rotating Transmitter (OART) configuration. The

choice of the final configuration should take into account the tight requirements on the pointing accuracy.

### 3.2.1 Attitude Dynamics Requirements

The solar array pointing accuracy is  $\pm 0.5^\circ$  around  $Y_C W$  and  $Z_C W$ . Although the latter does not seem to be very restrictive, the pointing accuracy of the attitude control is driven by a possible microwave beam pointing requirements. In order to transfer the energy to the receiving station without excessive loss, the beam pointing error should not be more than  $\pm 0.08^\circ$  ([WR01]).

Secondly the attitude control should have enough authority to extinguish an initial attitude error of  $\pm 10^\circ$  around  $X_I$ ,  $Y_I$  and  $Z_I$  by a time of the order of some orbits in the presence of all the disturbances [WR01].

### 3.2.2 The Sun Pointing (SP) Configuration

The SP configuration is obtained by keeping the BPI frame coincident with the BCSP frame. This configuration is the most promising in terms of operativeness since the solar arrays are kept always perpendicular to the solar rays. At the same time it shows some drawbacks that makes this choice hard to be really realized.

First of all a possible microwave transmitting system should be always oriented towards the receiving station on the Earth by large rotation around three axes. This choice may be improbable considering the large mass involved (see Chapter 1).

Secondly the gravity gradient torque, is expected to have considerable component around all the directions of the BPI frame. For these reasons the SP configuration is not considered to be the most suitable configuration.

### 3.2.3 The Sun Facing (SF) Configuration

The SF configuration is obtained by keeping the BPI frame coincident with the BCSF frame. The solar arrays are not exactly perpendicular to the Sun rays during the whole orbit of the Earth around the Sun, except at the equinoxes.

The  $Z_{SF}$  axis is always perpendicular to the equatorial plane so that the microwave beam antenna system should be oriented to the receiving station by rotating the transmitting system just around the  $Z_{SF}$  axis.

Beyond the fact that the attitude control appears to be more easily designed, the gravity gradient torque shows its major contribution just around the  $Z_{SF}$  axis. In the end the SF configuration is chosen to be the reference configuration for the attitude control design ([WR01]).

### 3.2.4 The Transmitting Pointing Configurations

Even though the microwave transmitting system has not been analysed in detail, the attitude control should guarantee the beam pointing accuracy of  $\pm 0.08^\circ$ .

In the ITP configuration, the attitude control of the whole SSP satellite may be designed to satisfy the  $\pm 0.5^\circ$  accuracy around  $Y_C W$  and  $Z_C W$ , while an independent attitude control for the microwave transmitting system should provide the finest pointing requirement of  $\pm 0.08^\circ$ . On the other hand, the OART configuration employs an attitude control system for the entire SSP satellite to satisfy the  $\pm 0.08^\circ$  accuracy. A possible microwave transmitting system is able to rotate around the  $Z_C W$  axis tracking the receiving station on the Earth.

Although the OART configuration seems to be the most simple in terms of architecture simplicity, it is necessary to verify the feasibility in a plausible operative situation.

## 3.3 Attitude State Representation

The principal momentum of inertia are:

$$I_x = 4.9023 \times 10^{13} \text{ kgm}^2 \quad (3.1a)$$

$$I_y = 2.4492 \times 10^{13} \text{ kgm}^2 \quad (3.1b)$$

$$I_z = 2.4532 \times 10^{13} \text{ kgm}^2 \quad (3.1c)$$

$$(3.1d)$$

The Euler Equations of Motion (EEM) expressed in the BPI frame are [Wer99]:

$$I_x \dot{\omega}_{x_I} + (I_{z_I} - I_{y_I}) \omega_{z_I} \omega_{y_I} = M_{x_I}^c + M_{x_I}^d \quad (3.2a)$$

$$I_y \dot{\omega}_{y_I} + (I_{x_I} - I_{z_I}) \omega_{x_I} \omega_{z_I} = M_{y_I}^c + M_{y_I}^d \quad (3.2b)$$

$$I_z \dot{\omega}_{z_I} + (I_{y_I} - I_{x_I}) \omega_{y_I} \omega_{x_I} = M_{z_I}^c + M_{z_I}^d \quad (3.2c)$$

where  $\omega_{x_I}$ ,  $\omega_{y_I}$  and  $\omega_{z_I}$  are the angular velocities in the BPI frame,  $M_{x_I}^c$ ,  $M_{y_I}^c$  and  $M_{z_I}^c$  are the attitude control torques, while  $M_{x_I}^d$ ,  $M_{y_I}^d$  and  $M_{z_I}^d$  are the disturbance torques in the BPI frame.

The BPI frame can be related to the BCSF frame by a rotational matrix  $\mathbf{A}$  such that:

$$\mathbf{v}_{BPI} = \mathbf{A} \cdot \mathbf{v}_{BCSF} \quad (3.3)$$

where  $\mathbf{v}_{BPI}$  and  $\mathbf{v}_{BCSF}$  are respectively the vectors in the BPI and the BCSF frame. Assuming that the SSP satellite is kept in the nominal configuration, the BPI frame can be considered as the BCSF frame perturbed by small rotations. If an Euler

angles parametrization with different indexes is used, the  $\mathbf{A}$  matrix can be written as [Wer99]:

$$\mathbf{A} = \begin{bmatrix} 1 & \alpha_z & -\alpha_y \\ -\alpha_z & 1 & \alpha_x \\ \alpha_y & -\alpha_x & 1 \end{bmatrix} \quad (3.4)$$

where  $\alpha_x$ ,  $\alpha_y$  and  $\alpha_z$  are small rotations respectively around  $X_E$ ,  $Y_E$  and  $Z_E$ . Considering that the ECSF frame is rotating around the  $Z$  axis with the angular velocity of the Earth with respect to the Sun ( $n_\oplus$ ), the cinematic equations become:

$$\begin{Bmatrix} \omega_x \\ \omega_y \\ \omega_z \end{Bmatrix} = \begin{bmatrix} 1 & \alpha_z & -\alpha_y \\ -\alpha_z & 1 & \alpha_x \\ \alpha_y & -\alpha_x & 1 \end{bmatrix} \begin{Bmatrix} \dot{\alpha}_x \\ \dot{\alpha}_y \\ \dot{\alpha}_z + n_\oplus \end{Bmatrix}. \quad (3.5)$$

If the second order terms are neglected, Equations 3.5 can be simplified as follow:

$$\omega_x = \dot{\alpha}_x - \alpha_y n_\oplus \quad (3.6a)$$

$$\omega_y = \dot{\alpha}_y + \alpha_x n_\oplus \quad (3.6b)$$

$$\omega_z = \dot{\alpha}_z + n_\oplus \quad (3.6c)$$

Deriving Equations 3.6 with respect to time:

$$\dot{\omega}_x = \ddot{\alpha}_x - \dot{\alpha}_y n_\oplus \quad (3.7a)$$

$$\dot{\omega}_y = \ddot{\alpha}_y + \dot{\alpha}_x n_\oplus \quad (3.7b)$$

$$\dot{\omega}_z = \ddot{\alpha}_z \quad (3.7c)$$

Using Equations 3.7, Equations 3.2 yield:

$$I_x \ddot{\alpha}_x + n_\oplus (I_z - I_y - I_x) \dot{\alpha}_y + n_\oplus^2 (I_z - I_y) \alpha_x = M_{x_I}^c + M_{x_I}^d \quad (3.8a)$$

$$I_y \ddot{\alpha}_y + n_\oplus (I_x + I_y - I_z) \dot{\alpha}_x + n_\oplus^2 (I_z - I_x) \alpha_y = M_{y_I}^c + M_{y_I}^d \quad (3.8b)$$

$$I_z \ddot{\alpha}_z = M_{z_I}^c + M_{z_I}^d \quad (3.8c)$$

The state space realization for the attitude dynamic is:

$$\dot{\bar{\alpha}} = \mathbf{A}_{\text{att}} \bar{\alpha} + \mathbf{B}_{\text{uatt}} \mathbf{M}_I^d + \mathbf{B}_{\text{datt}} \mathbf{M}_I^c \quad (3.9a)$$

where:

$$\bar{\alpha} = \begin{Bmatrix} \alpha \\ \dot{\alpha} \end{Bmatrix} = \begin{Bmatrix} \alpha_x \\ \alpha_y \\ \alpha_z \\ \dot{\alpha}_x \\ \dot{\alpha}_y \\ \dot{\alpha}_z \end{Bmatrix} \quad \mathbf{B}_{\mathbf{u}_{\text{att}}} = \mathbf{B}_{\mathbf{d}_{\text{att}}} = \begin{bmatrix} 0 & 0 & 0 \\ 0 & 0 & 0 \\ 0 & 0 & 0 \\ 1/I_x & 0 & 0 \\ 0 & 1/I_y & 0 \\ 0 & 0 & 1/I_z \end{bmatrix} \quad (3.10)$$

$$\mathbf{A}_{\text{att}} = \begin{bmatrix} 0 & 0 & 0 & 1 & 0 & 0 \\ 0 & 0 & 0 & 0 & 1 & 0 \\ 0 & 0 & 0 & 0 & 0 & 1 \\ \frac{-n_{\oplus}^2(I_z - I_y)}{I_x} & 0 & 0 & 0 & \frac{-n_{\oplus}(I_z - I_y - I_x)}{I_x} & 0 \\ 0 & \frac{-n_{\oplus}^2(I_z - I_x)}{I_y} & 0 & \frac{-n_{\oplus}(I_x + I_y - I_z)}{I_y} & 0 & 0 \\ 0 & 0 & 0 & 0 & 0 & 0 \end{bmatrix} \quad (3.11)$$

### 3.4 Environmental Disturbances

The environmental disturbances considered for the attitude control design are the gravity gradient torque and the solar radiation torque. They all have to be evaluated in the BPI frame. The torque caused by the counter-reaction force due to the microwave transmission has been neglected since the transmitting system has not been considered in the present work.

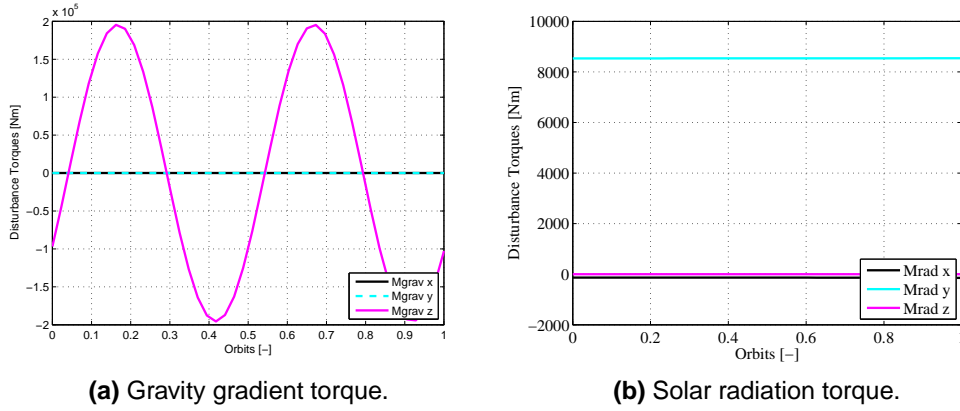


Figure 3.1: Environmental torques.

### 3.4.1 The Gravity Gradient Torque

The gravity gradient torque results from the not uniform Earth's gravitational field acting on the body. In BPI frame it can be expressed as:

$$M_{x_I}^g = \frac{3\mu_{\oplus}}{r^3} (I_z - I_y) c_{z_I} c_{y_I} \quad (3.12a)$$

$$M_{y_I}^g = \frac{3\mu_{\oplus}}{r^3} (I_x - I_z) c_{x_I} c_{z_I} \quad (3.12b)$$

$$M_{z_I}^g = \frac{3\mu_{\oplus}}{r^3} (I_y - I_x) c_{y_I} c_{x_I} \quad (3.12c)$$

where  $c_{x_I}$ ,  $c_{y_I}$  and  $c_{z_I}$  are the component of the radial versor from the Earth to the satellite, and  $M_{x_I}^g$ ,  $M_{y_I}^g$  and  $M_{z_I}^g$  are the components of the gravity gradient torque [Wer99]. Since the BPI frame should be kept about the BCSF frame with a small tolerance,  $c_{z_I}$  is expected to be very small, so that in the nominal configuration the major contribution of the gravity gradient torque should be around the  $Z_I$  axis.

Figure 3.1a shows the gravity gradient torque disturbance  $\mathbf{M}_I^{\text{grav}}$  in the BPI frame in the nominal configuration. As expected, the disturbance torque results to be periodic around the pitch axis. As a consequence a cyclic disturbance suppression control method may be implemented.

### 3.4.2 The Solar Radiation Torque

Despite the importance of the cyclic pitch gravity-gradient torque, the solar radiation torque is more detrimental than one may expects because of the large value of the area-to-mass ratio of the SSP satellite.

The solar radiation pressure acting on a satellite orbiting around the Earth can be considered to be constant and equal to  $P^{\odot} = 4.5298 \times 10^{-6}$  Pa. Considering the

satellite area equal to  $A_{\text{sat}} = 10240000 \text{ m}^2$ , the solar radiation force  $\mathbf{F}_I^\odot$  is a vector expressed in the BPI frame acting on the center of pressure of the SSP satellite along the Sun-satellite direction. Its modulus is equal to  $F_I^\odot = P^\odot A_{\text{sat}}$ .

In the nominal condition the center of pressure is almost coincident with the center of mass, so that the solar radiation force does not provide a considerable torque. However, if uncertainties of 20 m are imposed on the center of pressure and center of mass [WR01], the solar radiation torque can be expressed as:

$$\mathbf{M}_I^\odot = \mathbf{F}_I^\odot \wedge \mathbf{v}_{\text{pm}_I} \quad (3.13)$$

where  $\mathbf{v}_{\text{pm}}$  is the position vector from the center of pressure to the center of mass with components in the  $Y_I Z_I$  plane. Figure 3.1b shows the solar radiation torque disturbance  $\mathbf{M}_I^\odot$  in the BPI frame. As expected, in presence of a constant offset between the center of mass and pressure, a constant torque should be guaranteed.

### 3.5 Attitude Uncontrolled Motion

The attitude uncontrolled motion of the SSP satellite should be considered in order to estimate the necessity of an active attitude control. The starting attitude error configuration is assumed equal to zero in terms of angle and their derivatives with respect to the GCW. That is to impose  $\bar{\alpha}_I = \bar{\alpha}_{0_I}$  with

$$\bar{\alpha}_{0_I} = [0 \ 0 \ 0 \ 0 \ 0 \ 0]^T. \quad (3.14)$$

Figure 3.2 shows the behaviour of  $\alpha_{x_I}$ ,  $\alpha_{y_I}$  and  $\alpha_{z_I}$  due to the environmental disturbance torques. After just a simulation time of a small fraction of orbit, the tolerance accuracy is no longer not satisfied. Although Equations 3.9 are linearised about zero, and the approximation is not effective in case of large angles, it is evident that an active attitude control system is required.

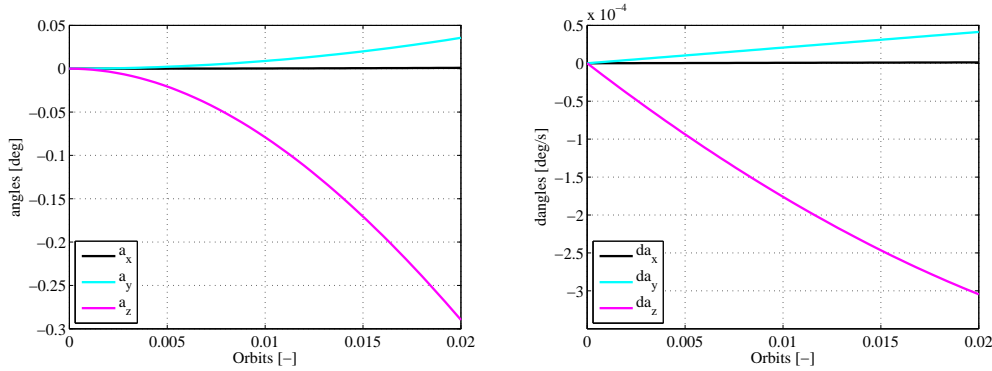
### 3.6 Attitude Control Regulators

Two kind of attitude control regulators have been designed in order to assure that the error angles don't exceed the tolerances: the classical PID regulator, and the optimal LQR.

#### 3.6.1 Proportional Integrative Derivative Regulator

The PID regulator generates a control torque  $M_j^{\text{PID}}$  around the  $j$  axis, as the sum of a proportional, derivative and integral contributions of the error angle  $\alpha_{j_I}$ .

$$M_j^{\text{PID}} = K_{p_j} \alpha_{j_I} + K_{i_j} \int_0^T \alpha_{j_I} dt + K_{d_j} \frac{d\alpha_{j_I}}{dt} \quad (3.15a)$$



(a) Angles behaviours in the uncontrolled dy- (b) Angle derivatives behaviours in the un-  
namics. controlled dynamics.

**Figure 3.2:** Full attitude state in the uncontrolled dynamics.

where the proportional, integral and derivative control parameters are chosen such that:

$$K_{pj} = I_j(\xi_j\omega_{0j}\omega_{1j} + \omega_{0j}^2) \quad (3.16a)$$

$$K_{ij} = I_j\omega_{0j}\omega_{1j}^2 \quad (3.16b)$$

$$K_{dj} = I_j(2\omega_{0j}\xi_j + \omega_{1j}) \quad (3.16c)$$

with  $I_j$  the principal momentum of inertia.

### 3.6.2 Optimal Linear Quadratic Regulator

The LQR has been considered in order to weigh the performances and the control inputs distinctly, and to guarantee robustness of the closed loop system. The state may be available by an estimator since the dimension of the full state is not prohibitive. However, for simplicity, the full state is considered to be known.

The performance to be minimized is the state vector  $\bar{\alpha}_1$  since the pointing accuracy is given in the GCW frame.

The control torques  $\mathbf{M}_I^c$  in the BPI frame turn out to be proportional to the states  $\bar{\alpha}$  through the gain matrix  $\mathbf{K}_{att}$ ,

$$\mathbf{M}_I^c = -\mathbf{K}_{att}\bar{\alpha}. \quad (3.17)$$

The gain matrix is eventually obtained minimizing the quadratic cost function,

$$J = \int_0^\infty (\bar{\alpha}^T \mathbf{Q}_{att} \bar{\alpha} + \mathbf{M}_I^c{}^T \mathbf{R}_{att} \mathbf{M}_I^c) dt. \quad (3.18)$$

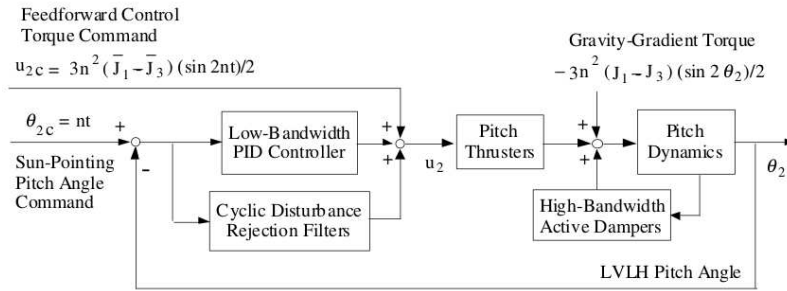


**Figure 3.3:** The cyclic-disturbance accommodating control for the  $Z_E$  axis [WR01]

The MATLAB<sup>®</sup> function `lqr` has been used to solve the minimization problem, and to find the resulting gain. Substituting Equation 3.17 in Equation 3.9, the final closed loop system yields:

$$\frac{d\bar{\alpha}}{dt} = (\mathbf{A}_{\text{att}} - \mathbf{B}_{\text{uatt}}\mathbf{K}_{\text{att}})\bar{\alpha} + \mathbf{B}_{\text{datt}}\mathbf{M}_{\text{I}}^{\text{d}} \quad (3.19)$$

### 3.6.3 Cyclic Disturbance Rejection

In order to satisfy the  $\pm 0.08^\circ$  pointing accuracy in the presence of large external disturbances around the  $Z_I$  axis, the attitude control system utilizes a concept of cyclic-disturbance accommodating control. Since the gravity gradient torque is expected to be cyclic with a period of two times a day, a feedforward control torque command is introduced as follow:

$$M_{z_I}^f = \frac{3\mu_{\oplus}}{r^3} (I_y - I_x) \sin(2n_{\oplus} + \phi)/2 \quad (3.20)$$

where  $\phi$  depends on the initial attitude of the satellite with respect to the Earth. In addition, a second-order-filter with a cut-off frequency equal to the main frequency of the disturbance is placed in the control loop as shown in Figure 3.3. The task of the filter is to attenuate the effect of the gravity gradient torque around the  $Z_I$  axis using the internal modelling of the disturbance [WR01].

## 3.7 Attitude Control System

The simulations have been carried out in two different conditions: the Independent Transmitter Pointing (ITP) and the One Axis Rotating Transmitter (OART) in the presence of the environmental disturbances. The same control architecture described in Section 2.6.2 is considered to be the reference architecture for the attitude control system. In particular, as shown in Figure 2.16, in the absence of

**Table 3.1:** PID regulator parameters

	$X_I$ axis	$Y_I$ axis	$Z_I$ axis
$\omega_0$	$n_{\text{sat}} \times 3$	$n_{\text{sat}} \times 3$	$n_{\text{sat}} \times 3$
$\omega_1$	$n_{\text{sat}} \times 1$	$n_{\text{sat}} \times 1$	$n_{\text{sat}} \times 1$
$\xi$	0.7	0.7	0.7

geometrical/configuration uncertainties, actuators #1, #2, #14, #5, #8, #9, #11 and #12 are assigned to provide the required control torque around the  $X_I$  axis, actuators #3 and #10 around  $Y_I$ , while actuators #5 and #6 are assigned to provide the torque around  $Z_I$ .

Although the location of the actuators is not optimized to minimize the interaction with the orbit and the structural system, this architecture has some interesting advantages for this preliminary study. First of all it can provide independent control torques around each principal axes of inertia, secondly it maximizes the lever arm in each direction, so that it minimizes the force required for each actuator. One of the principal drawback is a possible strong interaction with the structure, caused by an expected high modal participation at the corners of the structure. Thus, the structural control interaction with respect to the orbit and attitude control systems appears to be critical. The control parameters for the PID regulator are shown in Table 3.1 while the matrices  $\mathbf{Q}_{\text{att}}$  and  $\mathbf{R}_{\text{att}}$  have been chosen to be:

$$\mathbf{Q}_{\text{att}} = \begin{bmatrix} 1 \times 10^{13} & 0 & 0 & 0 & 0 & 0 \\ 0 & 3 \times 10^{13} & 0 & 0 & 0 & 0 \\ 0 & 0 & 4 \times 10^{13} & 0 & 0 & 0 \\ 0 & 0 & 0 & 1 \times 10^{13} & 0 & 0 \\ 0 & 0 & 0 & 0 & 3 \times 10^{13} & 0 \\ 0 & 0 & 0 & 0 & 0 & 4 \times 10^{13} \end{bmatrix} \quad (3.21)$$

$$\mathbf{R}_{\text{att}} = \begin{bmatrix} 10 & 0 & 0 \\ 0 & 10 & 0 \\ 0 & 0 & 10 \end{bmatrix} \quad (3.22)$$

### 3.7.1 The Attitude Zero Initial Condition (AZIC)

In the AZIC, the starting angles are considered equal to zero. The simulations are carried out using the PID control parameters of Table 3.1 and the LQR penalty matrices of Equation 3.21. Both the controllers are capable to keep the angles into the specific tolerance of  $0.08^\circ$  (Figure 3.4). The PID regulator yield an initial high elongation, that may be adjusted by a better choice of the control parameters.

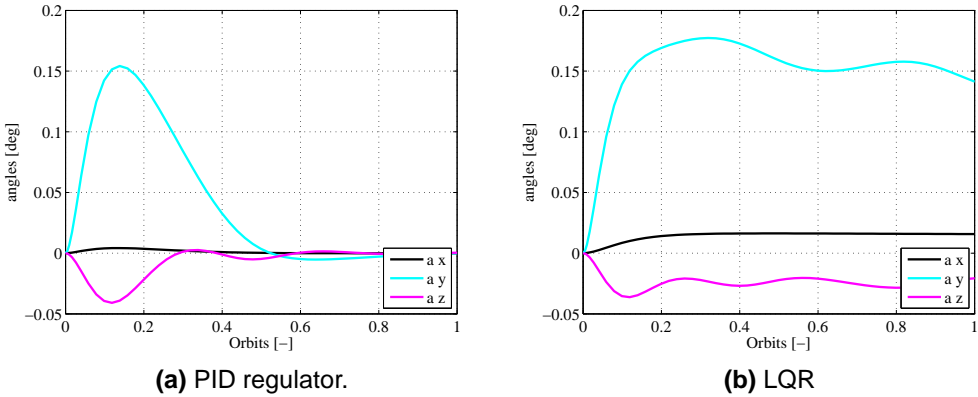


Figure 3.4:  $\alpha$  in the ZIC.

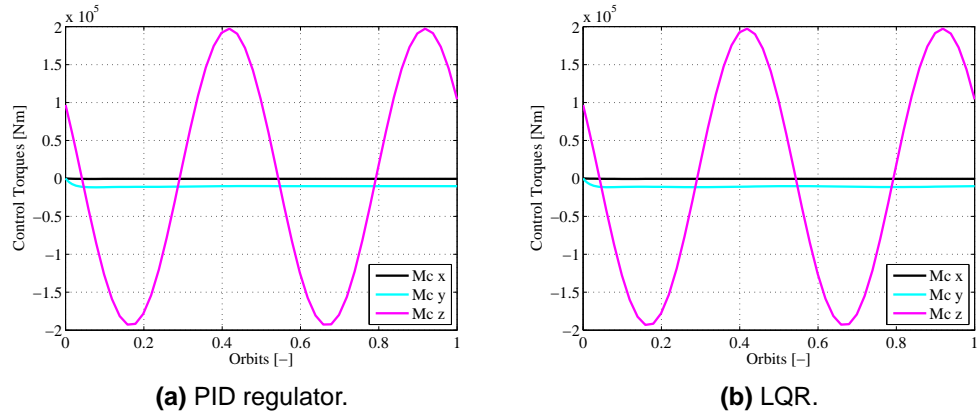


Figure 3.5: Control torque in the AZIC

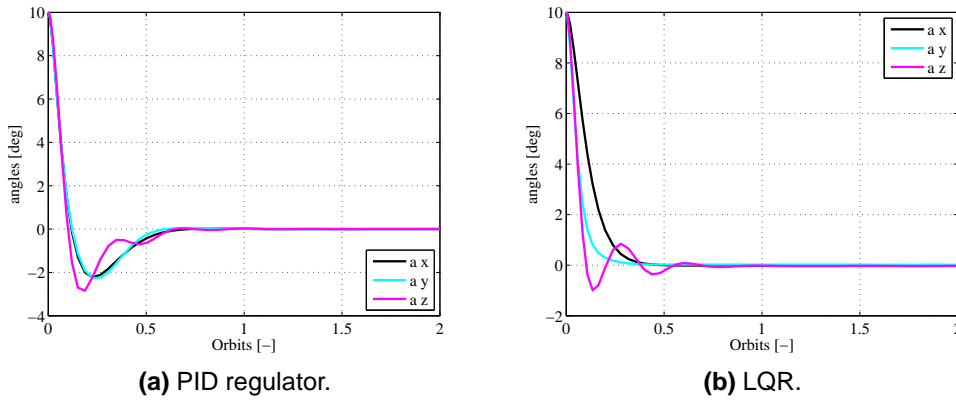


Figure 3.6:  $\alpha$  in the APIC.

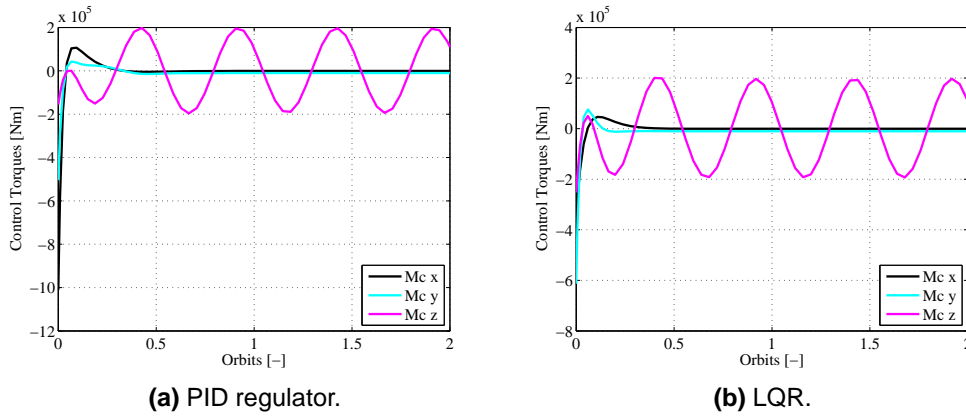
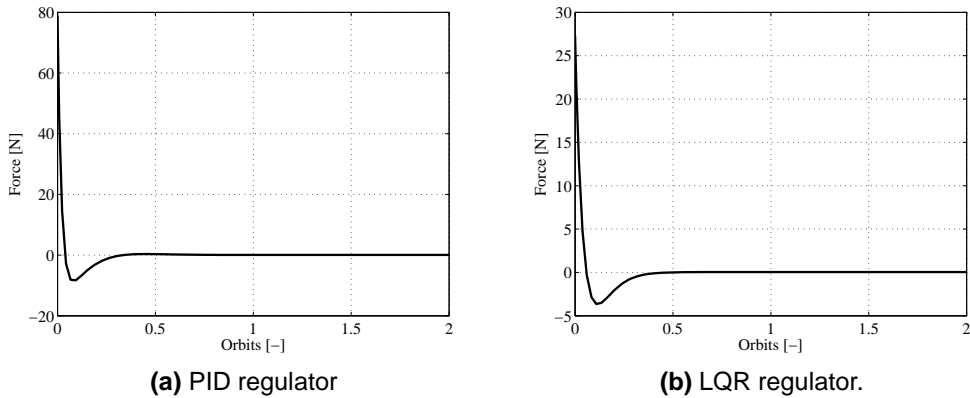


Figure 3.7: Control torque in the APIC.

Contrary, the LQR produces a smoother action on the attitude angles, however it appears that an integral control action is needed to remove the regime errors. Despite this, the performances of the controllers are acceptable for the purpose of a preliminary study of the structural and control interaction. Moreover, the control torques required for both the PID regulator and the LQR are comparable (Figure 3.5). As expected, in the nominal operative life of the satellite a significant torque around the  $Z_I$  axis is required, in order to counteract the high gravity gradient torque.

### 3.7.2 Attitude Perturbed Initial Condition (APIC)

In the APIC, a starting error of  $10^\circ$  have been imposed to  $\alpha_{x_I}$ ,  $\alpha_{y_I}$  and  $\alpha_{z_I}$  and zero initial conditions to their derivatives. Figure 3.6 show the behaviours of the angles  $\alpha_I$  resulting from the LQR and the PID regulators actions. Both the controllers



**Figure 3.8:** Actuator #1 in the APIC.

have enough authority to bring the angles back into the tolerance of  $\pm 0.08^\circ$  in less than one orbit from the same starting initial conditions. As expected, the control torques (Figure 3.7) are much higher than those required in the nominal operative life of the satellite (see Section 3.7.1). However, although both the controllers are capable to restore the nominal configuration in a time of the order of the orbit, the distribution of penalties imposed to the LQR yields a lower control action. As a consequence, the same considerations may be referred to the actuator actions. For example, considering the actuator #1, Figure 3.8 shows that a higher level of force is required by the PID regulator. In the end, although the two controllers show comparable behaviour, the LQR is preferable since it permits to better impose penalties on the states and the control inputs. Moreover, it may be further integrated with the already designed LQR orbit control.

# Chapter 4

## Structural Model

In this chapter, a FE model of the Abacus-like structure is developed as a bidimensional frame and constituted by beam elements. The geometric properties are chosen such that some important features of the reference Abacus concept, inertial characteristics and the first modal frequency, are met [WR01]. This model is used to carry out the modal analysis of the structure and the results are compared with those obtained from an analogous model developed with another software for finite element analysis. The resulting second order dynamical system is then transformed into the first order system of equations representing the state-space realization of the dynamical model.

### 4.1 Finite Element Model

#### 4.1.1 The Bidimensional Reference Configuration

This section deals with the development of a FE model of the Abacus satellite concept. In order to easily study the dynamics and control of the structure, a MATLAB<sup>®</sup> routine has been developed to determine the mass, damping and stiffness matrices of the satellite.

The ARF satellite is characterized by a square platform and a microwave transmitting system placed along a side of the array platform as shown in Figure 1.3. The latter is made of a 500 m diameter antenna and an earth-tracking reflector (500×700 m) with a total mass of about  $25 \times 10^6$  kg. The square platform is mainly a bidimensional frame which supports the solar arrays plane ( $3.2 \times 3.2$  km) composed itself by smaller sub-panels ( $40 \times 200$  m) as depicted in Figure 4.1. The mass of the square platform is  $21 \times 10^6$  kg, that results to a total satellite mass of  $24.8 \times 10^6$  kg.

According to the purpose of the present work, that is a preliminary study on an orbit and attitude control together with a vibration suppression system, the mi-

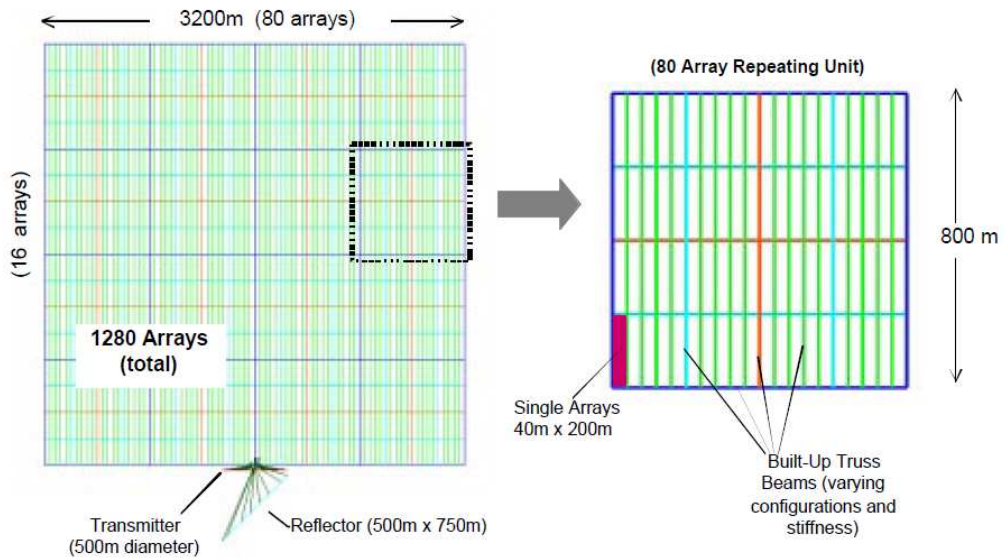


**Figure 4.1:** The ARF satellite modelled as a frame structure.

crowave transmitting system has been neglected. Moreover, the square platform has been modelled by straight elements connected together and organized in a bidimensional frame configuration. The element cross-sections properties have not been available, thus, they have been calculated iteratively such that the behaviour of the global structure is comparable with that of the reference model (see Section 4.1.3).

#### 4.1.2 The Structural Reference Systems

Two reference systems have been employed in the FE modelling: the Structural Global (SG) frame is referred to the global structure, while the Structural Local (SL) frame has been adopted to express the equilibrium equations for each element.

The SG frame is defined by  $X_S Y_S Z_S$  and it is centered in one of the corner of the square platform of the satellite.  $X_S$  and  $Y_S$  are the in-plane axes along the side-directions, while  $Z_S$  is in the out-of-plane direction such as to define a right-handed orthogonal coordinate system. The SL frame is the local coordinate system defined by  $X_L Y_L Z_L$ . It is placed in the geometric-center of the element cross-section. The  $Y_L$  and  $Z_L$  axes are in the cross-section plane with  $Y_L$  coincident to  $Z_S$ , while  $X_L$  completes a right-handed orthogonal coordinate system.

**Table 4.1:** Comparison between the global structural parameters.

	Model parameters	Reference parameters
Total mass [kg]	$2.465 \times 10^7$	$2.480 \times 10^7$
$f_{el}$ [Hz]	0.001807	0.001800
$I_x$ [kgm <sup>2</sup> ]	$4.9023 \times 10^{13}$	$4.6 \times 10^{13}$
$I_y$ [kgm <sup>2</sup> ]	$2.4492 \times 10^{13}$	$2.8 \times 10^{13}$
$I_z$ [kgm <sup>2</sup> ]	$2.4532 \times 10^{13}$	$1.8 \times 10^{13}$

**Table 4.2:** Elemental cross-section properties.

	Prop. A	Prop. B	Prop. C	Prop. D
A [m <sup>2</sup> ]	0.1907086	0.0515676	0.0139439	0.0037704
$I_{x_{sec}}$ [m <sup>4</sup> ]	3.85606102	0.28194037	0.02061440	0.00150725
$I_{y_{sec}}$ [m <sup>4</sup> ]	1.92803051	0.14097019	0.01030720	0.00075362
$I_{z_{sec}}$ [m <sup>4</sup> ]	1.92803051	0.14097019	0.01030720	0.00075362

### 4.1.3 The Finite Element Model

The bidimensional frame structure is built up by a series of straight beam element. The degrees of freedom for each element are three displacements and three rotations of the extremity nodes. Thus the total number of degrees of freedom for each element is 12 [LQ03].

The beam elements are placed to form a grid in the  $X_S Y_S$  plane, with 80 elements along  $X_S$  and 16 elements along  $Y_S$ . The nodes are exactly placed at the every intersection of the grid [WR01].

The beams are supposed to be made of a uniform and isotropic material. Expecting a very high slenderness of the sub-beams, the Aluminium 7075 have been chosen for its good behaviour in compression-stability between the other metal materials, and for its proven reliability in the space field. The composite materials have been temporarily excluded for their high cost and unproven behaviour. The Young modulus for the Aluminium 7075 is assumed to be  $E = 71$  GPa, the Poisson's ratio  $\nu = 0.33$  and density  $\rho = 2768$ .

Four different cross-section properties have been identified. They have been iteratively calculated in order to obtain values for the total mass, the first modal frequency and the principal moments of inertia of the whole satellite comparable with those of the ARF reference concept. Table 4.2 shows the cross-section properties which give the value of total mass, first modal frequency and principal moments of inertia of the whole satellite listed in Table 4.1.

#### 4.1.4 Dynamic Problem

The dynamic problem is written as:

$$\mathbf{M}\ddot{\mathbf{A}} + \mathbf{C}_d\dot{\mathbf{A}} + \mathbf{K}\mathbf{A} = \mathbf{\Gamma}\mathbf{u} \quad (4.1)$$

where  $\mathbf{M}$ ,  $\mathbf{C}_d$  and  $\mathbf{K}$  are respectively the mass, damping and stiffness matrices,  $\mathbf{\Gamma}$  is the control-action matrix, while  $\mathbf{A}$  and  $\mathbf{u}$  are respectively the global degrees of freedom and the actuators input.

#### Local Degrees of Freedom

The element displacement vector is:

$$\mathbf{a}^e = [u_1 \ v_1 \ w_1 \ \vartheta_{x_1} \ \vartheta_{y_1} \ \vartheta_{z_1} \ u_2 \ v_2 \ w_2 \ \vartheta_{x_2} \ \vartheta_{y_2} \ \vartheta_{z_2}]^T \quad (4.2)$$

where 1 and 2 indexes are referred to the element nodes at the extremity, while  $u$ ,  $v$  and  $w$  stand for the translation displacements, and  $\vartheta_x$ ,  $\vartheta_y$  and  $\vartheta_z$  represent the three rotational displacement. Thus, the element stiffness and the mass matrices are  $12 \times 12$  matrices. The components of the stiffness matrix are listed as follows,

$$\mathbf{k}^e = \begin{bmatrix} \frac{EA}{2a} & 0 & 0 & 0 & 0 & 0 & -\frac{EA}{2a} & 0 & 0 & 0 & 0 & 0 \\ & \frac{3EI_{z_L}}{2a^3} & 0 & 0 & 0 & \frac{3EI_{z_L}}{2a^2} & 0 & -\frac{3EI_{z_L}}{2a^3} & 0 & 0 & 0 & \frac{3EI_{z_L}}{2a^2} \\ & & \frac{3EI_{y_L}}{2a^3} & 0 & -\frac{3EI_{y_L}}{2a^2} & 0 & 0 & 0 & -\frac{3EI_{y_L}}{2a^3} & 0 & -\frac{3EI_{y_L}}{2a^2} & 0 \\ & & & \frac{GJ}{2a} & 0 & 0 & 0 & 0 & 0 & -\frac{GJ}{2a} & 0 & 0 \\ & & & & \frac{2EI_{y_L}}{a} & 0 & 0 & 0 & \frac{3EI_{y_L}}{2a^2} & 0 & \frac{EI_{y_L}}{a} & 0 \\ & & & & & \frac{2EI_{z_L}}{a} & 0 & -\frac{3EI_{z_L}}{2a^2} & 0 & 0 & 0 & \frac{EI_{z_L}}{a} \\ & & & & & & \frac{EA}{2a} & 0 & 0 & 0 & 0 & 0 \\ & & & & & & & \frac{3EI_{z_L}}{2a^3} & 0 & 0 & 0 & -\frac{3EI_{z_L}}{2a^2} \\ & & & & & & & & \frac{3EI_{y_L}}{2a^3} & 0 & \frac{3EI_{y_L}}{2a^2} & 0 \\ & & & & & & & & & \frac{GJ}{2a} & 0 & 0 \\ & & & & & & & & & & \frac{2EI_{y_L}}{a} & 0 \\ & & & & & & & & & & & \frac{2EI_{z_L}}{a} \end{bmatrix} \quad (4.3)$$

where  $I_{y_L}$  and  $I_{z_L}$  are the second moment of area of the element cross-sections with respect to the  $y_L$  and  $z_L$  axes, respectively.

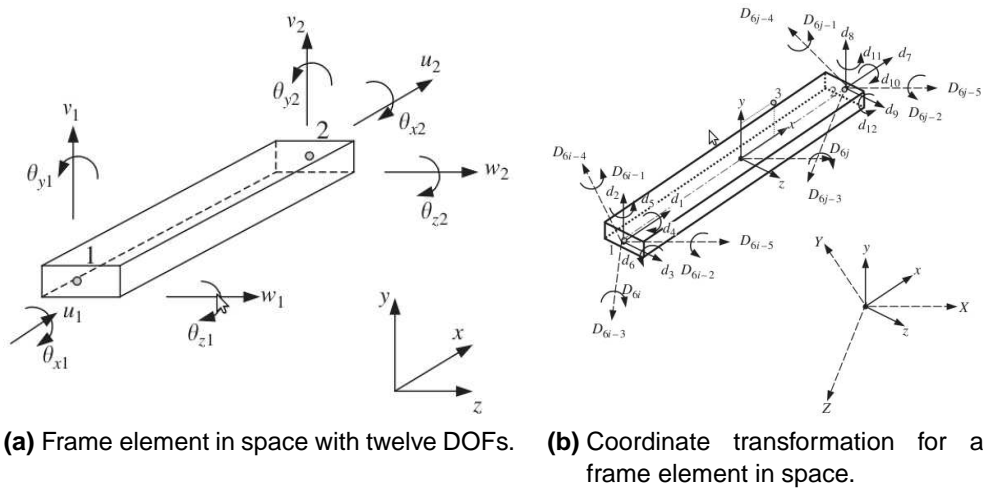


Figure 4.2: Frame element in local and global coordinates

The element mass matrix is:

$$\mathbf{m}^e = \frac{\rho A a}{105} \begin{bmatrix} 70 & 0 & 0 & 0 & 0 & 0 & 35 & 0 & 0 & 0 & 0 & 0 \\ & 78 & 0 & 0 & 0 & 22a & 0 & 27 & 0 & 0 & 0 & -13a \\ & & 78 & 0 & -22a & 0 & 0 & 0 & 27 & 0 & 13a & 0 \\ & & & 70r_x^2 & 0 & 0 & 0 & 0 & 0 & -35r_x^2 & 0 & 0 \\ & & & & 8a^2 & 0 & 0 & 0 & -13a & 0 & -6a^2 & 0 \\ & & & & & 8a^2 & 0 & 13a & 0 & 0 & 0 & -6a^2 \\ & & & & & & 70 & 0 & 0 & 0 & 0 & 0 \\ & & & & & & & 78 & 0 & 0 & 0 & -22a \\ & & & & & & & & 78 & 0 & 22a & 0 \\ & & & & & & & & & 70r_x^2 & 0 & 0 \\ & & & & & & & & & & 8a^2 & 0 \\ & & & & & & & & & & & 8a^2 \end{bmatrix} \quad (4.4)$$

where

$$r_x^2 = \frac{I_{xL}}{A} \quad (4.5)$$

in which  $I_x$  is the second moment of area of the element cross-section with respect to the  $x_L$  axis.

### 4.1.5 Global Degrees of Freedom

The element matrices should be rotated into the global coordinate system in order to express the dynamic equations involving the global displacement vector  $\mathbf{A}$ . Considering Figure 4.2, Assuming that the local nodes 1 and 2 of the element correspond to global nodes  $i$  and  $j$  in the global displacement vector, respectively. As stated by (4.2), the displacement of a node in the SL frame has three translational

components in the  $x_L$ ,  $y_L$  and  $z_L$  directions, and three rotational components with respect to the  $x$ ,  $y$  and  $z$  axes for a total of 6 degrees of freedom.

The six displacements of the  $i$ th node in the SG frame are listed in the  $\mathbf{A}$  vector in the same block  $\mathbf{A}_i^e$ , from the position  $6i - 5$  to the position  $6i$ . In particular the first three components  $A_{6i-5}$ ,  $A_{6i-4}$  and  $A_{6i-3}$  correspond respectively to the translation of the  $i$ th node along the  $X_S$ ,  $Y_S$  and  $Z_S$  axes, while  $A_{6i-2}$ ,  $A_{6i-1}$  and  $A_{6i}$  are the three rotational displacements around the  $X_S$ ,  $Y_S$  and  $Z_S$  axes (Figure 4.2b). The same convention is applied to the node  $j$  in order to identified an equivalent block  $\mathbf{A}_j^e$ . The degrees of freedom of an element  $e$  is expressed as:

$$\mathbf{A}^e = \begin{Bmatrix} \mathbf{A}_i^e \\ \mathbf{A}_j^e \end{Bmatrix} \quad (4.6)$$

Thus  $\mathbf{A}^e$  results to be:

$$\mathbf{A}^e = [A_{6i-5} \ A_{6i-4} \ A_{6i-3} \ A_{6i-2} \ A_{6i-1} \ A_{6i} \ A_{6j-5} \ A_{6j-4} \ A_{6j-3} \ A_{6j-2} \ A_{6j-1} \ A_{6j}]^T \quad (4.7)$$

The coordinate transformation gives the relationship between  $\mathbf{a}^e$  and  $\mathbf{A}^e$ :

$$\mathbf{a}^e = \mathbf{T}^e \mathbf{A}^e \quad (4.8)$$

where  $\mathbf{T}^e$  is the transformation matrix for the element  $e$  given by

$$\mathbf{T} = \begin{bmatrix} \mathbf{T}_3^e & \mathbf{0} & \mathbf{0} & \mathbf{0} \\ \mathbf{0} & \mathbf{T}_3^e & \mathbf{0} & \mathbf{0} \\ \mathbf{0} & \mathbf{0} & \mathbf{T}_3^e & \mathbf{0} \\ \mathbf{0} & \mathbf{0} & \mathbf{0} & \mathbf{T}_3^e \end{bmatrix} \quad (4.9)$$

in which  $\mathbf{T}_3^e$  is the direction cosines matrix between the SL and the SG reference frames for the element  $e$ .

Using the transformation matrix  $\mathbf{T}^e$ , the mass and stiffness matrices of the element  $e$  in the global coordinate system are:

$$\mathbf{K}^e = \mathbf{T}^{eT} \mathbf{k}^e \mathbf{T}^e \quad (4.10)$$

$$\mathbf{M}^e = \mathbf{T}^{eT} \mathbf{m}^e \mathbf{T}^e \quad (4.11)$$

### Assembling Procedure

Once that the mass and stiffness matrices of the singular element have been constructed, the global matrices must be assembled. An ordinary procedure is to express the global matrices as the sum of the contribution coming from each element:

$$\mathbf{K} = \sum_e \tilde{\mathbf{K}}^e \quad \mathbf{M} = \sum_e \tilde{\mathbf{M}}^e \quad (4.12)$$

where  $\tilde{\mathbf{K}}^e$  and  $\tilde{\mathbf{M}}^e$  are the expanded matrices of the element  $e$ . They can be calculated as:

$$\tilde{\mathbf{K}}^e = \mathbf{H}^{eT} \mathbf{K}^e \mathbf{H}^e \quad \tilde{\mathbf{M}}^e = \mathbf{H}^{eT} \mathbf{M}^e \mathbf{H}^e \quad (4.13)$$

where  $\mathbf{H}^e$  is the extraction matrix which relates the degrees of freedom of the element  $e$  to the vector of the global degrees of freedom  $\mathbf{A}$ :

$$\mathbf{A}^e = \mathbf{H}^e \mathbf{A} \quad (4.14)$$

This procedure results to the global mass and stiffness matrices of dimension  $6n_{\text{nod}} \times 6n_{\text{nod}}$ . Considering the large dimension of the system, the procedure described before is not convenient in terms of computational time. Indeed a large number of zero values should be memorized at each time.

Another procedure has been investigated which involves the use of a pointing vector  $\mathbf{I}^e$  for each element  $e$ . The position of each parameter in the  $\mathbf{I}^e$  vector indicates the degree of freedom in the  $\mathbf{A}^e$ , while the value of each parameter stand for the relative position in the  $\mathbf{A}$  vector. Then, the global matrices  $\mathbf{K}$  and  $\mathbf{M}$  are gradually populated by adding up the contribute of every element [coo].

### Damping Matrix

The definition of a plausible damping matrix  $\mathbf{C}_d$  has been investigated. A diagonal modal damping matrix is assumed in accordance with the experimental results, which usually reveal uncoupled damping on each mode. As a consequence, if Equation 4.1 are written using the modal transformation  $\mathbf{A} = \mathbf{U}q$ :

$$\mathbf{U}^T \mathbf{M} \mathbf{U} \ddot{\mathbf{q}} + \mathbf{U}^T \mathbf{C}_d \mathbf{U} \dot{\mathbf{q}} + \mathbf{U}^T \mathbf{K} \mathbf{U} \mathbf{q} = \mathbf{U}^T \mathbf{F} \mathbf{u} \quad (4.15)$$

it is reasonable to assume that  $\mathbf{C}_d$  should has the same property of orthogonality as the mass and stiffness matrices with respect to the modal matrix  $\mathbf{U}$ . A model often used to describe the structural damping considers the damping matrix as a linear combination of the mass and stiffness matrices:

$$\mathbf{C}_d = \alpha_M \mathbf{M} + \alpha_K \mathbf{K} \quad (4.16)$$

The proportionality with respect to the stiffness matrix can be refereable to a viscous-elastic constitutive law of the material, while the proportionality to the mass matrix is more complex and need further studies. For this reason, since a low damping is preferable, in order to prove the effectiveness of a vibration suppression system, the proportionality to the mass matrix has been neglected, while  $\alpha_K$  has been taken equal to 0.005, considering that a value between 0.1 and 0.01 is usually assumed for a bolted structure.

### Dynamic Problem

The modal analysis is useful to easily understand the behaviour of the structure in terms of frequency response. First of all it is necessary to evaluate the first modal frequencies of the structure in order to predict an eventual strong interaction with the orbit and attitude low-bandwidth control. Secondly the modal analysis may be employed to simplify the behaviour of the structure by considering a proper number of flexible modes (see Chapter 5). In the end, the results coming from the modal analysis can be easily compared with a structural-analysis program available on the market.

The dynamic problem is stated by the following equation system

$$\mathbf{M}\ddot{\mathbf{a}} + \mathbf{K}\mathbf{a} = \mathbf{0} \quad (4.17)$$

Assuming the harmonic solution  $\mathbf{a} = \Phi e^{i\omega t}$ , the problem can be rewritten as

$$(\mathbf{K} - \omega^2\mathbf{M}) \Phi e^{i\omega t} = \mathbf{0} \quad (4.18)$$

The non trivial solution is found by imposing

$$\det(\mathbf{K} - \omega^2\mathbf{M}) = 0 \quad (4.19)$$

which leads to the determination of the modal frequencies from the eigenvalues  $\omega$ . The associated eigenvectors  $\Phi_i$  are the modal shapes of the structure.

The computation of the modal frequency and their eigenvector is accomplished in MATLAB<sup>®</sup> by means of the `eigs` function which calculates the first  $k$  eigenvalues, where  $k$  is specified by the user.

### 4.1.6 Structural Model Comparison

Here after, the results obtained by using the implemented algorithm are compared with the results computed by NASTRAN on the same structure already defined in Section 4.1.3. Table 4.3 shows the first eight modal frequencies with the associated modes depicted in the Figures from 4.3 to 4.10. As it is evident, some modes at a similar modal frequency are switched. However, Table 4.3 shows that the error in terms of frequencies is not relevant, and that the modal behaviour of the structure can be considered to be sufficiently known.

**Table 4.3:** Comparison of the modal frequencies.

	NASTRAN	MATLAB	Error [%]
Freq. 1	0.0018038	0.0018068	0.16631
Freq. 2	0.0029589	0.0029660	0.23995
Freq. 3	0.0029913	0.0029991	0.26076
Freq. 4	0.0047973	0.0048172	0.41482
Freq. 5	0.0048123	0.0048203	0.16624
Freq. 6	0.0079923	0.0080274	0.43917
Freq. 7	0.0080272	0.0080456	0.22922
Freq. 8	0.0084396	0.0084718	0.38153

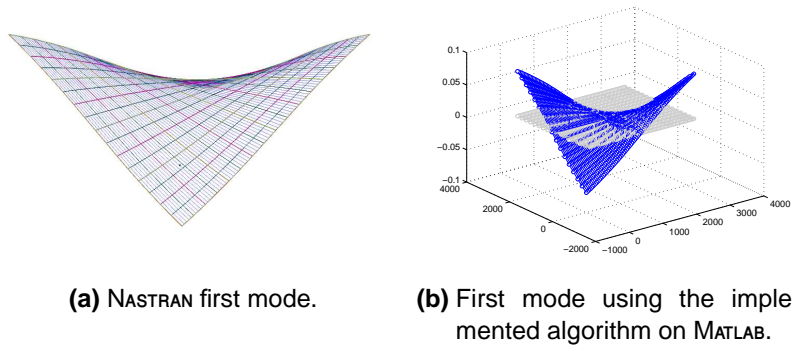


**Figure 4.3:** Comparison of the first modal mode

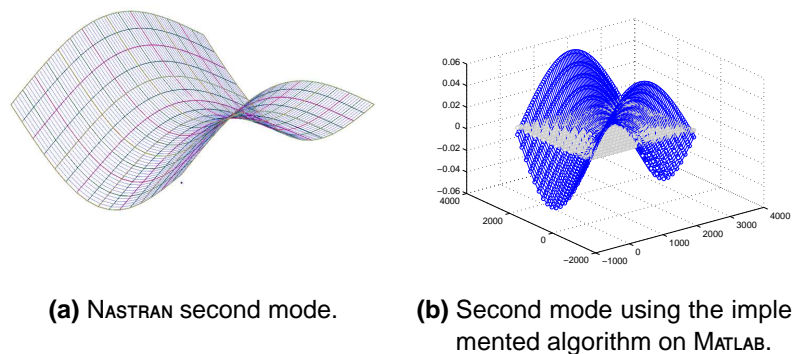
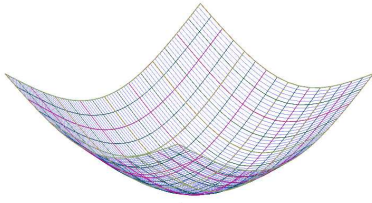
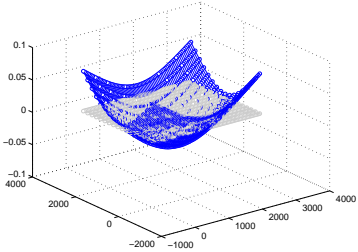


**Figure 4.4:** Comparison of the second modal mode

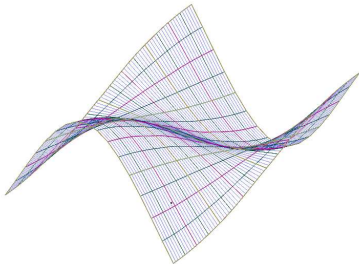


(a) NASTRAN third mode.

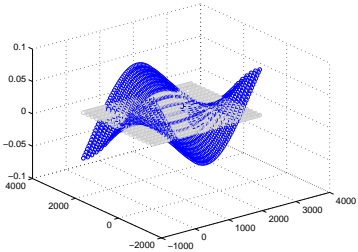


(b) Third mode using the implemented algorithm on MATLAB.

**Figure 4.5:** Comparison of the third modal mode

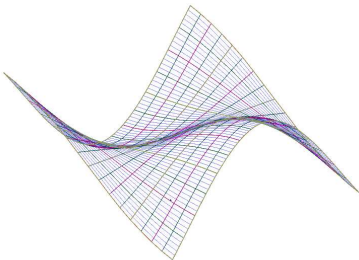


(a) NASTRAN fourth mode.

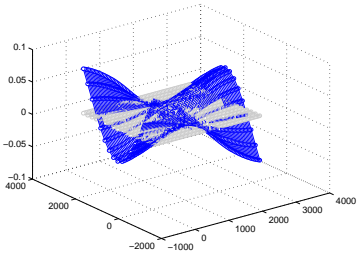


(b) Fourth mode using the implemented algorithm on MATLAB.

**Figure 4.6:** Comparison of the fourth modal mode

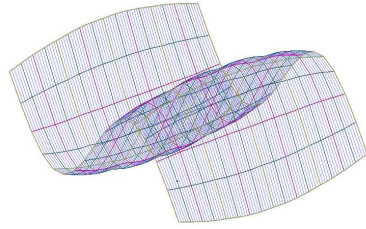


(a) NASTRAN fifth mode.

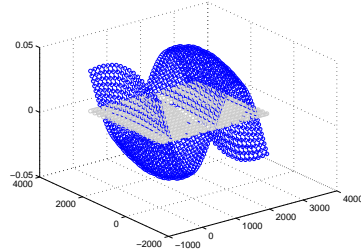


(b) Fifth mode using the implemented algorithm on MATLAB.

**Figure 4.7:** Comparison of the fifth modal mode

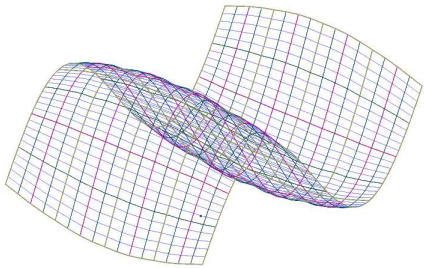


(a) NASTRAN sixth mode.

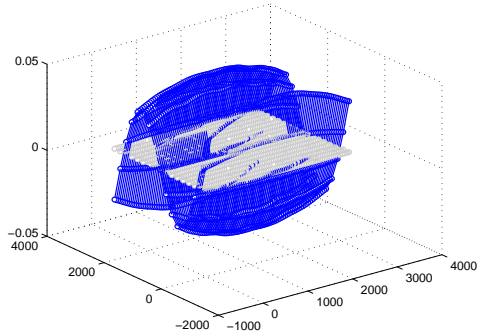


(b) Sixth mode using the implemented algorithm on MATLAB.

**Figure 4.8:** Comparison of the sixth modal mode

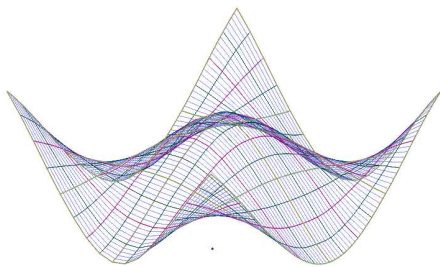


(a) NASTRAN seventh mode.

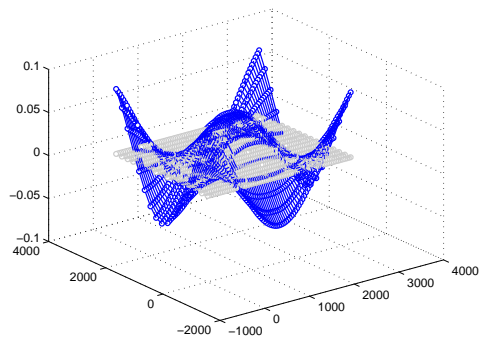


(b) Seventh mode using the implemented algorithm on MATLAB.

**Figure 4.9:** Comparison of the seventh modal mode



(a) NASTRAN eighth mode.



(b) Eighth mode using the implemented algorithm on MATLAB.

**Figure 4.10:** Comparison of the eighth modal mode

## 4.2 State-Space Realization

The dynamic problem defined by Equation (4.1) can be transformed in the state space defining the state vector  $\mathbf{x} = [\mathbf{A} \dot{\mathbf{A}}]^T$ . In the previous expression  $\mathbf{\Gamma}\mathbf{u}$  is the control force vector.

The state space realization can be written as

$$\dot{\mathbf{x}} = \mathbf{A}\mathbf{x} + \mathbf{B}\mathbf{u} \quad (4.20)$$

in which

$$\mathbf{A} = \begin{bmatrix} \mathbf{0} & \mathbf{I} \\ -\tilde{\mathbf{M}}^{-1}\tilde{\mathbf{K}} & -\tilde{\mathbf{M}}^{-1}\tilde{\mathbf{C}}_d \end{bmatrix} \quad \mathbf{B} = \begin{bmatrix} \mathbf{0} \\ -\tilde{\mathbf{M}}^{-1}\tilde{\mathbf{\Gamma}} \end{bmatrix} \quad (4.21)$$

Considering a colocated control system the equation for the sensors measures is

$$\mathbf{y} = \mathbf{C}\mathbf{x} \quad (4.22)$$

where

$$\mathbf{C} = \begin{bmatrix} \tilde{\mathbf{\Gamma}}^T & \mathbf{0} \\ \mathbf{0} & \tilde{\mathbf{\Gamma}}^T \end{bmatrix} \quad (4.23)$$

In the previous expressions  $\tilde{\mathbf{M}}$ ,  $\tilde{\mathbf{K}}$ ,  $\tilde{\mathbf{C}}_d$  and  $\tilde{\mathbf{\Gamma}}$  are the projection of  $\mathbf{M}$ ,  $\mathbf{K}$ ,  $\mathbf{C}_d$  and  $\mathbf{\Gamma}$  onto the space of the flexible modes.

$$\tilde{\mathbf{M}} = \mathbf{\Phi}^T \mathbf{M} \mathbf{\Phi} \quad (4.24a)$$

$$\tilde{\mathbf{C}}_d = \mathbf{\Phi}^T \mathbf{C}_d \mathbf{\Phi} \quad (4.24b)$$

$$\tilde{\mathbf{K}} = \mathbf{\Phi}^T \mathbf{K} \mathbf{\Phi} \quad (4.24c)$$

$$\tilde{\mathbf{\Gamma}} = \mathbf{\Phi}^T \mathbf{\Gamma} \quad (4.24d)$$

in which  $\mathbf{\Phi}$  is the modal matrix where only the flexible modes of the structure are retained.

# Chapter 5

## Model reduction

Numerical simulation of dynamical systems, such as FEM, usually results in complex high-order dynamic models. It is often desirable, e.g. for control design issues, to approximate these models by simpler models with reduced order. In this process it is important to design the reduced model so as to capture the important properties of the original high-order model. Until relatively recently model reduction was often based on physical intuition, that usually means, for mechanical engineers, removing high frequency vibration modes.

In particular, in this chapter it is firstly presented the classical modal truncation, then the necessity of satisfactory approximation of the model behaviour at low frequency leads to investigate the singular perturbation approximation method. A slightly different technique is based on matching some important properties of the system, i.e. the frequency and power moments. Finally the promising family of balanced reductions is described as a possible effective mean of reducing the order of a dynamical model. In the last section of the chapter it is performed the order reduction of the structural model of the satellite employing the introduced methods. Since the presented model reduction techniques lean on some basic properties regarding the linear systems behaviour, Appendix B gives a brief theoretical background on the significant properties.

### 5.1 Preliminary Concepts

Given a dynamic system  $\mathcal{S}$  of usually high order  $n$ , a model reduction is a procedure that yields some approximate model  $\mathcal{S}_r$  of order  $n_r < n$  and such that the following properties, if possible, are satisfied [ASG]:

- The approximation error is small, and there exists an error bound.
- System properties stability is preserved.

- The procedure is computationally stable and efficient.

Let  $\mathcal{S}$  be a LTI model described by the set of equations (4.20) and (4.22),

$$\dot{x} = Ax + Bu \quad (5.1a)$$

$$y = Cx + Du \quad (5.1b)$$

The reduced order model  $\mathcal{S}_r$  to be determined has the same structure as  $\mathcal{S}$ , that is, a linear and time-invariant model described by

$$\dot{x}_r = A_r x_r + B_r u \quad (5.2a)$$

$$y_r = C_r x_r + D_r u \quad (5.2b)$$

where  $x_r$  is a reduced order state and  $y_r$  is the output of the reduced order state.

## 5.2 Model Reduction by Truncation

Dealing with state-space systems, truncation of the state vector is the natural choice for obtaining a reduced order model. In this section several reduction techniques are evaluated where truncation of some states are able to partially preserve selected properties of the original system.

The basic idea behind all the considered techniques is to transform the state vector into a new set of coordinates and then truncate the new state obtained with the transformation. The procedure can be summarized as follow

**Algorithm 1.** Given a LTI system  $\mathcal{S}$  written as in (5.1):

1. A preferred realization can be obtained via the similarity transformation  $T = [T_1 \ T_2]$ .

$$x = [T_1 \ T_2] \begin{Bmatrix} x'_1 \\ x'_2 \end{Bmatrix} \quad \text{and} \quad \begin{Bmatrix} x'_1 \\ x'_2 \end{Bmatrix} = \begin{bmatrix} R_1^T \\ R_2^T \end{bmatrix} x \quad (5.3)$$

where  $T_1 R_1^T + T_2 R_2^T = I_n$ .

2. This operation transforms the realization of the original system as

$$A \rightarrow \mathbf{A}' = \begin{bmatrix} R_1^T A T_1 & R_1^T A T_2 \\ R_2^T A T_1 & R_2^T A T_2 \end{bmatrix}, \quad B \rightarrow \mathbf{B}' = \begin{bmatrix} R_1^T B \\ R_2^T B \end{bmatrix} \quad C \rightarrow \mathbf{C}' = [C T_1 \ C T_2] \quad (5.4)$$

3. A reduced model (5.2) is then obtained by truncating the state vector so as to preserve only the state  $x_r = x'_1$ .

$$A_r = R_1^T A T_1, \quad B_r = R_1^T B, \quad C_r = C T_1, \quad D_r = D \quad (5.5)$$

### 5.2.1 Minimal Transfer Equivalent Realization

In Section B.1 it has been shown that different realizations can have the same transfer function. This leads to the following definition.

**Definition 1.** Two distinct state-space realizations of a linear time-invariant system are said to be transfer equivalent if they have the same transfer function.

In the context of model reduction, given a state-space realization  $(A, B, C, D)$  of order  $n$ , the realization is minimal in the sense that there exists no other transfer equivalent realization  $(A_r, B_r, C_r, D_r)$  of order  $n_r$  smaller than  $n$ . The following theorem, which is due to Kalman, gives a characterization of minimal state space realizations [DS00].

**Theorem 1.** *The state-space realization  $(A, B, C, D)$  is minimal if, and only if, it is controllable and observable.*

An immediate implication is that if a given realization is not minimal, one should be able to obtain a transfer equivalent realization with reduced order. A transfer function with minimal degree is obtained when  $(A_r, B_r, C_r, D_r)$  is controllable and observable. A constructive procedure to compute such a minimal realization is based on the calculation of the controllable and observable subspaces. The following algorithm allows to build a minimal transfer equivalent realization in two steps. In the first step, it extracts the controllable subspace of  $(A, B, C, D)$  then, in the second step, it obtains the observable subspace of the controllable system built in step one. The resulting system is controllable and observable.

**Algorithm 2.** Given the state-space realization  $(A, B, C, D)$  of order  $n$ :

1. Calculate the singular value decomposition

$$\mathcal{C} = [U_{c_1} \quad U_{c_2}] \begin{bmatrix} \Sigma_c & 0 \\ 0 & 0 \end{bmatrix} \begin{bmatrix} V_{c_1}^T \\ V_{c_2}^T \end{bmatrix} = U_{c_1} \Sigma_c V_{c_1}^T \quad (5.6)$$

Define  $T_c := U_{c_1} \Sigma_c^{1/2}$ .

2. Calculate the singular value decomposition

$$\mathcal{O}T_c = [U_{co_1} \quad U_{co_2}] \begin{bmatrix} \Sigma_{co} & 0 \\ 0 & 0 \end{bmatrix} \begin{bmatrix} V_{co_1}^T \\ V_{co_2}^T \end{bmatrix} = U_{co_1} \Sigma_{co} V_{co_1}^T \quad (5.7)$$

3. Compute the matrices

$$T_1 = U_{c_1} \Sigma_c^{1/2} V_{co_1} \Sigma_{co}^{-1/2}, \quad R_1 = U_{c_1} \Sigma_c^{-1/2} V_{co_1} \Sigma_{co}^{1/2} \quad (5.8)$$


---

The state-space realization of order  $n_m$ , built using (5.4) and (5.5), is a minimal transfer equivalent realization of  $(A, B, C, D)$ .

Caution must be exerted when these results are to be followed by the design of a control law. It should be said that the deletion of unobservable states is always desirable (given that the output includes all variables of interest), but it is not always desirable to delete uncontrollable states.

Reducing the model to a minimal degree realization is necessary in order to implement model reduction techniques beyond the minimal degree.

### 5.2.2 Modal Truncation

Truncation methods of model reduction seek to remove unimportant states from state-space models. As mentioned before, an ordinary approach, known as modal truncation, seeks to remove those states that correspond to fast modes, i.e. high frequency modes.

The main advantage of modal truncation, beyond its inherent simplicity, is that the poles of the reduced order system are a subset of the poles of the full order system. This means that the most important frequencies of the dynamical system are retained in the reduced model. In the following algorithm, the simple implementation of modal truncation is outlined.

**Algorithm 3.** Given the minimal state-space realization  $(A, B, C, D)$  of order  $n$ :

1. Compute the solution to the eigenvalue problem associated with matrix  $A$  and determine the right eigenvectors matrix,

$$\mathbf{\Phi} = [\mathbf{\Phi}_1 \quad \dots \quad \mathbf{\Phi}_n] \quad (5.9)$$

2. The similarity transformation (5.3) with  $\mathbf{T} = \mathbf{\Phi}$  and  $\mathbf{R} = \mathbf{\Phi}^{-T}$  puts matrix  $\mathbf{A}$  into a diagonal form (known as Jordan form) and state  $\mathbf{x}$  into modal coordinates<sup>1</sup>. Wanting to discard those modes with the highest natural frequencies, order the eigenvalues so that  $|\lambda_i|$  is non-decreasing with increasing  $i$ .

3. Divide the state vector  $\mathbf{x}'$  into components to be retained and components to be discarded

$$\mathbf{x}' = \begin{Bmatrix} x'_1 \\ x'_2 \end{Bmatrix} \quad (5.10)$$

in which the  $n_r$ -vector  $\mathbf{x}'_1$  contains the components to be retained and  $\mathbf{x}'_2$  contains those states to be discarded.

---

<sup>1</sup>This is strictly true if  $\mathbf{A}$  has distinct eigenvalues. Although, for multiple eigenvalues, it is possible to transform it into a block diagonal form (see [Kai80]).

4. Partition the matrices  $\mathbf{T}$  and  $\mathbf{R}$  in conformity with  $\mathbf{x}'$

$$\mathbf{T} = [\mathbf{T}_1 \quad \mathbf{T}_2], \quad \mathbf{R} = [\mathbf{R}_1 \quad \mathbf{R}_2] \quad (5.11)$$

5. The reduced model of order  $n_r$  is then obtained using (5.4) and (5.5).

The error incurred in modal truncation depends not only on the  $\lambda_i$ , but also on the size of the residues  $\mathbf{C}_i \mathbf{B}_i$ . If modes labelled  $n_r + 1$  to  $n$  are omitted by truncation to obtain  $\mathbf{G}_r$ , the following holds [GL94],

$$\|\mathbf{G} - \mathbf{G}_r\|_\infty \leq \sum_{i=n_r+1}^n \frac{\|\mathbf{C}_i \mathbf{B}_i\|_2}{|\Re(\lambda_i)|}. \quad (5.12)$$

Another property that surely holds between the transfer function matrices  $\mathbf{G}$  and  $\mathbf{G}_r$ , is

$$\mathbf{G}_r(\infty) = \mathbf{G}(\infty) \quad (5.13)$$

which means that all reduced order models obtained by truncation have perfect matching at infinite frequency.

### 5.2.3 Singular Perturbation Approximation

The steady state error obtained with state-space truncation may be unacceptably large for applications requiring good low-frequency fidelity. In these cases, it is appropriate to use a singular perturbation approximation in which the dynamics associated with the discarded states, i.e. the fast dynamics, is statically recovered in the reduced order model. The following algorithm sum up the procedure used to obtain the reduced model of the LTI system  $\mathcal{S}$ , employing the singular perturbation approximation.

**Algorithm 4.** Given the minimal state-space realization  $(A, B, C, D)$  of order  $n$ :

1. Compute the similarity transformation (5.4) with matrices  $\mathbf{T}$  and  $\mathbf{R}$  calculated as in Algorithm 3
2. Approximate the low-frequency behaviour of the fast dynamics of the system, represented by  $\mathbf{x}'_2$ , by setting  $\dot{\mathbf{x}}'_2 = \mathbf{0}$

$$\mathbf{0} = \mathbf{A}'_{21} \mathbf{x}'_1 + \mathbf{A}'_{22} \mathbf{x}'_2 + \mathbf{B}'_2 \mathbf{u} \quad (5.14)$$

which, provided  $\mathbf{A}'_{22}$  non singular, yields

$$\mathbf{x}'_2 = -\mathbf{A}'_{22}{}^{-1} (\mathbf{A}'_{21} \mathbf{x}'_1 + \mathbf{B}'_2 \mathbf{u}) \quad (5.15)$$

3. Eliminating  $\mathbf{x}'_2$  from the equations associated with  $\mathbf{x}'_1$ , the reduced model of order  $n_r$  can be written as

$$\mathbf{A}_r = \mathbf{A}'_{11} - \mathbf{A}'_{12}\mathbf{A}'_{22}{}^{-1}\mathbf{A}'_{21}, \quad \mathbf{B}_r = \mathbf{B}'_1 - \mathbf{A}'_{12}\mathbf{A}'_{22}{}^{-1}\mathbf{B}'_2 \quad (5.16a)$$

$$\mathbf{C}_r = \mathbf{C}'_1 - \mathbf{C}'_2\mathbf{A}'_{22}{}^{-1}\mathbf{A}'_{21}, \quad \mathbf{D}_r = \mathbf{D}' - \mathbf{C}'_2\mathbf{A}'_{22}{}^{-1}\mathbf{B}'_2 \quad (5.16b)$$

It can be shown that the singular perturbation approach is related to state-space truncation by a bilinear transformation  $s \mapsto 1/s$  (see [GL94]). Hence, this method achieves perfect approximation at steady state,

$$\mathbf{G}_r(0) = \mathbf{G}(0) \quad (5.17)$$

## 5.2.4 Matching Frequency and Power Moments

The following algorithm is able to reduce a minimal realization in such a manner that the reduced model matches a subset of low frequency moments and a subset of high frequency moments

The next lemma shows how to develop reduced order models that match a subset of the high frequency and power moments, that is, the Markov and the covariance parameters.

**Lemma 1.** Given the minimal and asymptotically stable realization  $(A, B, C, 0)$  of order  $n$ , compute the symmetric and positive definite controllability grammian  $W_c$ . Calculate the singular value decomposition

$$W_q = \begin{bmatrix} U_{q1} & U_{q2} \end{bmatrix} \begin{bmatrix} \Sigma_q & 0 \\ 0 & 0 \end{bmatrix} \begin{bmatrix} V_{q1}^T \\ V_{q2}^T \end{bmatrix} = U_{q1}\Sigma_q V_{q1}^T \quad (5.18)$$

where

$$W_q := \begin{bmatrix} C \\ CA \\ \vdots \\ CA^{q-1} \end{bmatrix} \quad (5.19)$$

Then compute the following matrices

$$T_{q1} = W_c V_{q1} (V_{q1}^T W_c V_{q1})^{-1}, \quad R_{q1} = V_{q1} \quad (5.20)$$

The preferred realization of order  $n_r$  defined by

$$\mathbf{A}_r = R_{q1}^T A T_{q1}, \quad \mathbf{B}_r = R_{q1}^T B, \quad \mathbf{C}_r = C T_{q1}, \quad \mathbf{D}_r = D \quad (5.21)$$

is asymptotically stable and matches the first  $q$   $M_i(j\infty)$  and the first  $q$   $R_i(j\infty)$ , where  $i = 0, \dots, q-1$ , of  $(A, B, C, 0)$ . It is worth to notice that the stability of the reduced system comes from the minimality of the original system

Low frequency parameters can be matched by means of the following lemma

**Lemma 2.** Given the minimal and asymptotically stable realization  $(A, B, C, 0)$  of order  $n$  and computed the controllability grammian  $W_c$ , calculate the singular value decomposition

$$W_p = [U_{p1} \quad U_{p2}] \begin{bmatrix} \Sigma_p & 0 \\ 0 & 0 \end{bmatrix} \begin{bmatrix} V_{p1}^T \\ V_{p2}^T \end{bmatrix} = U_{p1} \Sigma_p V_{p1}^T \quad (5.22)$$

in which

$$W_p := \begin{bmatrix} CA^{-1} \\ CA^{-2} \\ \vdots \\ CA^{-p} \end{bmatrix} \quad (5.23)$$

Calculate the matrices

$$T_{p1} = W_c V_{p1} (V_{p1}^T W_c V_{p1})^{-1}, \quad R_{p1} = V_{p1} \quad (5.24)$$

The preferred realization of order  $n_r$  given by

$$A_r = R_{p1}^T A T_{p1}, \quad B_r = R_{p1}^T B, \quad C_r = C T_{p1}, \quad D_r = D \quad (5.25)$$

is asymptotically stable and matches the first  $p$   $M_i(j0)$  and the first  $p$   $R_i(j0)$ , where  $i = 0, \dots, p-1$ , of  $(A, B, C, 0)$ .

Matching the first low frequency moments guarantees that the steady state values of the response of the system are preserved. On the other hand, matching the high frequency moments guarantees that the time moments of the impulse response are matched.

Combining the results expressed by Lemma 1 and Lemma 2, it is possible to develop an algorithm that can be employed to simultaneously match a set of high and low frequency moments.

**Algorithm 5.** Given the minimal state-space realization  $(A, B, C, 0)$  of order  $n$ :

1. Calculate the singular value decomposition

$$\begin{bmatrix} W_q \\ W_p \end{bmatrix} = [U_1 \quad U_2] \begin{bmatrix} \Sigma & 0 \\ 0 & 0 \end{bmatrix} \begin{bmatrix} V_1^T \\ V_2^T \end{bmatrix} = U_1 \Sigma V_1^T \quad (5.26)$$

where matrices  $W_q$  and  $W_p$  are defined by 5.19 and 5.22

2. Define the matrices

$$T_1 = W_c V_1 (V_1^T W_c V_1)^{-1}, \quad R_1 = V_1 \quad (5.27)$$


---

3. Produce the following state-space realization of order  $n_r$

$$A_r = R_1^T A T_1, \quad B_r = R_1^T B, \quad C_r = C T_1, \quad D_r = D \quad (5.28)$$

The latter computed model matches the first  $p$  low frequency moments and the first  $q$  high frequency moments, as stated by Lemma 1 and Lemma 2. It is interesting to notice that the projections generate reduced order models that are not guaranteed to approximate the original system according to any system norm.

### 5.2.5 Balanced Truncation

Balanced truncation is an interesting technique for model reduction because of its good absolute-error truncation properties. It requires a state truncation of a system which is represented in a preferred set of coordinates, known as balanced coordinates.

**Definition 2.** The asymptotically stable and time-invariant state-space realization  $(A, B, C, D)$  of order  $n$ , is said to be in balanced coordinates if the controllability and observability grammians,  $W_c$  and  $W_o$ , are equal and diagonal. Hence, the following hold

$$AW + WA^T + BB^T = 0 \quad (5.29a)$$

$$A^T W + WA + C^T C = 0 \quad (5.29b)$$

where

$$W_c = W_o = W = \begin{bmatrix} \sigma_1 I_{r_1} & 0 & 0 \\ 0 & \ddots & 0 \\ 0 & 0 & \sigma_m I_{r_m} \end{bmatrix}, \quad \sigma_i \neq \sigma_j \text{ and } \sigma_i > 0 \quad \forall i \quad (5.30)$$

in which  $n = r_1 + \dots + r_m$ , each  $r_i$  being the multiplicity of the correspondent  $\sigma_i$ . The balanced realization is said to be an ordered balanced realization if, in addition,  $\sigma_1 > \dots > \sigma_m > 0$ .

The following theorem, concerned with the existence and uniqueness of balanced realization, can be proved.

**Theorem 2.** *A given realization  $(A, B, C, D)$  admits a balanced representation if and only if it is minimal and asymptotically stable.*

**Algorithm 6.** Given the minimal and asymptotically stable system  $(A, B, C, D)$  of order  $n$ :

1. Compute the controllability grammian  $W_c$  and factorize it such that

$$W_c = F^T F \quad (5.31)$$

2. Calculate the observability grammian  $W_o$  and the singular value decomposition

$$FW_o F^T = [U_1 \ U_2] \begin{bmatrix} \Sigma_1^2 & 0 \\ 0 & \Sigma_2^2 \end{bmatrix} \begin{bmatrix} U_1^T \\ U_2^T \end{bmatrix} \quad (5.32)$$

where  $\Sigma = \text{diag}(\sigma_1 I_{r_1}, \dots, \sigma_m I_{r_m})$  and the  $\sigma_i$  are the Hankel singular values.

3. The following matrices

$$T_1 = F^T U_1 \Sigma_1^{-1/2}, \quad R_1 = F^{-1} U_1 \Sigma_1^{1/2} \quad (5.33)$$

produce the reduced model of order  $n_r$  obtained by truncation of the original system transformed in balanced coordinates.

$$A_r = R_1^T A T_1, \quad B_r = R_1^T B, \quad C_r = C T_1, \quad D_r = D \quad (5.34)$$

In practice, this approximation method provides very efficient and good approximate models. It eliminates the poorly reachable and poorly observable states from a state space model.

As mentioned before, balanced truncation is attractive also due to its good truncation error properties. In particular the following relation can be proved to provide an upper bound for the infinity norm of the model reduction error (see [dVS87])

$$\|G - G_r\|_\infty \leq 2 \sum_{i=n_r+1}^n \sigma_i. \quad (5.35)$$

## 5.3 Application of the Reduction Algorithms

In control theory, eigenvalues define a system stability, whereas Hankel singular values define the energy of each state in the system [BB94]. Keeping larger energy states of a system preserves most of its characteristics in terms of stability, frequency, and time responses. In virtue of this consideration, the rationale according to which the order of the reduced system can be selected is analysing the rate of decay of the the Hankel singular values of the structural model developed in Chapter 4. Referring to a system in which a number of collocated sensors and actuators are employed as in Figure 5.1, the associated minimal dynamical system ( $\mathbf{A}, \mathbf{B}, \mathbf{C}, \mathbf{D}$ ) of order 56 is then considered. In Figure 5.2 are shown the determined

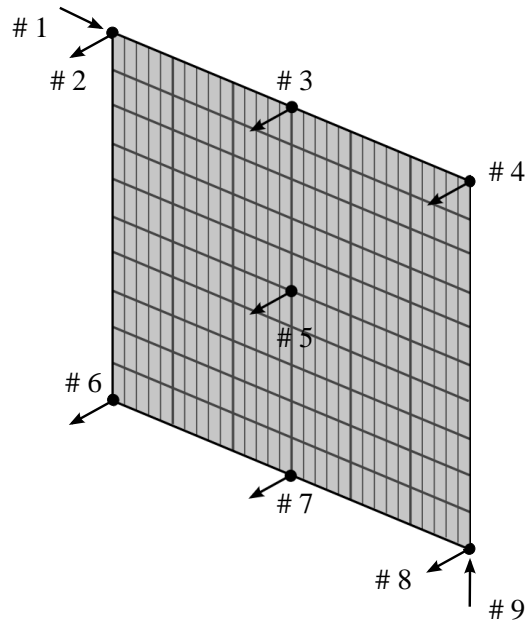


**Figure 5.1:** Actuators pattern employed in generating the minimal structural model of order 56.

Hankel singular values for this system in which the first thirty modes have been computed, resulting to be a sixth order system. Two huge drops in their magnitude can be noticed between the eighth and the ninth singular value and between the twelfth and the thirteenth. Consequently, in Figures 5.4 - 5.7 are depicted the Bode plots of the reduced systems obtained using the aforementioned algorithms in comparison with those of the full-order system. As an illustrative example, the response from input 4 to output 4 is showed. Although this choice is to be considered not a limiting one for the interpretation of the results. It is clear that, when employing the matching moments technique, one cannot directly select the order of the reduced model. It is instead necessary to choose the number of the moments at low and high frequency that are desired to be matched. The order of the reduce system is then computed by the implemented routine itself. As concern the modal truncation, the singular perturbation approximation and the balanced reduction, that is for those techniques in which the order of the reduced system can be explicitly imposed, the twelfth order systems, as expected, better approximate the full order system behaviour. A little increasing in the dimensions of the system (eighth to twelfth order) allows to achieve a better behaviour at very low frequencies and permits a good match of the peaks of the Bode magnitude plot in the frequency band between  $10^{-3}$  and  $10^{-2}$  Hz, this being the frequency band of interest for the first modes of the structure. On the other hand, when the matching

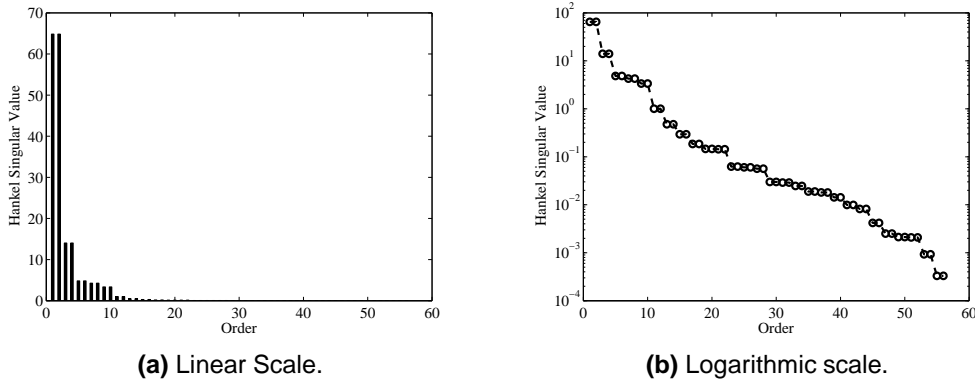


**Figure 5.2:** Hankel Singular Values for the considered full dynamical system of the 56<sup>th</sup> order.

moments method is used, requiring to match just the first low frequency moments leads to a reduced system of the 18<sup>th</sup> order, whereas matching the first two low frequency moments entails a reduced-order model of the 36<sup>th</sup> order. Hence, this technique does not appear to be effective for the problem of interest in the present work.

Among the remaining methods, the singular perturbation approximation provides the best approximation of the full order system at very low frequency, as anticipated by the given theoretical considerations in Section 5.2.3, allows a perfect match at the lowest frequencies. Nevertheless, since the resulting reduced system is not strictly proper, it shows a non-zero feed-through and a greatly different high-frequency response.

Balanced reductions have the main advantage of eliminating the less controllable and observable states and, at the same time, provide a valid global frequency behaviour of the reduced system, very much comparable to that obtained by modal truncation.

In Table 5.1 are reported the approximation errors, measured as  $\|\mathbf{G} - \mathbf{G}_r\|_\infty$ , made by the different reduction methods described. It can be noticed that, since the matching moments algorithm does not provide any bound to that error, it turns out to be an order of magnitude greater than the errors resulting from the other reduction methods, and even worse if the 36<sup>th</sup> order is to be used. Concerning the other techniques, the infinity norm of the error is essentially the same, regardless the order and the method used, apart from the 12<sup>th</sup> order reduced system obtained by balancing the state, which shows a roughly halved error.

Drawing on the previous considerations, a reduced model of order twelve is chosen. Besides, for the next developments regarding the design of a vibration suppression system, it will be useful to interpret the results focusing onto the structural modes behaviour. Hence, for clarity's sake, the choice has fallen onto the

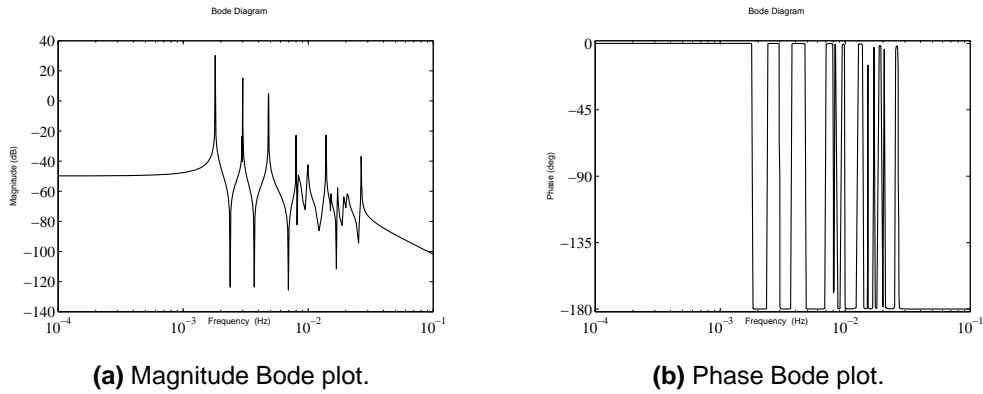


**Figure 5.3:** Bode plots of the full order model, 56<sup>th</sup> order. From input 4 to output 4.

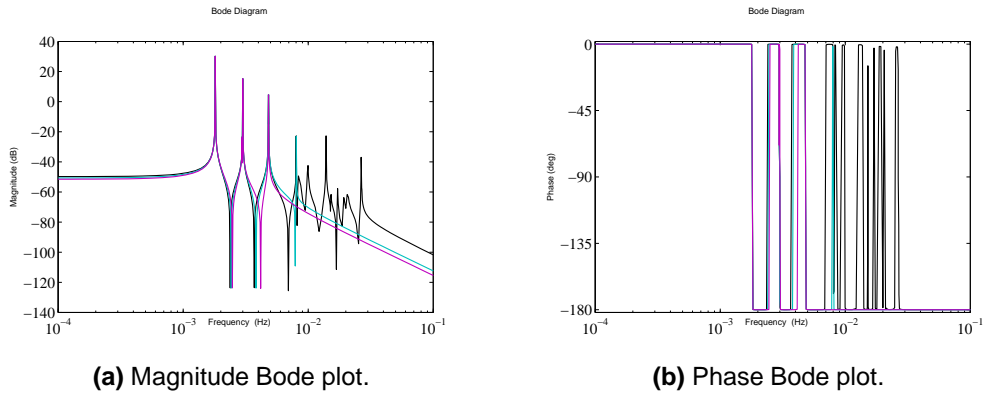


**Figure 5.4:** Bode plots of the reduced order models. Modal truncation, 8<sup>th</sup> and 12<sup>th</sup> order. From input 4 to output 4.

simple modal truncation, even though other techniques, e.g. balanced truncation of order 12, appear to be more effective.

In Chapter 4 a modal analysis of the FE model of the satellite structure has been carried out. It can be noticed that a reduced order system ( $\mathbf{A}_r, \mathbf{B}_r, \mathbf{C}_r, \mathbf{D}_r$ ) of order twelve entails the inclusion of six modes, implying the exclusion of the seventh mode which has an associated frequency closed to the previous one. This consideration motivates the adoption of a reduced model in which seven modes are included, i.e. a reduced system of order fourteen. In Figure 5.8 is illustrated the frequency behaviour of the chosen reduced order model, in comparison with the full, 56<sup>th</sup> order system.

### 5.3 Application of the Reduction Algorithms

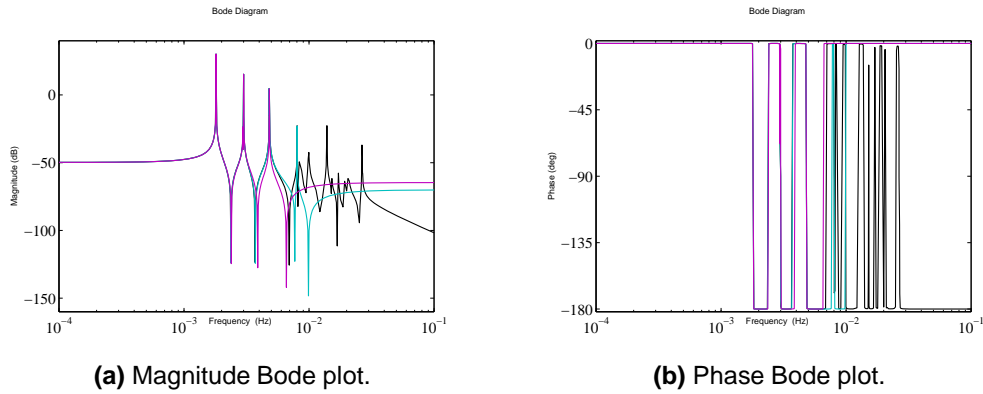


**Figure 5.5:** Bode plots of the reduced order models. Singular perturbation approximation, 8<sup>th</sup> and 12<sup>th</sup> order. From input 4 to output 4.

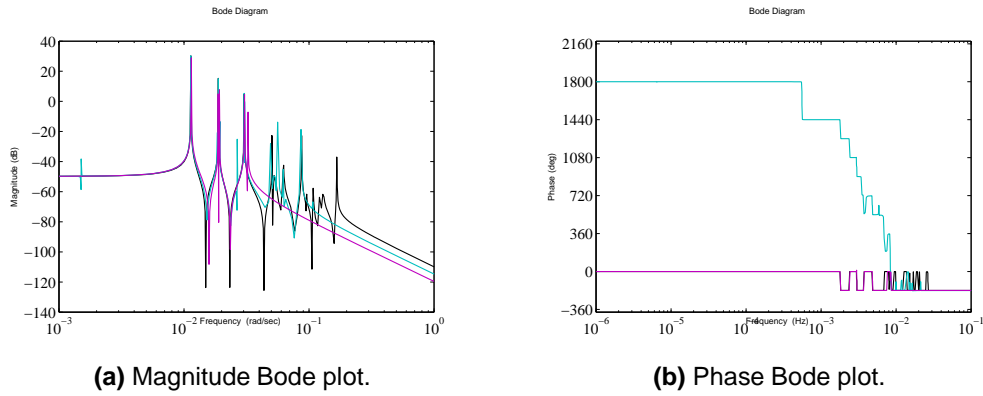


**Figure 5.6:** Bode plots of the reduced order models. Matching moments, 8<sup>th</sup> and 12<sup>th</sup> order. From input 4 to output 4.

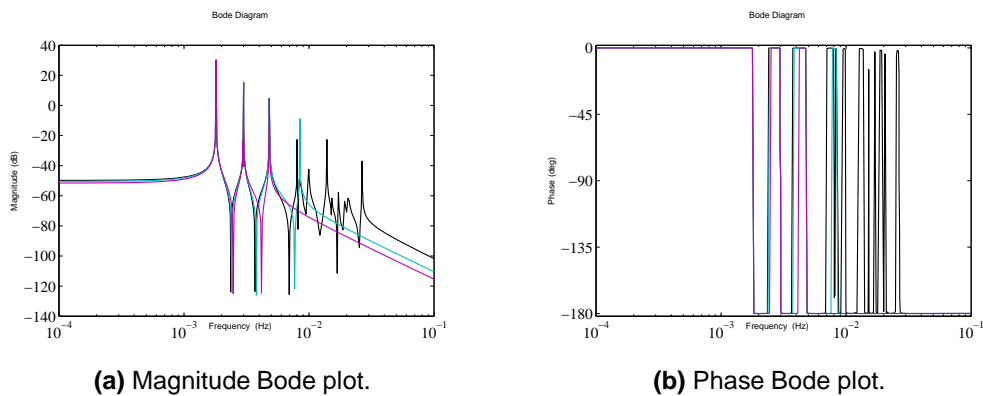


**Figure 5.7:** Bode plots of the reduced order models. Balanced reduction, 8<sup>th</sup> and 12<sup>th</sup> order. From input 4 to output 4.

**Table 5.1:**  $\mathcal{H}_\infty$  norm of the approximation error committed in using the different reduction technique.

Method	Modal Truncation			Singular Perturbation		Matching Moments		Balanced Truncation	
	8	12	14	8	12	18	36	8	12
$\ \mathbf{G} - \mathbf{G}_r\ _\infty$	0.2707	0.2707	0.2707	0.2707	0.2707	1.6253	2.4737	0.2707	0.1038

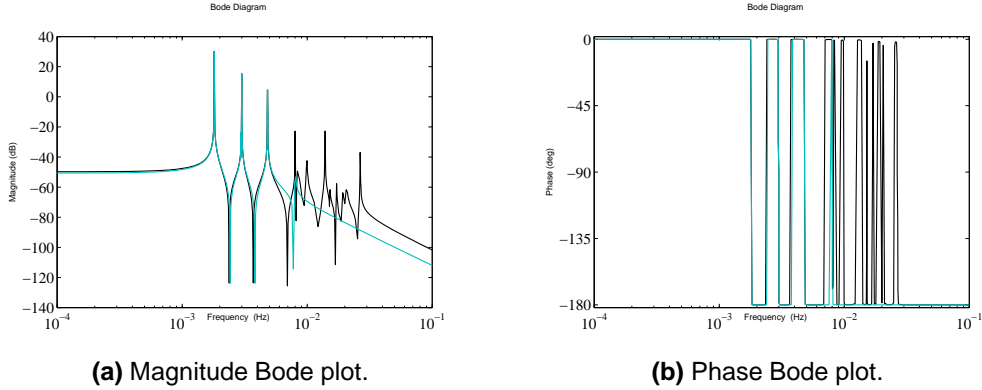


**Figure 5.8:** Bode plots of the final considered reduced order model. Modal truncation, 14<sup>th</sup> order. From input 4 to output 4.

# Chapter 6

## Vibration Suppression System

In Section 1.3 is underlined the appropriateness of having a control system which carries out vibration suppression.

To this concern, when designing controllers for dynamical models (even linearised models) of large space structures, three major problems usually arise [JK93].

- Many of the available control methods assume that the full-state vector, or an estimate of it, is available. However, in most practical situations, the estimation algorithms and associated control laws encounter difficulties when only a low-dimensional subset of the state vector is measured. On the other hand, real time implementation of high-dimensional estimators are computationally unattractive.
- It is computationally expansive to design controllers for extremely high order systems such as those arising from FE models of flexible structure. It is usually more feasible to design a controller based on a reduced-order, which includes only the most important subset of vibration modes.

### 6.1 Linear Output Feedback Control

When the full-state vector of a large dynamical system is not neither available nor practical to be reconstructed by an estimator, there exists an alternative solution, often profitably applicable. It is based on the idea of producing a control action proportional to the available measures, that is,

$$\mathbf{u} = -\mathbf{K}\mathbf{y}. \quad (6.1)$$

In this case, an estimation of the full-state vector is not necessary and a considerable simplification of the resulting control system can be achieved. Nevertheless, this simplification usually entails the optimal value of an appropriate performance

index to be higher than that that could be determined by means of a classical LQR. For this reason the output feedback control is known as to be a sub-optimal control.

### 6.1.1 Stability Analysis

Consider the class of dynamical systems modelled by the following equation of motion, which usually results from numerical simulation of flexible structures,

$$\mathbf{M}\ddot{\mathbf{a}} + \mathbf{C}_d\dot{\mathbf{a}} + \mathbf{K}\mathbf{a} = \mathbf{\Gamma}\mathbf{u}, \quad (6.2)$$

in which  $\mathbf{M}$  is the positive definite mass matrix,  $\mathbf{K}$  is the positive, at least semi-definite, stiffness matrix and  $\mathbf{C}_d$  is the damping matrix that is defined as a linear combination of the previous matrices as in (4.16).

Assuming to carry out independent measures of position and velocity, the output relation can be written as,

$$\mathbf{y} = \begin{Bmatrix} \mathbf{y}_p \\ \mathbf{y}_v \end{Bmatrix} = \begin{bmatrix} \mathbf{C}_p & \mathbf{0} \\ \mathbf{0} & \mathbf{C}_v \end{bmatrix} \begin{Bmatrix} \mathbf{a} \\ \dot{\mathbf{a}} \end{Bmatrix}. \quad (6.3)$$

Hence, a direct feedback action is determined as,

$$\mathbf{u} = -(\mathbf{K}_p\mathbf{y}_p + \mathbf{K}_v\mathbf{y}_v) = -(\mathbf{K}_p\mathbf{C}_p\mathbf{a} + \mathbf{K}_v\mathbf{C}_v\dot{\mathbf{a}}). \quad (6.4)$$

Substituting the latter expression into (6.2) leads to the following equation describing the closed-loop system,

$$\mathbf{M}\ddot{\mathbf{a}} + (\mathbf{C}_d + \mathbf{\Gamma}\mathbf{K}_v\mathbf{C}_v)\dot{\mathbf{a}} + (\mathbf{K} + \mathbf{\Gamma}\mathbf{K}_p\mathbf{C}_p)\mathbf{a} = \mathbf{0}. \quad (6.5)$$

If it is supposed that the needed measures are carried out at exactly the same positions in which the actuation takes place (collocated sensors and actuators), the following symmetric output feedback form the control law can be introduced,

$$\mathbf{y} = \begin{Bmatrix} \mathbf{y}_p \\ \mathbf{y}_v \end{Bmatrix} = \begin{bmatrix} \mathbf{\Gamma}^T & \mathbf{0} \\ \mathbf{0} & \mathbf{\Gamma}^T \end{bmatrix} \begin{Bmatrix} \mathbf{a} \\ \dot{\mathbf{a}} \end{Bmatrix}. \quad (6.6)$$

since it is  $\mathbf{C}_p = \mathbf{C}_v = \mathbf{\Gamma}^T$ . The closed-loop equations can now be written as,

$$\mathbf{M}\ddot{\mathbf{a}} + (\mathbf{C}_d + \mathbf{\Gamma}\mathbf{K}_v\mathbf{\Gamma}^T)\dot{\mathbf{a}} + (\mathbf{K} + \mathbf{\Gamma}\mathbf{K}_p\mathbf{\Gamma}^T)\mathbf{a} = \mathbf{0}. \quad (6.7)$$

Equation (6.7) states that, if  $\mathbf{K}_p$  and  $\mathbf{K}_v$  are positive definite, then the control-induced damping and stiffness perturbations  $\mathbf{\Gamma}\mathbf{K}_p\mathbf{\Gamma}^T$  and  $\mathbf{\Gamma}\mathbf{K}_v\mathbf{\Gamma}^T$  are symmetric positive definite. This characteristic can be imposed taking advantage of the possibility of freely assigning a desired structure to the gain matrices. It can be shown

that, if this is the case, asymptotic stability of the closed-loop system is guaranteed [JK93].

Moreover, an important consequence is that the stability is maintained regardless the number of states retained in the reduced-order model, regardless of inaccuracies in the parameter values used in the structural model and even in the event of a breakdown of some sensors and actuators; only the predicted performances (and the optimality index) would be degraded. Thus, by using the symmetric output feedback controller, the instability problems due to spillover effects seem to be completely avoided, and the parameters of the model do not have to be accurately known.

In fact, these assertions must be tempered when taking into account the real dynamics of sensors and actuators, delays in possible digital realizations and non-linear effects such as saturations of the actuators.

### 6.1.2 Stability Robustness Analysis

In practice, exact sensors and actuators collocation is generally impossible to achieve. Hence, this section deals with a preliminary analysis of the robustness of symmetric output feedback controllers due to imprecise collocation of sensors and actuators.

The first-order state-space realization of (6.7) is,

$$\dot{\mathbf{x}} = \mathbf{A}\mathbf{x} \quad (6.8)$$

where

$$\mathbf{x} = \begin{Bmatrix} \mathbf{a} \\ \dot{\mathbf{a}} \end{Bmatrix} \quad \text{and} \quad \mathbf{A} = \begin{bmatrix} \mathbf{0} & \mathbf{I} \\ -\mathbf{M}^{-1}(\mathbf{K} + \mathbf{\Gamma}\mathbf{K}_p\mathbf{\Gamma}^T) & -\mathbf{M}^{-1}(\mathbf{C}_d + \mathbf{\Gamma}\mathbf{K}_v\mathbf{\Gamma}^T) \end{bmatrix}. \quad (6.9)$$

Let  $\mathbf{P}$  be some positive definite matrix and consider the Lyapunov equation,

$$U(\mathbf{x}) = \mathbf{x}^T \mathbf{P} \mathbf{x}. \quad (6.10)$$

Using (6.8), the time derivative of the Lyapunov function becomes,

$$\dot{U} = \mathbf{x}^T (\mathbf{A}^T \mathbf{P} + \mathbf{P} \mathbf{A}) \mathbf{x} = -\mathbf{x}^T \mathbf{Q} \mathbf{x}. \quad (6.11)$$

Since the closed-loop system (6.8) is asymptotically stable, for any given positive definite  $\mathbf{Q}$  there exists a positive definite  $\mathbf{P}$  that is solution of the following Lyapunov equation,

$$\mathbf{A}^T \mathbf{P} + \mathbf{P} \mathbf{A} = -\mathbf{Q}. \quad (6.12)$$

Suppose that the sensors and the actuators are not precisely collocated and introduce the non-collocation perturbation matrices,  $\mathbf{\Lambda}_p$  and  $\mathbf{\Lambda}_v$ , due to which the

---

output relation becomes,

$$\mathbf{y} = \begin{Bmatrix} \mathbf{y}_p \\ \mathbf{y}_v \end{Bmatrix} = \begin{bmatrix} (\mathbf{\Gamma} + \mathbf{\Lambda}_p)^\top & \mathbf{0} \\ \mathbf{0} & (\mathbf{\Gamma} + \mathbf{\Lambda}_v)^\top \end{bmatrix} \begin{Bmatrix} \mathbf{a} \\ \dot{\mathbf{a}} \end{Bmatrix}. \quad (6.13)$$

The following theorem, proven in [Jos89], gives an upper bound on the size of non-collocation matrices which guarantee stability.

**Theorem 3.** *The closed-loop system (6.8) with imprecisely collocated sensors and actuators is asymptotically stable if,*

$$\|\mathbf{K}_p\|_2 \|\mathbf{\Lambda}_p\|_2 + \|\mathbf{K}_v\|_2 \|\mathbf{\Lambda}_v\|_2 \leq \frac{\lambda_m(\mathbf{M})}{2\|\mathbf{\Gamma}\|_2 \lambda_M(\tilde{\mathbf{P}})}, \quad (6.14)$$

where  $\tilde{\mathbf{P}}$  is the solution of the Lyapunov equation (6.12) when  $\mathbf{Q}$  is an identity matrix, whilst  $\lambda_m$  and  $\lambda_M$  denotes respectively the smallest and the largest singular value of a matrix.

This theorem does not take into account possible unmodelled actuators and sensors dynamics or non-linearities, though it gives an indication of good robustness of the symmetric output feedback controller.

## 6.2 Unstructured Suboptimal Control

The dynamical system modelled by (6.2), with collocated sensors and actuators, can be written in its state-space realization as,

$$\begin{Bmatrix} \dot{\mathbf{a}} \\ \ddot{\mathbf{a}} \end{Bmatrix} = \begin{bmatrix} \mathbf{0} & \mathbf{I} \\ -\mathbf{M}^{-1}\mathbf{K} & -\mathbf{M}^{-1}\mathbf{C}_d \end{bmatrix} \begin{Bmatrix} \mathbf{a} \\ \dot{\mathbf{a}} \end{Bmatrix} + \begin{bmatrix} \mathbf{0} \\ \mathbf{M}^{-1}\mathbf{\Gamma} \end{bmatrix} \mathbf{u} = \mathbf{Ax} + \mathbf{Bu}. \quad (6.15)$$

$$\mathbf{y} = \begin{bmatrix} \mathbf{\Gamma}^\top & \mathbf{0} \\ \mathbf{0} & \mathbf{\Gamma}^\top \end{bmatrix} \begin{Bmatrix} \mathbf{a} \\ \dot{\mathbf{a}} \end{Bmatrix} = \mathbf{Cx}. \quad (6.16)$$

Consider to employ a symmetric output feedback controller  $\mathbf{u} = -\mathbf{Ky}$  seeking to minimize the following performance index,

$$J = \int_0^\infty \mathbf{x}^\top \mathbf{Q} \mathbf{x} + \mathbf{u}^\top \mathbf{R} \mathbf{u} dt = \int_0^\infty \mathbf{x}^\top \mathbf{W}(\mathbf{K}) \mathbf{x} dt. \quad (6.17)$$

where

$$\mathbf{W}(\mathbf{K}) = \mathbf{Q} + \mathbf{C}^\top \mathbf{K}^\top \mathbf{R} \mathbf{K} \mathbf{C}. \quad (6.18)$$

If the system is perturbed by some initial conditions  $\mathbf{x}_0$ , the problem of minimizing the performance index can be restated as follows,

$$\min(J) = \min_{\mathbf{P}, \mathbf{K}} (\text{trace}(\mathbf{P}\mathbf{x}_0)), \quad (6.19)$$

in which  $P$  is a symmetric matrix satisfying the following Lyapunov equation,

$$\underbrace{(\mathbf{A}^T - \mathbf{C}^T \mathbf{K}^T \mathbf{B}^T)}_{\bar{\mathbf{A}}^T} \mathbf{P} + \mathbf{P} \underbrace{(\mathbf{A} - \mathbf{B} \mathbf{K} \mathbf{C})}_{\bar{\mathbf{A}}} + \mathbf{W}(\mathbf{K}) = \mathbf{0}, \quad (6.20)$$

and  $\mathbf{X}_0$  is an appropriate matrix which comprises the interactions between the different components of the initial condition  $\mathbf{x}_0$ . This constrained minimization can be translated into the corresponding unconstrained problem by means of the introduction of the Lagrange multipliers matrix  $\Lambda$ . Hence, the new performance index to be minimized is,

$$\tilde{J} = \mathbf{P} \mathbf{X}_0 + \Lambda (\bar{\mathbf{A}}^T \mathbf{P} + \mathbf{P} \bar{\mathbf{A}} + \mathbf{W}(\mathbf{K})). \quad (6.21)$$

Computation of the correspondent stationarity conditions leads to the following system of matrix equations,

$$\frac{\partial \tilde{J}}{\partial \Lambda} = \bar{\mathbf{A}}^T \mathbf{P} + \mathbf{P} \bar{\mathbf{A}} + \mathbf{W}(\mathbf{K}) = \mathbf{0} \quad (6.22a)$$

$$\frac{\partial \tilde{J}}{\partial \mathbf{P}} = \bar{\mathbf{A}} \Lambda + \Lambda \bar{\mathbf{A}}^T + \mathbf{X}_0 = \mathbf{0} \quad (6.22b)$$

$$\frac{\partial \tilde{J}}{\partial \mathbf{K}} = \mathbf{R} \mathbf{K} \mathbf{C} \mathbf{A} \mathbf{C}^T - \mathbf{B}^T \mathbf{P} \mathbf{A} \mathbf{C}^T = \mathbf{0} \quad (6.22c)$$

From the latter equation, it is immediate to determine the gain matrix as,

$$\mathbf{K} = \mathbf{R}^{-1} (\mathbf{B}^T \mathbf{P} \mathbf{A} \mathbf{C}^T) (\mathbf{C} \mathbf{A} \mathbf{C}^T)^{-1}. \quad (6.23)$$

### 6.2.1 Gain Matrix Computation Algorithm

As can be inferred from expression (6.23), the gain matrix of the symmetric output feedback controller depends on both  $\mathbf{P}$  and  $\Lambda$ . This means that it is not possible to refer to a single Algebraic Riccati Equation (ARE), and therefore an iterative solution of the problem appears unavoidable. In Algorithm 7 a simple iterative procedure used to find the gain matrix for the output feedback control is outlined.

**Algorithm 7.** Given the system of equations (6.22)

1. Find a stabilizing  $\mathbf{K}^{(0)}$  for the closed-loop system  $\dot{\mathbf{x}} = (\mathbf{A} - \mathbf{B} \mathbf{K} \mathbf{C}) \mathbf{x}$ .
2. Calculate  $\mathbf{P}^{(0)}$  with (6.22a).
3. Set  $J^* = 10^{30}$ ,  $\varepsilon_J = 10^{-10}$  and  $\varepsilon_\alpha = 10^{-15}$ .
4. Calculate  $\Lambda^{(0)}$  with equation (6.22b).

5. Determine  $\Delta\mathbf{K}^{(1)} = \mathbf{R}^{-1} (\mathbf{B}^T \mathbf{P}^{(0)} \mathbf{\Lambda}^{(0)} \mathbf{C}^T) (\mathbf{C} \mathbf{\Lambda}^{(0)} \mathbf{C}^T)^{-1} - \mathbf{K}^{(0)}$ .
6. Set  $\alpha = 1$  and calculate  $\mathbf{K}^{(1)} = \mathbf{K}^{(0)} + \alpha \Delta\mathbf{K}^{(1)}$ .
7. If the closed-loop system with  $\mathbf{K}^{(1)}$  is not stable, halve  $\alpha$  and return to 6. Iterate until stability is achieved or  $\alpha < \varepsilon_\alpha$ .
8. Calculate  $\mathbf{P}^{(1)}$  and  $J = \text{trace}(\mathbf{P}\mathbf{X}_0)$ .
9. If the system is stable and  $J < J^*$ , set  $J^* = J$ .
10. Iterate until  $\left| \frac{J}{J^*} - J^* \right| < \varepsilon_J$ .

In order to be able to start the mentioned iterative procedure it is necessary to find a stabilizing initial guess  $\mathbf{K}^{(0)}$ . If this initialization turned out to be difficult, it would be advisable to employ an eigenvalue shifting technique before beginning with the algorithm.

In case of arbitrary constraints upon the structure of the gain matrix  $\mathbf{K}$ , the direct solution of system (6.22) could be difficult. For this reason it is often preferred the alternative approach of a direct numerical optimization, even constrained, of the performance index.

### 6.3 Simulation results

In the previous sections it is underlined that the employment of a direct state feedback control law, being the full state of the system hardly recoverable, is unaffordable when dealing with large flexible structures. This motivates the recourse to the class of direct output feedback regulators that generate a control action proportional to the available measures of a usually small subset of the full state. It has also been stressed in Chapter 5 the necessity of having a reduced order system to design a vibration control system.

This section shows the performance of the vibration control law, designed referring to the the reduced order model of the structure, in which the first seven modes, drawing on the discussion in Section 5.3, are retained. The control system is based on the developments of Section 6.2 where the gain matrix is computed solving the optimization problem (6.17) without imposing particular constraint upon the structure of the feedback gains. Finally a useful comparison is given with an optimal controller in which the gain matrix is calculated basing on the knowledge of the full state of the system.

The state-space system that describes the dynamics of such a structure can be

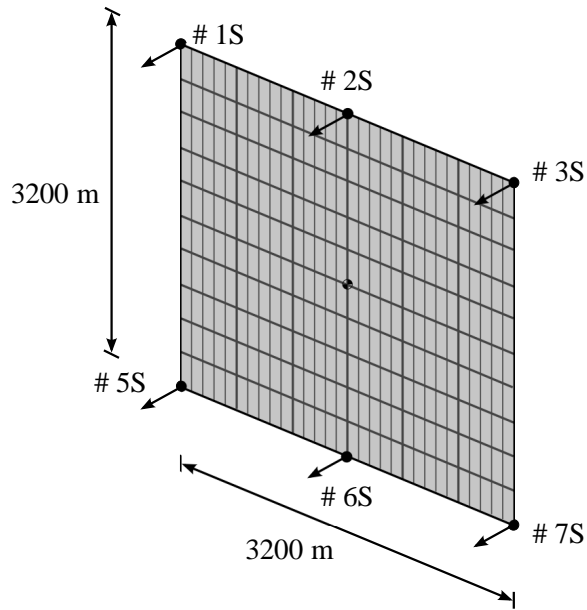


**Figure 6.1:** Actuators pattern used for the vibration suppression system.

expressed by the following,

$$\dot{\mathbf{x}} = \mathbf{Ax} + \mathbf{Bu}. \quad (6.24a)$$

$$\mathbf{y} = \mathbf{Cx}. \quad (6.24b)$$

The matrix  $\mathbf{C}$  that links the output vector with the state vector has been computed considering the positions of the actuators and sensors pairs as depicted in Figure 6.1. Referring to the results given by the modal analysis in Chapter 4, the free structure first modes turn out to be associated with the out of plane vibrations. Hence, six actuators, disposed as illustrated, assure that every mode is easily controllable. In order to prove and assess the functioning of the controllers designed to suppress the vibrations of the structure, some initial conditions are imposed. It can be shown that the imposition of initial conditions is equal to excite the system with impulsive forces and their time derivative. Consider the second-order equation of the forced system dynamics,

$$\mathbf{M}\ddot{\mathbf{a}} + \mathbf{C}_d\dot{\mathbf{a}} + \mathbf{K}\mathbf{a} = \mathbf{B}_0\delta(t) + \mathbf{B}_1\dot{\delta}(t). \quad (6.25)$$

Successive integrations yield,

$$\mathbf{M}\dot{\mathbf{a}} + \mathbf{C}_d\mathbf{a} + \mathbf{K} \int \mathbf{a} dt = \mathbf{B}_0sca(t) + \mathbf{B}_1\delta(t) + \mathbf{C}_1, \quad (6.26)$$

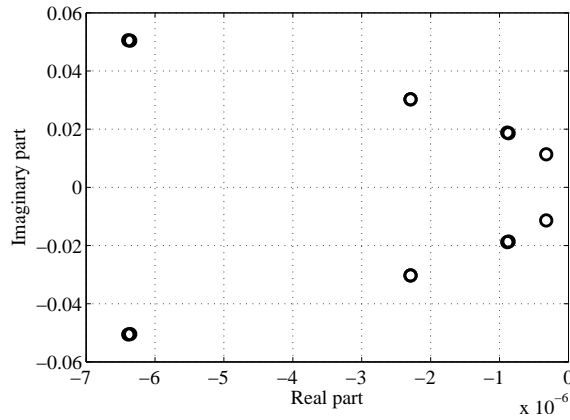


**Figure 6.2:** Open-loop eigenvalues of the reduced order system in the complex plane.

$$\mathbf{M}\mathbf{a} + \mathbf{C}_d \int \mathbf{a} dt + \mathbf{K} \iint \mathbf{a} dt = \mathbf{B}_0 \text{ramp}(t) + \mathbf{B}_1 \text{sca}(t) + \mathbf{C}_1 + \mathbf{C}_2. \quad (6.27)$$

Evaluating the integrals between  $0^-$  and  $0^+$  and supposing homogeneous initial conditions at  $0^-$ , yields,

$$\mathbf{a}(0^+) = \mathbf{M}^{-1}\mathbf{B}_1, \quad (6.28a)$$

$$\dot{\mathbf{a}}(0^+) = \mathbf{M}^{-1}(\mathbf{C}_d \mathbf{a} + \mathbf{B}_0). \quad (6.28b)$$

In the following sections, the initial conditions are calculated from the imposition of impulsive forces and their time derivative using (6.28).  $\mathbf{B}_0$  and  $\mathbf{B}_1$  are a column vectors in which forces of 1000 N (the order of magnitude of the environmental disturbances) are equally distributed onto all the translational degrees of freedom of the full structure. Eventually they are reduced by means of the same transformation matrix  $\mathbf{T}$ , used for the reduction of the system.

In Figure 6.2 are reported the eigenvalues of the open-loop reduced model. The uncontrolled motion of the structure perturbed by the imposition of initial conditions is slightly damped by the structural damping given by the matrix  $\mathbf{C}_d$ . As expected, since the internal damping is assumed to be low in order to be on the safe side, the vibrations are extinguished very slowly. This can be predicted by noticing that the open-loop eigenvalues are almost pure imaginary and is confirmed in Figure 6.3, in which, as an example, the time history of the uncontrolled third mode is depicted. The trend is analogous for the other modes.

### 6.3.1 Unstructured Suboptimal Regulator

As introduced in the previous section, an unstructured suboptimal regulator has been developed. The gain matrix has been computed following the steps outlined

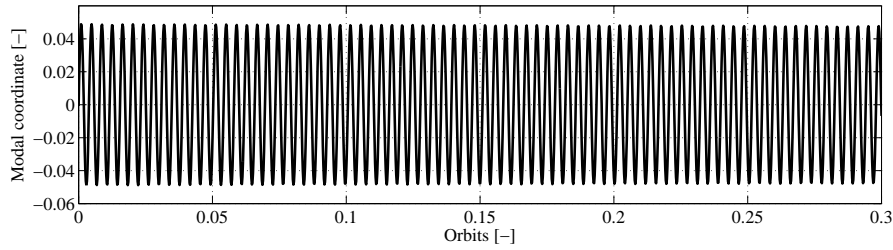


**Figure 6.3:** Uncontrolled structural vibrations with respect to the imposition of initial conditions. Mode 3.

**Table 6.1:** Closed-loop eigenvalues of the reduced order system. Unstructured Sub-optimal Regulator.

Mode	Open-Loop	Closed-Loop
1	$-0.00000032 + 0.01135258i$	$-0.00150992 + 0.01129401i$
2	$-0.00000086 + 0.01863602i$	$-0.00134120 + 0.01864962i$
3	$-0.00000088 + 0.01884402i$	$-0.00112420 + 0.01877911i$
4	$-0.00000228 + 0.03026719i$	$-0.00062441 + 0.03028173i$
5	$-0.00000229 + 0.03028664i$	$-0.00119769 + 0.03028904i$
6	$-0.00000635 + 0.05043782i$	$-0.00024016 + 0.05042173i$
7	$-0.00000638 + 0.05055180i$	$-0.00029145 + 0.05055039i$

in Algorithm 7. The following penalty matrices are determined to produce a regulator able to extinguish the structural vibrations in about one third of the orbit period.

$$\mathbf{Q}_{\text{sub}} = \text{diag} ([10 \ 200 \ 40 \ 100 \ 200 \ 1000 \ 1000 \ 10 \ 200 \ 40 \ 100 \ 200 \ 1000 \ 1000]), \quad (6.29)$$

$$\mathbf{R}_{\text{sub}} = \text{diag} ([0.015 \ 0.05 \ 0.015 \ 0.015 \ 0.025 \ 0.015]). \quad (6.30)$$

The resultant gain matrix is a fully populated matrix in which the highest values have an order of magnitude of  $10^3$ , whereas the lowest ones are of the order of  $10^{-3}$ .

In Table 6.1 and in Figure 6.4a are reported the closed-loop eigenvalues in comparison with the open-loop ones. It can be seen that the real part of the closed-loop eigenvalues are effectively moved far away from the imaginary axis by at least two orders of magnitude. The imaginary part is left practically the same for all the eigenvalues, this yielding to the damping factor of each mode to be increased. In Figure 6.5 is plotted the time history of the third modal coordinate, which can be straightforwardly compared to the uncontrolled behaviour. As expected, there is the same initial elongation as the uncontrolled case, but the following oscillations

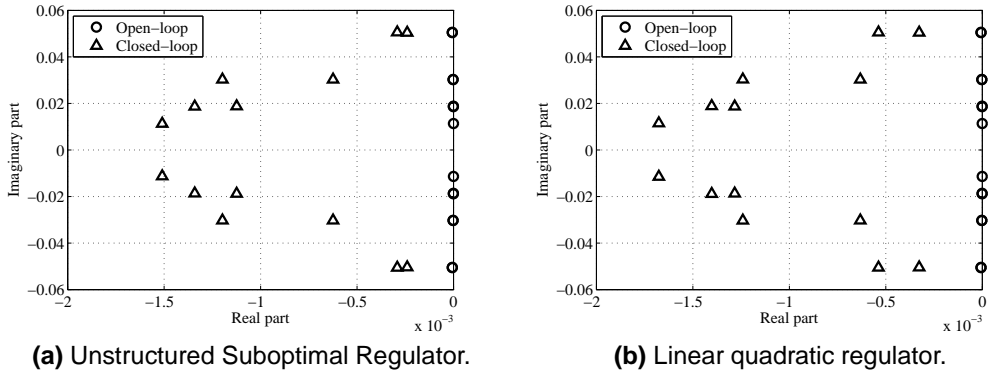


**Figure 6.4:** Closed-loop eigenvalues of the reduced order system in the complex plane.

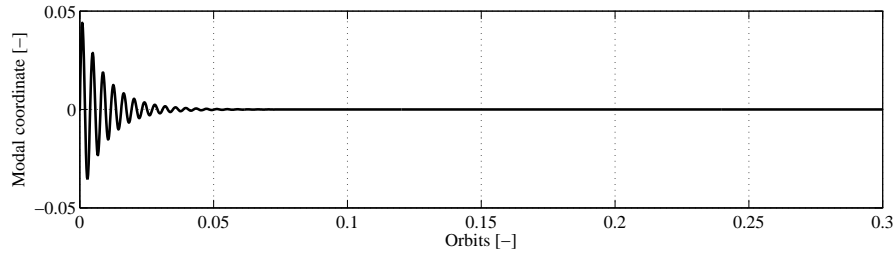


**Figure 6.5:** Controlled structural vibrations with respect to the imposition of initial conditions. Unstructured suboptimal regulator. Mode 3.

are extinguished in about a tenth of the orbital period. The same qualitative behaviour is shown by the other modes, the only difference being the time in which the fluctuations are cancelled. Recalling Table 6.1, the third mode is one of the more damped, since the associated eigenvalue is moved into the negative real part plane by almost four orders of magnitude. However, as mentioned before, all the modal coordinates considered in the reduced subsystem are damped within one third of the orbital period.

### 6.3.2 Comparison with LQR

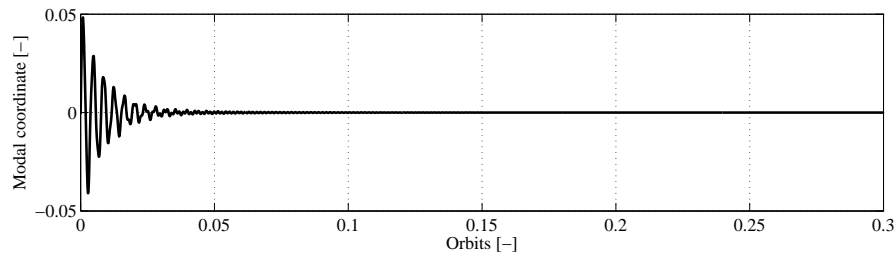
The performances of the previous controller is then compared with the dynamical system controlled by a classical LQR, supposing to know the full state vector. The following weight matrices are chosen in order to extinguish all the vibrations within one third of the orbit,

$$\mathbf{Q}_{\text{lqr}} = \text{diag} ([10 \ 30 \ 20 \ 20 \ 20 \ 50 \ 30 \ 10 \ 30 \ 20 \ 20 \ 20 \ 50 \ 30]), \quad (6.31)$$

$$\mathbf{R}_{\text{lqr}} = \text{diag} ([1 \ 1 \ 1 \ 0.1 \ 0.1 \ 0.1]). \quad (6.32)$$

**Table 6.2:** Closed-loop eigenvalues of the reduced order system. LQR.

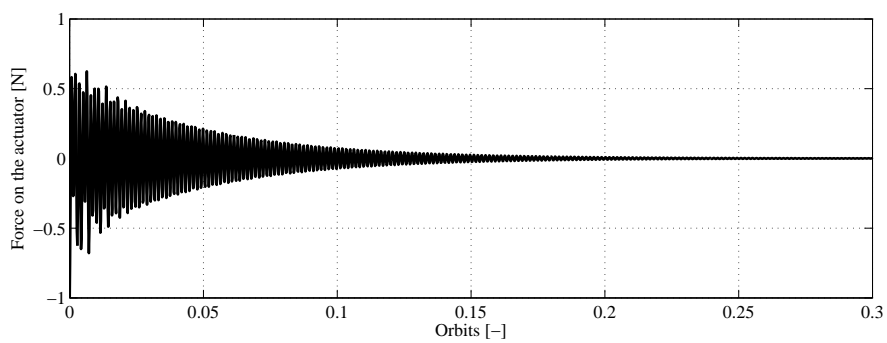
Mode	Open-Loop	Closed-Loop
1	$-0.00000032 + 0.01135258i$	$-0.00167628 + 0.01148216i$
2	$-0.00000086 + 0.01863602i$	$-0.00128350 + 0.01871441i$
3	$-0.00000088 + 0.01884402i$	$-0.00140243 + 0.01885967i$
4	$-0.00000228 + 0.03026719i$	$-0.00063204 + 0.03028603i$
5	$-0.00000229 + 0.03028664i$	$-0.00124113 + 0.03029888i$
6	$-0.00000635 + 0.05043782i$	$-0.00032686 + 0.05045831i$
7	$-0.00000638 + 0.05055180i$	$-0.00053761 + 0.05053522i$

**Figure 6.6:** Controlled structural vibrations with respect to the imposition of initial conditions. LQR. Mode 3.

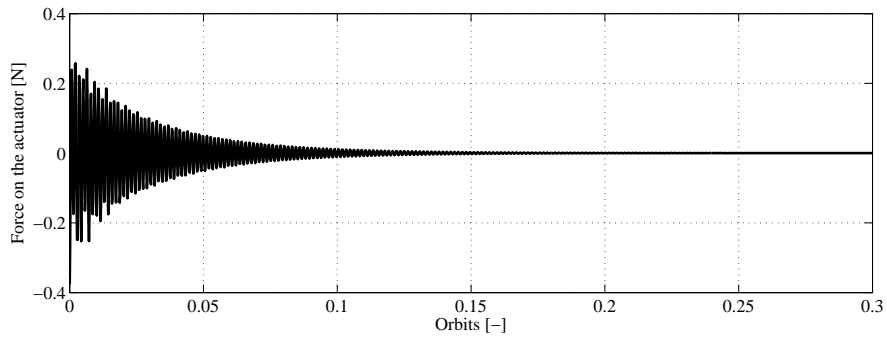
This choice yields a  $6 \times 14$  gain matrix in which the highest elements have an order of  $10^2$  and the lowest have an order of  $10^{-3}$ .

The characteristics of the resulting closed-loop employing the linear quadratic regulator, in comparison with those of the open-loop, are summarized in Table 6.2 and in Figure 6.4b. It can be noticed that the eigenvalues are moved slightly farther away from the imaginary axis in comparison with the suboptimal regulator, this being particularly true for the last two eigenvalues, at higher frequency. Nevertheless, the highest terms in the gain matrix are one order of magnitude less than those of the unstructured suboptimal regulator, suggesting that the LQR could be able to get the same results as the suboptimal regulator with less effort. This is quite expected and is confirmed by Figure 6.6, in which the time history of the third modal coordinate is plotted and can be compared with the trend of Figure 6.5. It is clear that the performances of the different regulator are highly comparable. The same observations are valid for the other modal coordinates. In order to strengthen the last considerations, in Figure 6.7, it is reported as an illustrative example, the time history of the control force exerted by the actuator #1. Even though the magnitude of the requested action is not really significant in this case, since the system is forced by fictitious initial conditions, it can be noticed that the highest peak of the force requested by the LQR is half the one needed by the

suboptimal controller. Besides, the control action appears to vanish quicker in the LQR case, suggesting that it is slightly more efficient in damping the vibrations. In conclusion, recalling that the estimation of the full state vector is not affordable when dealing with large flexible structures, this chapter proves the general reasonableness of a direct output feedback approach in carrying out the vibrations suppression problem.



**(a)** Actuator # 1S. Unstructured suboptimal regulator



**(b)** Actuator # 1S. LQR

**Figure 6.7:** Comparison between the control force provided by actuator #1.

## Chapter 7

# Integrated System Simulation Comparisons and Results

The necessity of a vibration suppression system should be verified by considering the the structural dynamics in a plausible operative situation, in which the continuous orbit and the attitude controls guarantee the station keeping and the desired attitude configuration. In particular,  $0.05^\circ$  latitude and  $0.1^\circ$  longitude are considered to be the maximum station keeping errors, while  $0.08^\circ$  attitude pointing accuracy on each axes should be guaranteed. In order to keep the orbit and the attitude of the satellite into these specific limits, the LQR approach is employed for both the orbit and attitude regulators. In particular, the following penalty matrices are considered with respect to the orbit regulator:

$$\mathbf{Q}_{\text{orb}} = \begin{bmatrix} 3 \times 10^{-14} & 0 & 0 & 0 & 0 & 0 \\ 0 & 3 \times 10^{-14} & 0 & 0 & 0 & 0 \\ 0 & 0 & 3 \times 10^{-14} & 0 & 0 & 0 \\ 0 & 0 & 0 & 10^{-9} & 0 & 0 \\ 0 & 0 & 0 & 0 & 10^{-9} & 0 \\ 0 & 0 & 0 & 0 & 0 & 10^{-9} \end{bmatrix}. \quad (7.1)$$

$$\mathbf{R}_{\text{orb}} = \begin{bmatrix} 10^6 & 0 & 0 \\ 0 & 10^6 & 0 \\ 0 & 0 & 10^6 \end{bmatrix}. \quad (7.2)$$

While the attitude penalty matrices:

$$\mathbf{Q}_{\text{att}} = \begin{bmatrix} 3 \times 10^{13} & 0 & 0 & 0 & 0 & 0 \\ 0 & 2 \times 10^{14} & 0 & 0 & 0 & 0 \\ 0 & 0 & 1 \times 10^{14} & 0 & 0 & 0 \\ 0 & 0 & 0 & 3 \times 10^{13} & 0 & 0 \\ 0 & 0 & 0 & 0 & 2 \times 10^{14} & 0 \\ 0 & 0 & 0 & 0 & 0 & 1 \times 10^{14} \end{bmatrix} \quad (7.3)$$

$$\mathbf{R}_{\text{att}} = \begin{bmatrix} 10 & 0 & 0 \\ 0 & 10 & 0 \\ 0 & 0 & 10 \end{bmatrix} \quad (7.4)$$

In the first part of the chapter, the structure is left uncontrolled. It is shown how the structural vibrations are excited by the orbit and attitude control actions in two illustrative situations: a nominal and a perturbed initial condition. It will be exhibited that two kind of structural oscillations arise from these interactions: large very low frequency oscillations, that are the natural consequence of the structural flexibility due to the nominal trend of the orbit and attitude control force, and much higher frequency vibrations in correspondence to the modal frequencies of the structure. Although the first kind of oscillations present a large amplitude, they are not considered to be dangerous for the structure, while the second kind need to be damped. In the end, it is shown how the active vibration suppression system, previously developed, is able to extinguish the undesired high frequency vibrations on the structure.

All the simulations are carried out for a time interval of 20 orbits. This is not restrictive, since a long term quasi-periodic behaviour of all the variables has been preliminary verified. Moreover the initial epoch  $t_0$  is considered to be January 1, 2012 at 12<sup>h</sup> 00' 00.0" UTC with the satellite located at the nominal longitude  $\lambda_G = 75.07^\circ$ . While the nominal attitude orientation is considered to be the ECSF reference frame directions.

In the end, three sets of actuators are considered to be independently employed for the orbit, the attitude and the structural vibration control. In particular, equivalent sets for the orbit and the attitude are adopted, as depicted in Figure 7.1. The actuators #1, #4, #8 and #11 are placed along the  $X_S$  direction, the actuators #2, #5, #9 and #12 along the  $Y_S$  direction, while the actuators #3, #6, #7 and #10. The set of actuators for the vibration suppression system consists of six actuators from #1S to #6S placed as depicted in Figure 7.2.

## 7.1 The Uncontrolled Structural Dynamics (USD) Condition

In the USD condition the structure does not have any active vibration suppression system. In particular, the hypothesis and simplifications, adopted for the Uncontrolled Structural Dynamics (USD) condition, are stated as follow:

- The orbital disturbances are caused by the major environmental disturbances together with the disturbances coming from the attitude control actions.
  - The attitude is affected by the gravity gradient torque and the solar radiation torque together with the disturbances coming from the orbit control actions.
-

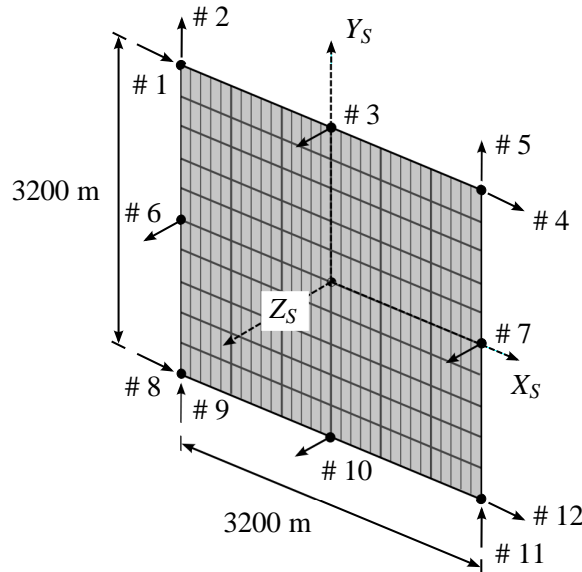


**Figure 7.1:** Actuators pattern employed for the orbital and attitude control system.

- The structural vibrations are only influenced by the orbit and the attitude control actions.

Two configurations are considered to be significant concerning the structural interactions with the rigid body motion dynamics: the Zero Initial Conditions (ZIC) and the Perturbed Initial Conditions (PIC).

### 7.1.1 The Zero Initial Conditions (ZIC) Configuration

In the ZIC configuration, the starting errors are considered to be equal to zero with respect to the nominal orbit position and the attitude pointing.

As shown in Figure 7.3, the requirements on the maximum latitude and longitude errors, of respectively  $0.05^\circ$  and  $0.1^\circ$ , are satisfied. The corresponding control actions is homogeneously distributed within the set of actuators. In particular, the a maximum force of about 30 N is required by the actuators in the  $X_S$  direction as shown in Figure 7.4. Similarly, the attitude control satisfies the pointing accuracy of  $0.08^\circ$  around each axis (Figure 7.5). As expected, the maximum control torque is requested around the  $X_S$  axis due to the significant pitch gravity gradient torque. Thus, the forces on the actuator #3 and #10 reach a maximum value of about 60 N, as shown in Figure 7.5.

The structure modal coordinates, as expected, present large very low frequency oscillations as exemplified in Figure 7.7, where the second modal coordinate be-

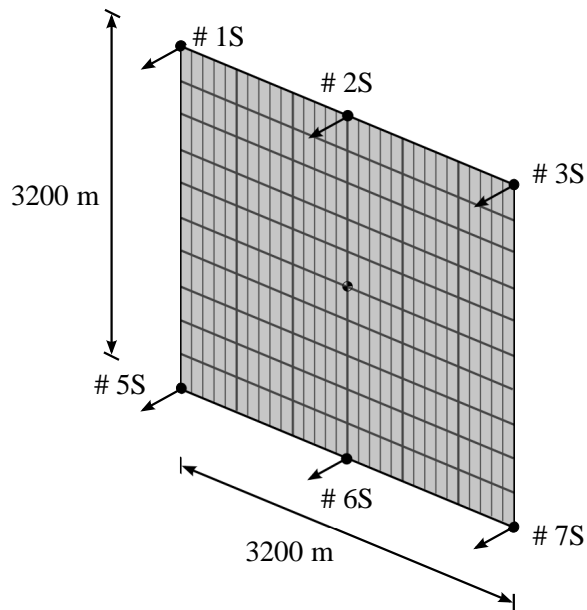


**Figure 7.2:** Actuators pattern employed for the vibration suppression system.

haviour is depicted. These kind of oscillations does not need to be extinguished. However, the first modal coordinate as well as the sixth and the seventh appear to be excited in correspondence to their related modal frequencies as exemplified in Figures 7.8, 7.9 and 7.10. As a consequence, a vibration suppression system appears be appropriate.

### 7.1.2 The Perturbed Initial Conditions (PIC) Configuration

Hereafter, the perturbed initial conditions are imposed to the orbit and the attitude nominal configuration. In the considered scenario, the spacecraft initially lays on the boundaries of the longitude and latitude admissible box with a pointing error about each axis. Particularly,  $0.05^\circ$  latitude and  $0.1^\circ$  longitude errors are considered for the position of the spacecraft on the orbit, whereas  $10^\circ$  pointing errors around each principal axis of inertia. As a consequence, a step behaviour of the control action is expected.

The requirements are met for both the orbit and the attitude controls in a time of the order of some orbits (Figures 7.12 and 7.13). As it is expected, the maximum actuator forces requested in the PIC configuration are much more higher than those in the ZIC configuration, due to the initial conditions. However, once the regime conditions are reached, the actuators forces return to the nominal behaviour (Figures 7.11 and 7.14).

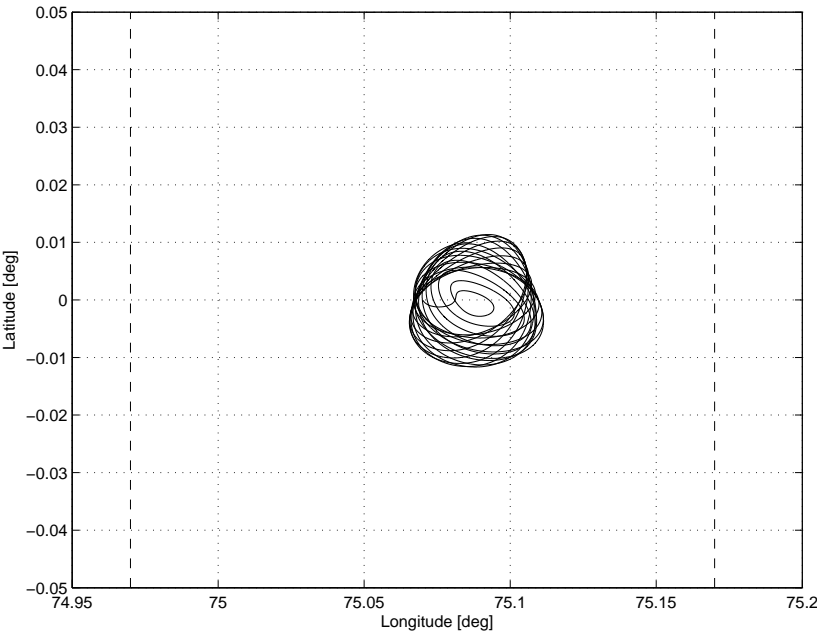


**Figure 7.3:** Time history of spacecraft longitude and latitude in the USD condition and the ZIC configuration.

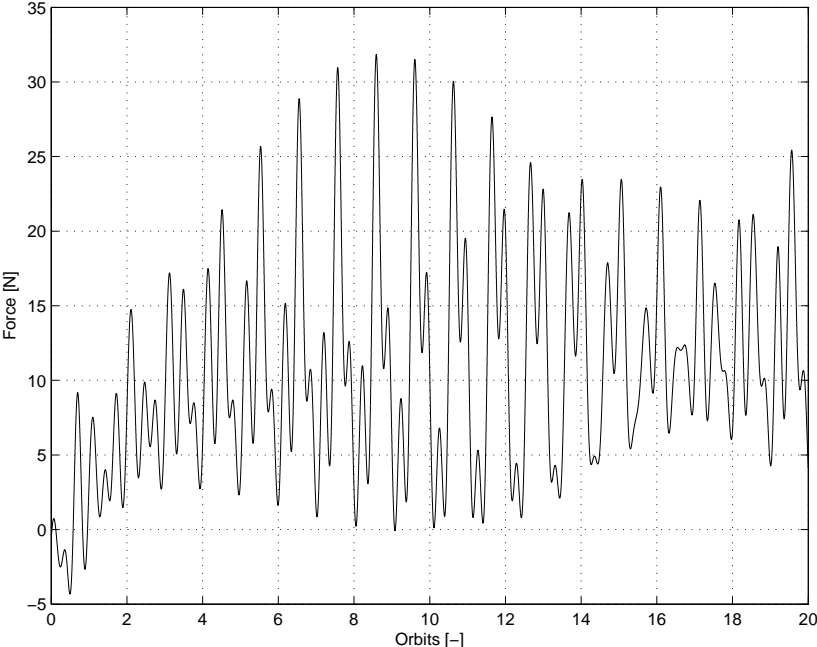


**Figure 7.4:** Force on the actuator #1 requested for the orbit control in the USD condition and the ZIC configuration.

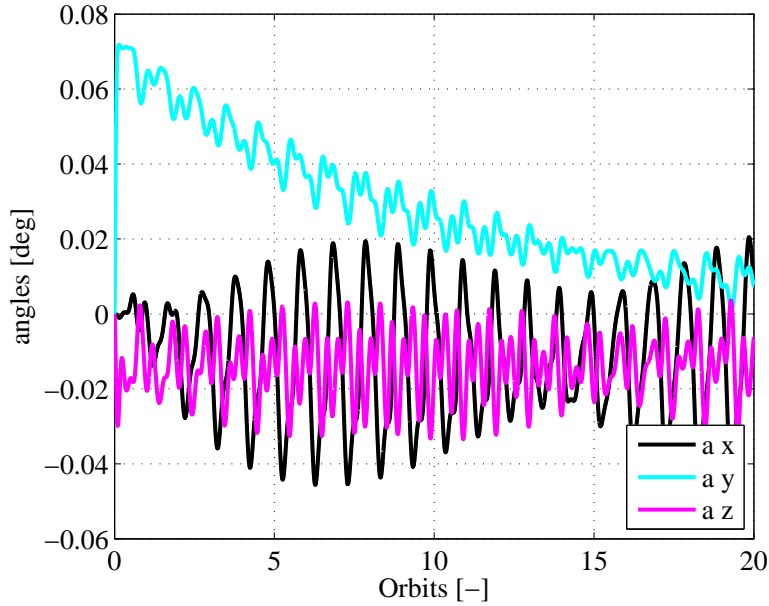


**Figure 7.5:** Attitude angles  $\alpha$  in the USD condition and the ZIC configuration.

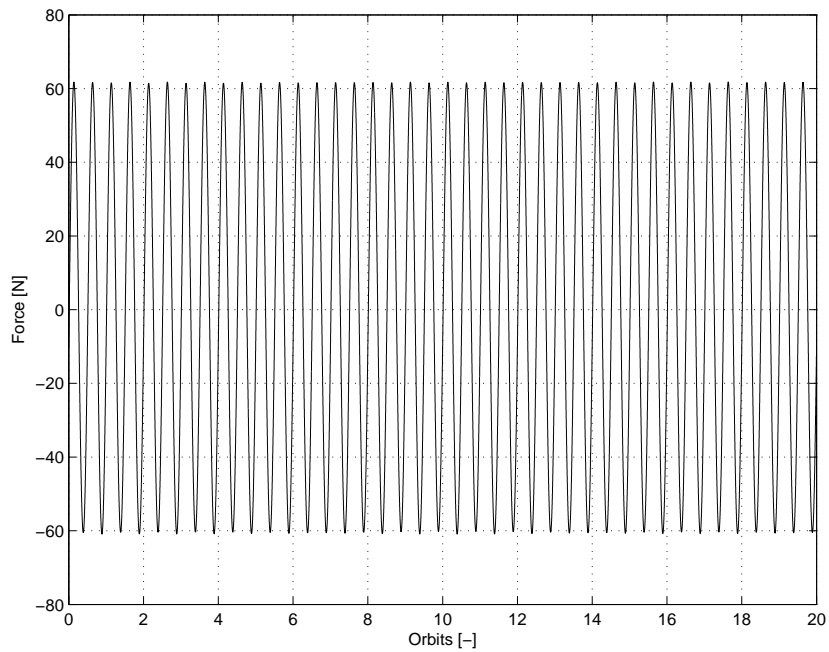


**Figure 7.6:** Force on the actuator #6 requested for the attitude control in the USD condition and the ZIC configuration.

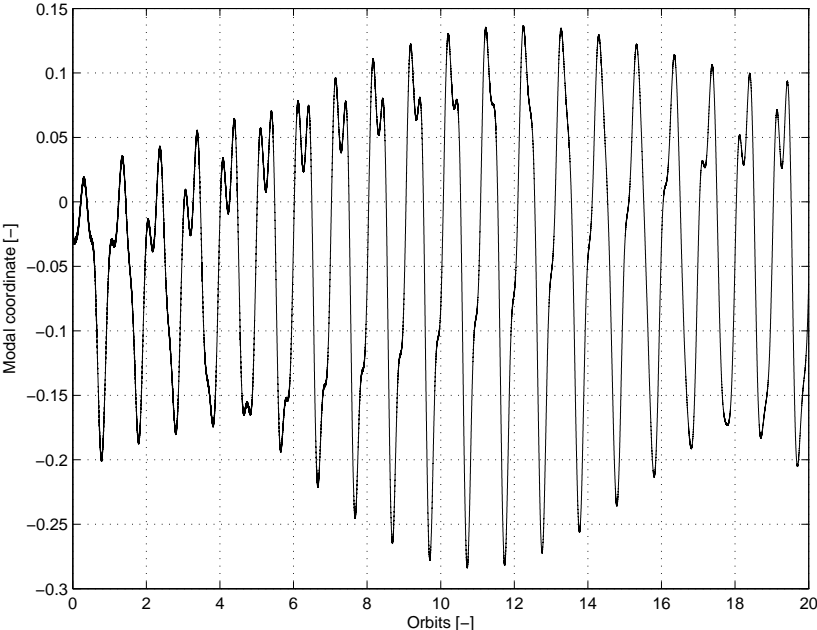


**Figure 7.7:** The second modal coordinate in the USD condition and the ZIC configuration.

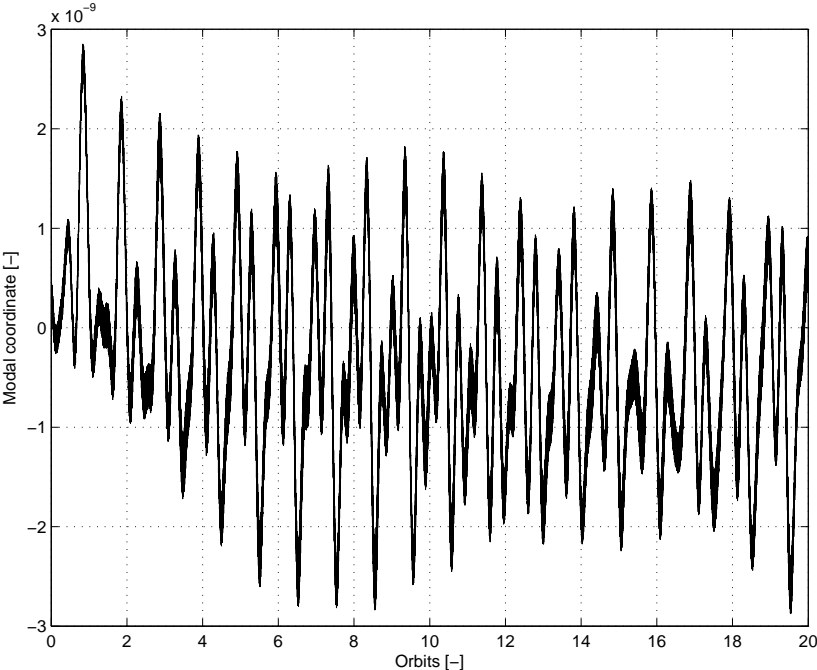


**Figure 7.8:** The first modal coordinate in the USD condition and the ZIC configuration.

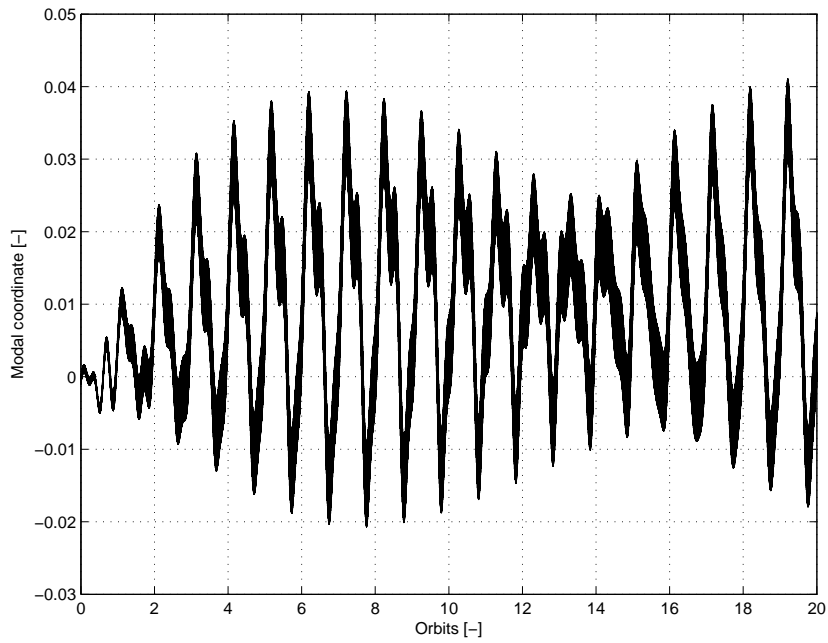


**Figure 7.9:** The sixth modal coordinate in the USD condition and the ZIC configuration.

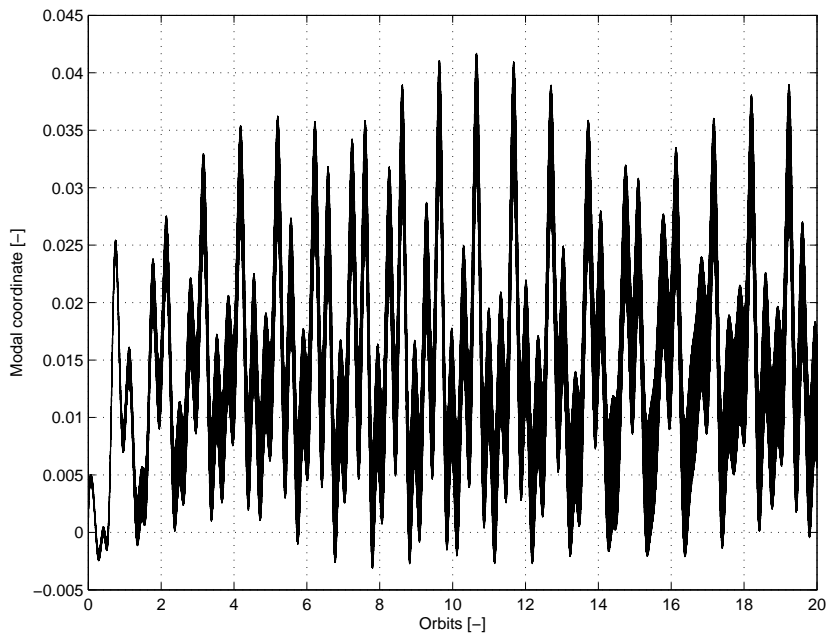


**Figure 7.10:** The seventh modal coordinate in the USD condition and the ZIC configuration.

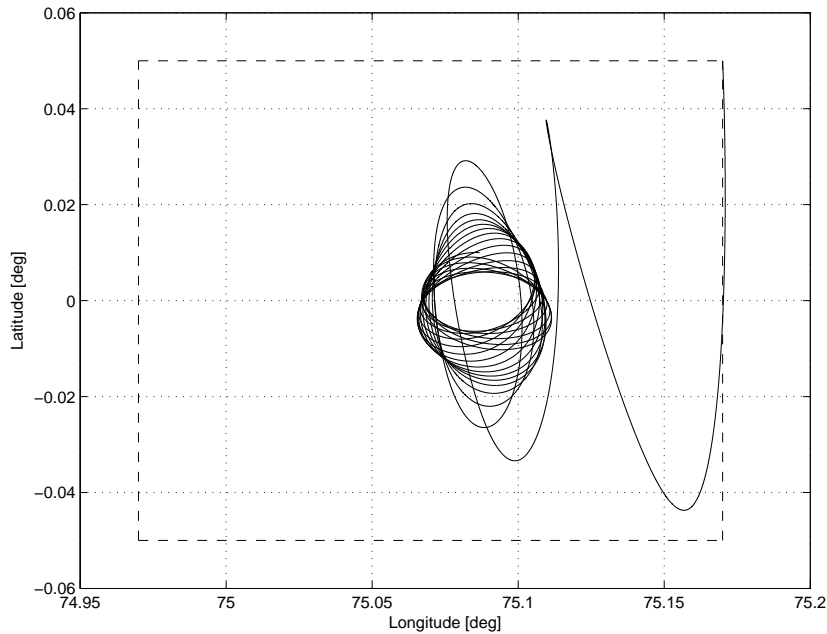


**Figure 7.11:** Time history of spacecraft longitude and latitude in the USD condition and the PIC configuration.

As a consequence of the initial strong orbit and control actions, all the modal coordinates are expected to be initially perturbed. Thus, the higher frequency vibrations, superimposed on to the lower large frequency oscillations, should be generally more significant than those in the ZIC configuration. Even if the structural damping may encourage the damping of such undesired high frequency vibrations, as it occurs for the the fifth modal coordinate (Figure 7.15), the orbit and attitude control actions may excite the vibrations in correspondence to particular modal frequencies. This is the case of the sixth and seventh modal frequencies (Figures 7.16 7.17).

Although the condition just analysed may be considered to be one of the worst case, since the step behaviour for orbit and control action, it has been shown that the possible appearance of a vibration may not be extinguished.

## 7.2 The Controlled Structural Dynamics (CSD) Condition

In the CSD condition, the high frequencies vibrations are damped by a suboptimal regulator. The penalty matrices for such a regulator have been chosen to diagonal

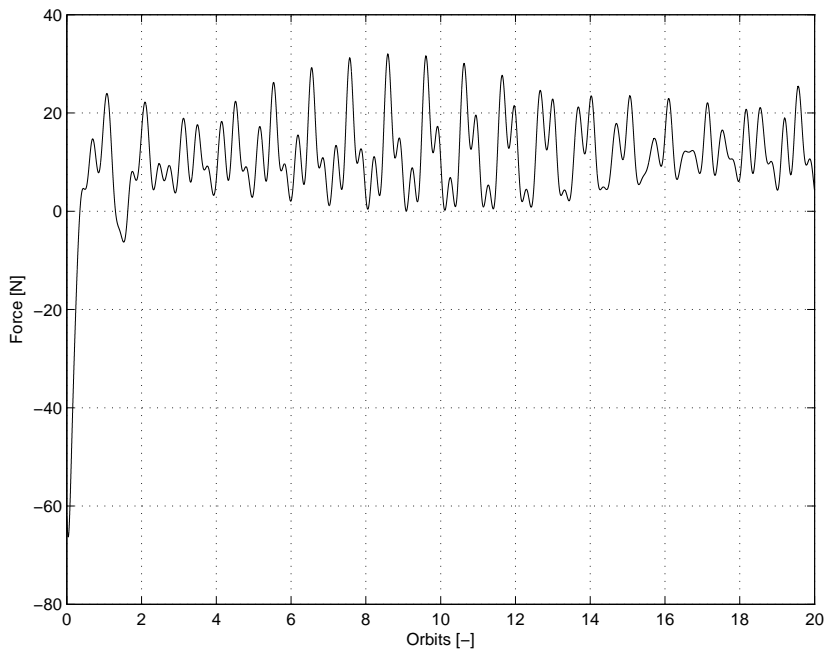


**Figure 7.12:** Force on the actuator #1 requested for the orbit control in the USD condition and the PIC configuration.

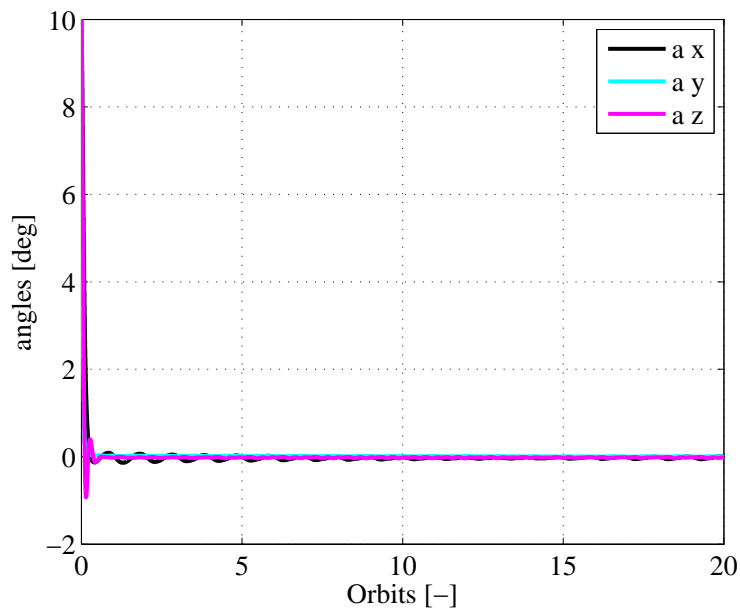


**Figure 7.13:** Attitude angles  $\alpha$  in the USD condition and the PIC configuration.

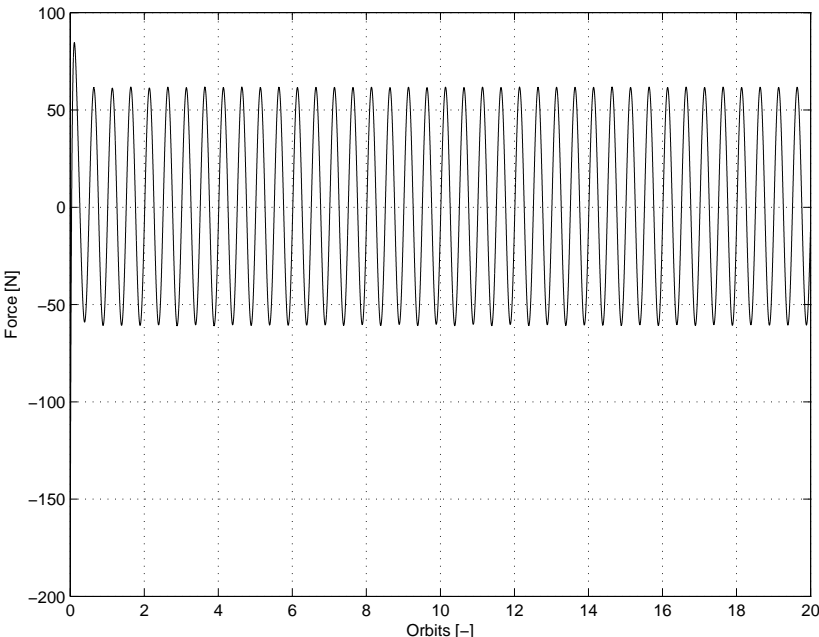


**Figure 7.14:** Force on the actuator #6 requested for the attitude control in the USD condition and the PIC configuration.

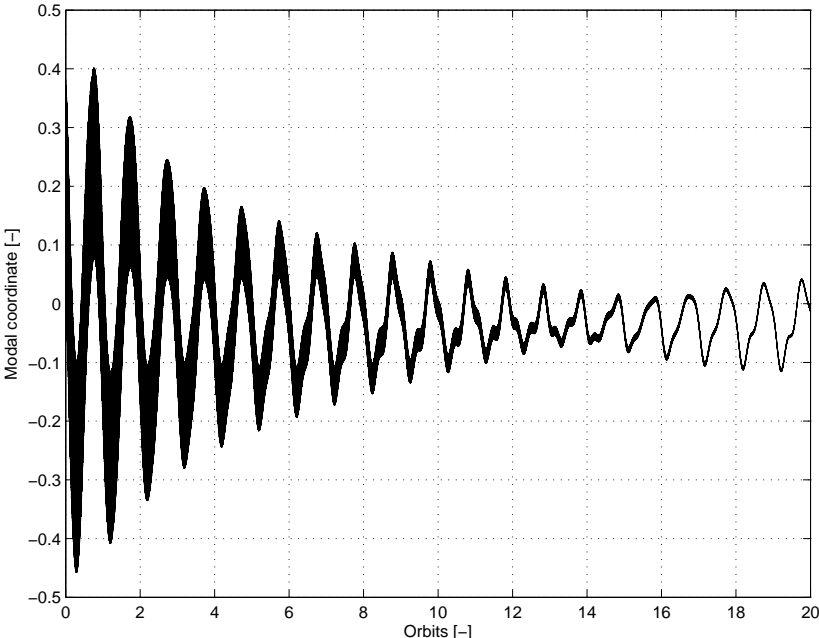


**Figure 7.15:** The fifth modal coordinate in the USD condition and the PIC configuration.

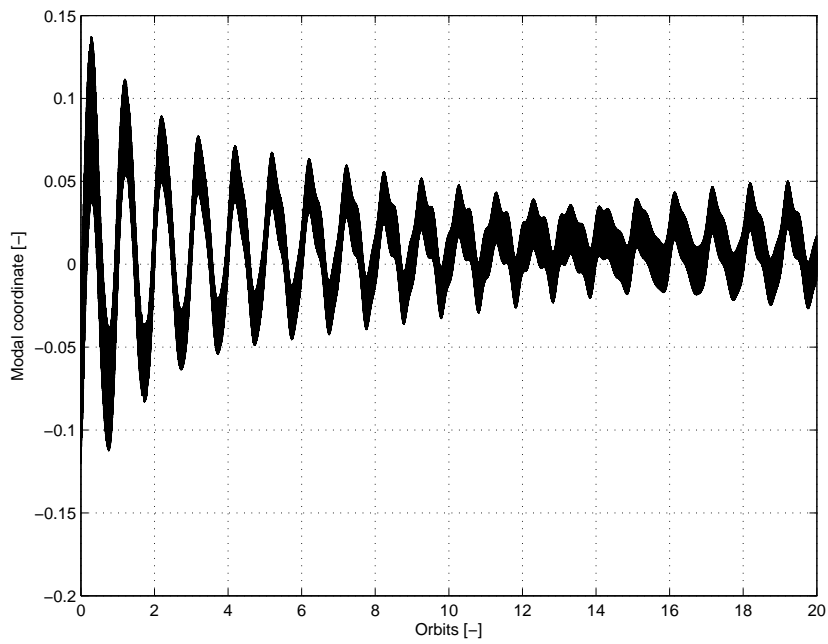


**Figure 7.16:** The sixth modal coordinate in the USD condition and the PIC configuration.

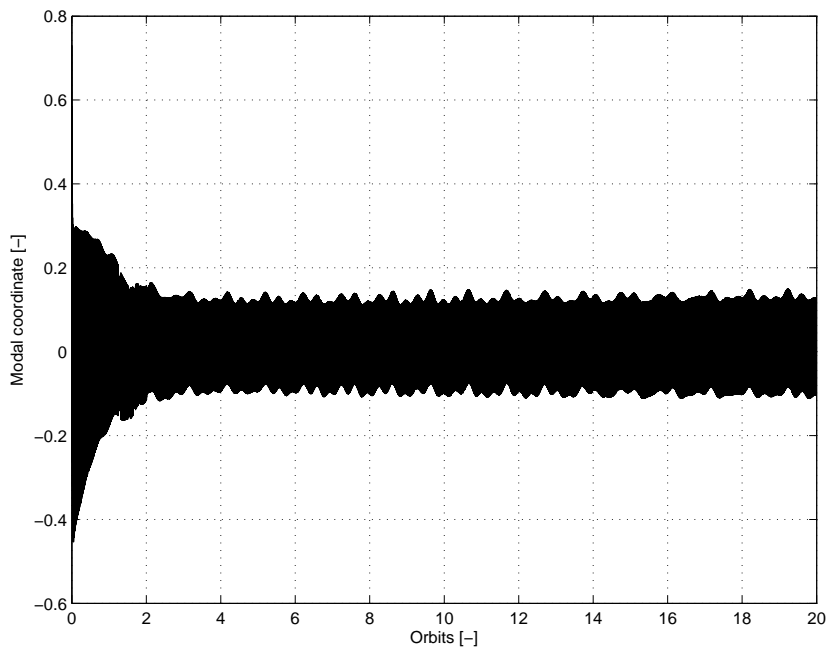


**Figure 7.17:** The seventh modal coordinate in the USD condition and the PIC configuration.

matrices with the diagonal:

$$\mathbf{Q} = \text{diag} ([10 \ 200 \ 40 \ 100 \ 200 \ 1000 \ 1000 \ 10 \ 200 \ 40 \ 100 \ 200 \ 1000 \ 1000]), \quad (7.5)$$

$$\mathbf{R} = \text{diag} ([0.015 \ 0.05 \ 0.015 \ 0.015 \ 0.025 \ 0.015]). \quad (7.6)$$

In particular, the hypothesis and simplifications, adopted for the CSD condition, are stated as follow:

- The orbital disturbances are caused by the major environmental disturbances previously described, together with the disturbances coming from the attitude and the vibration suppression control actions.
- The attitude is affected by the gravity gradient torque and the solar radiation torque together with the disturbances coming from the orbit and the vibration suppression control actions.
- The structural vibrations are only influenced by the orbit and the attitude control actions.

Only the PIC configuration is examined in the CSD condition, since it resumes the behaviour of the control systems in both the perturbed initial conditions and the nominal operative configuration. The presence of the vibration suppression system is not detrimental for the orbit and the attitude controls, which show the similar behaviour as it results considering the uncontrolled structure (Figures 7.18 and 7.20). As a consequence, the actuators forces are expected to be comparable, as exemplified in Figures 7.19 and 7.21, where the behaviours of the actuators #1 and #6, respectively for the orbit and attitude control, are depicted.

Concerning the structural behaviour, the large low frequency oscillations appear to have the same behaviour of those of the uncontrolled structure. This is what results observing Figure 7.22, which represents the sixth modal coordinate low frequency trend. However, if the very initial time intervals are considered, it is evident that the vibration suppression system is able to extinguish the undesired high frequency vibrations (Figures from 7.23 to 7.29). Moreover, the correspondent action required by the vibration suppression system is of the same order as that required for the orbit and attitude control systems, as results observing Figures from 7.30 to 7.35.

The simulations described in this chapter show that the interaction between the orbit and attitude control systems and the structure could be potentially dangerous. A suboptimal control approach for the vibration suppression has been introduced and yields satisfactory results. It is to be underlined that the aforementioned vibrations suppression system has been designed considering a reduced order structural model including the first seven flexible modes. Although the order of the reduced

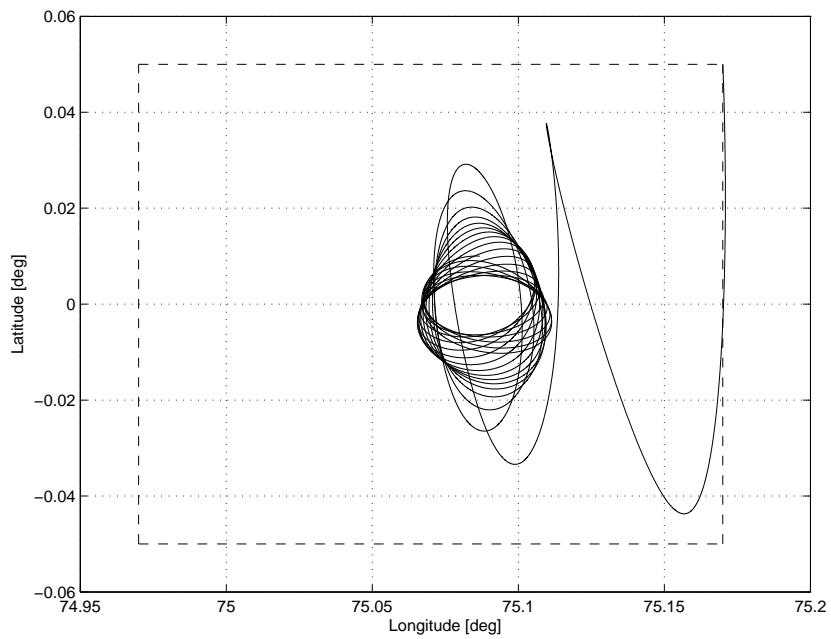


**Figure 7.18:** Time history of spacecraft longitude and latitude in the CSD condition.

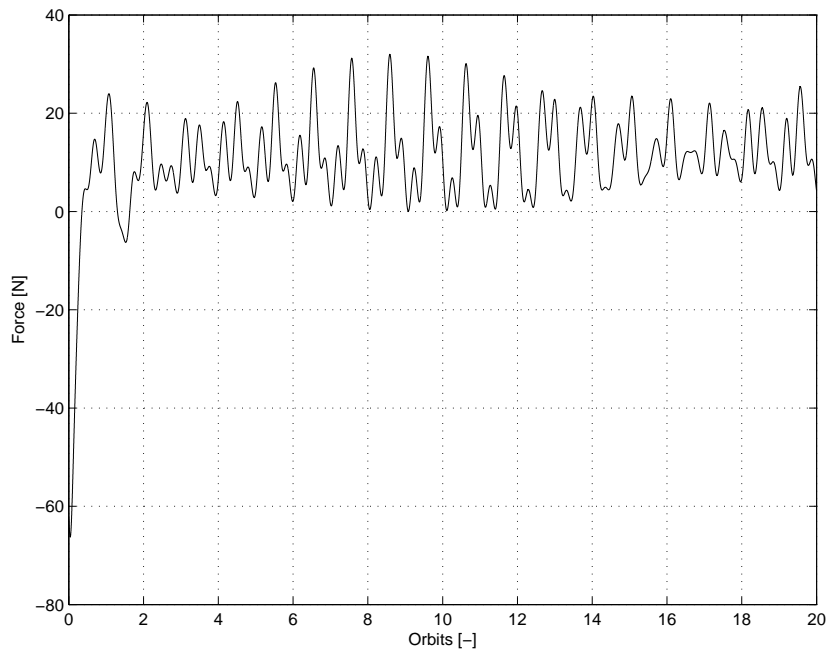


**Figure 7.19:** Force on the actuator #1 requested for the orbit control in the CSD condition.

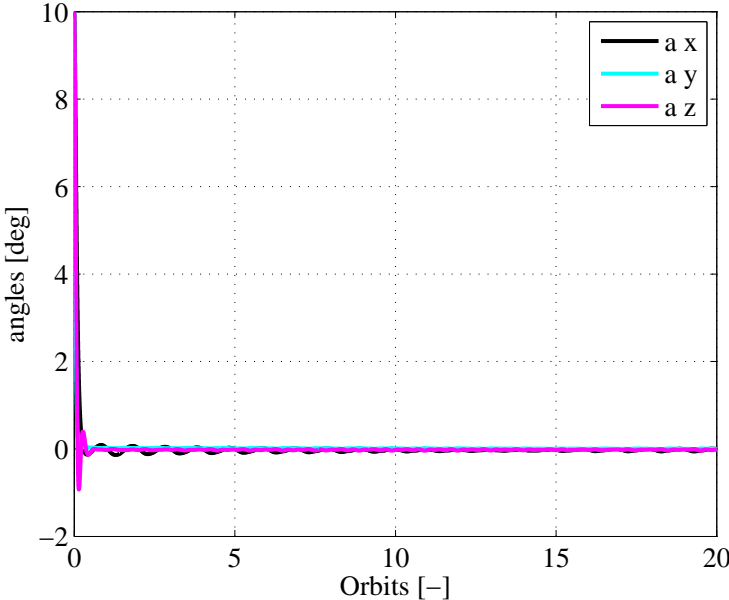


Figure 7.20: Attitude angles  $\alpha$  in the CSD condition..

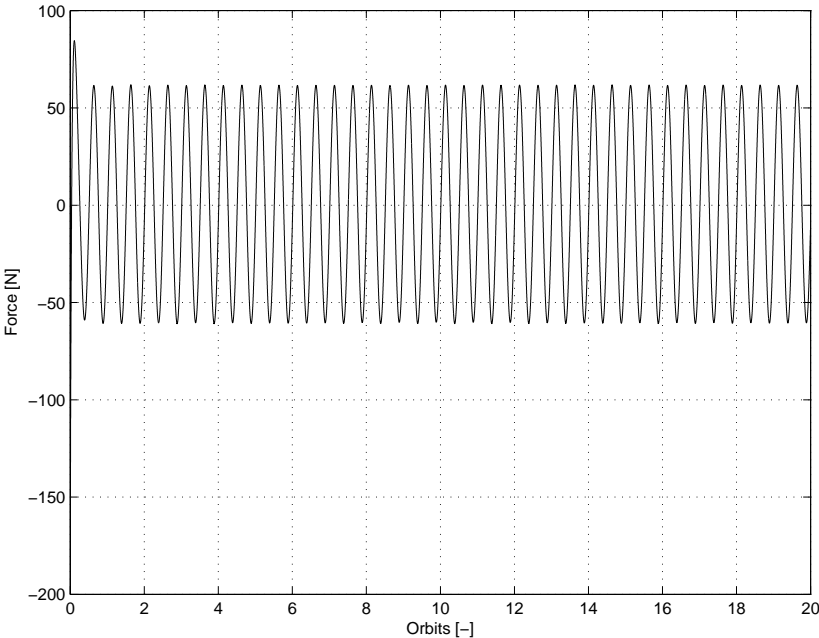
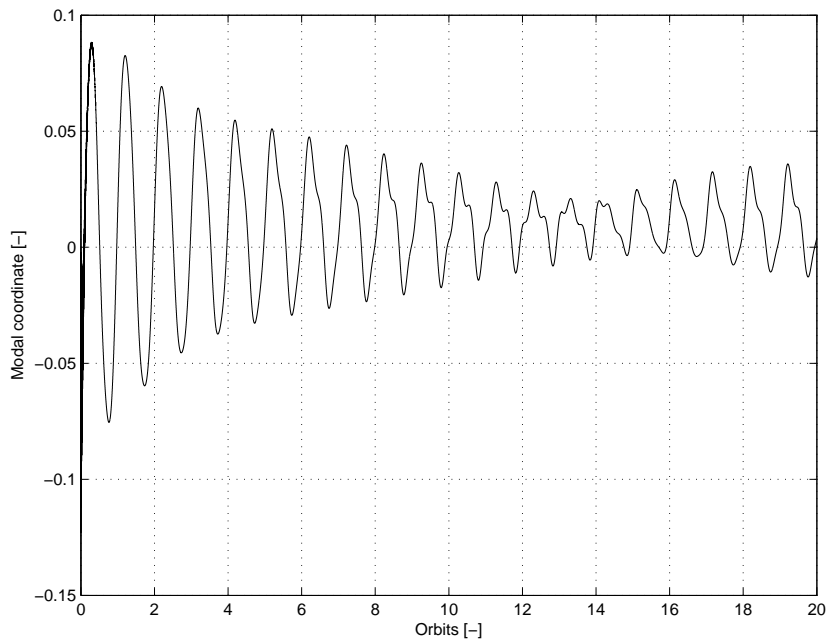
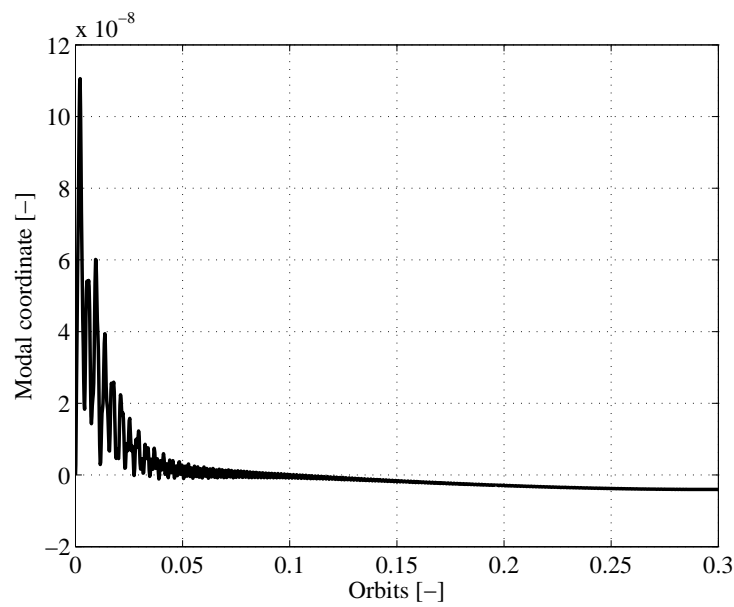


Figure 7.21: Force on the actuator #6 requested for the attitude control in the CSD condition.



**Figure 7.22:** The sixth modal coordinate in the CSD condition.



**Figure 7.23:** The first modal coordinate in the CSD condition, for the initial time interval.

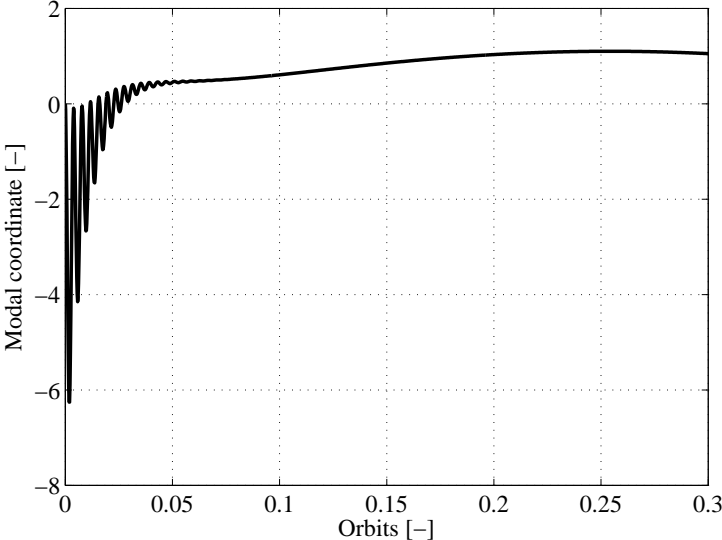


**Figure 7.24:** The second modal coordinate in the CSD condition, for the initial time interval.

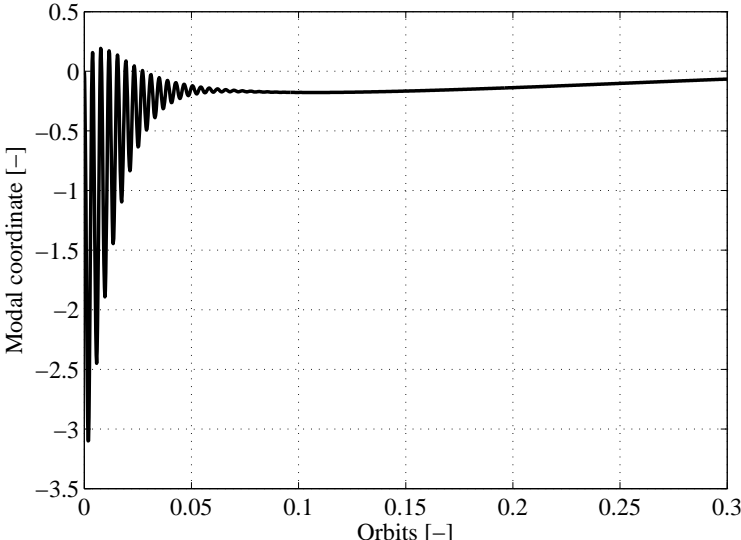


**Figure 7.25:** The third modal coordinate in the CSD condition, for the initial time interval.

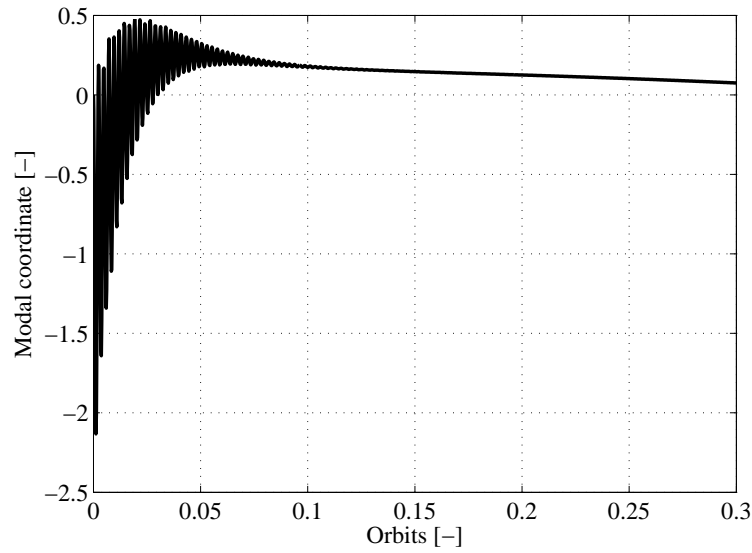


**Figure 7.26:** The fourth modal coordinate in the CSD condition, for the initial time interval.

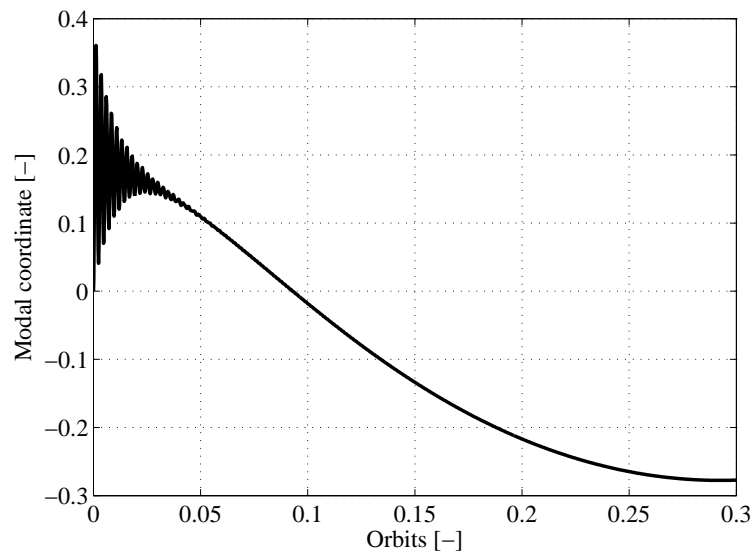


**Figure 7.27:** The fifth modal coordinate in the CSD condition, for the initial time interval.

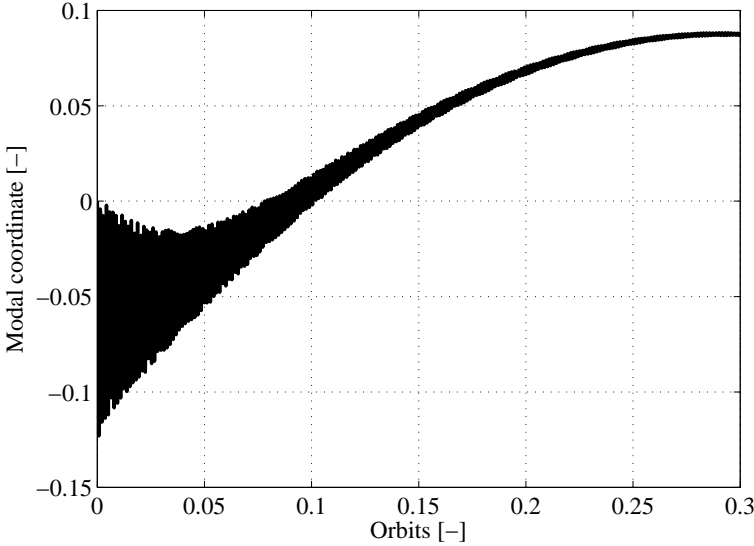


**Figure 7.28:** The sixth modal coordinate in the CSD condition, for the initial time interval.

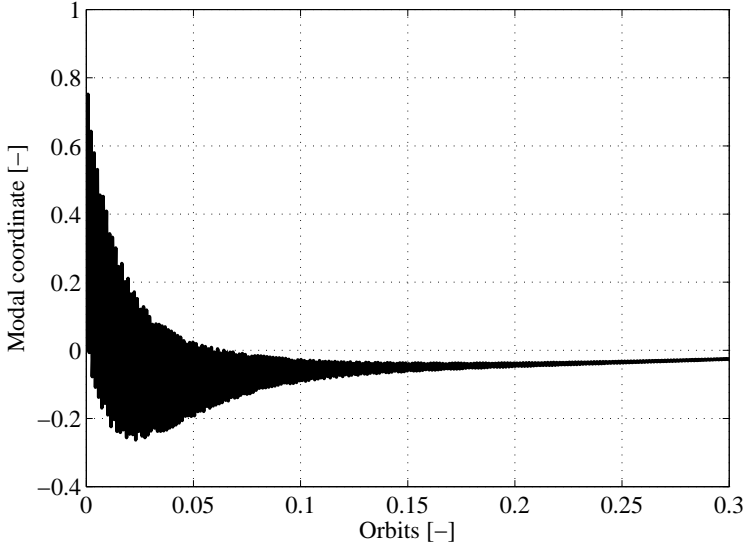


**Figure 7.29:** The seventh modal coordinate in the CSD condition, for the initial time interval.

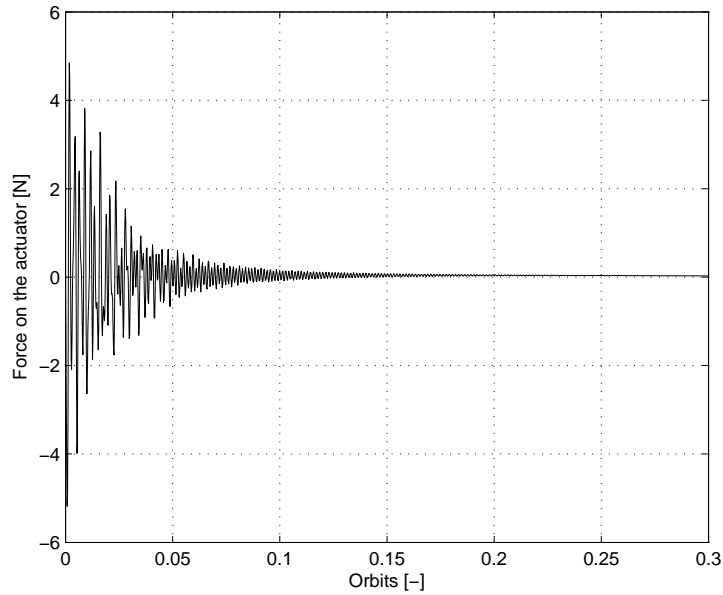


**Figure 7.30:** Force on the #1S actuator in the CSD condition, for the initial time interval.

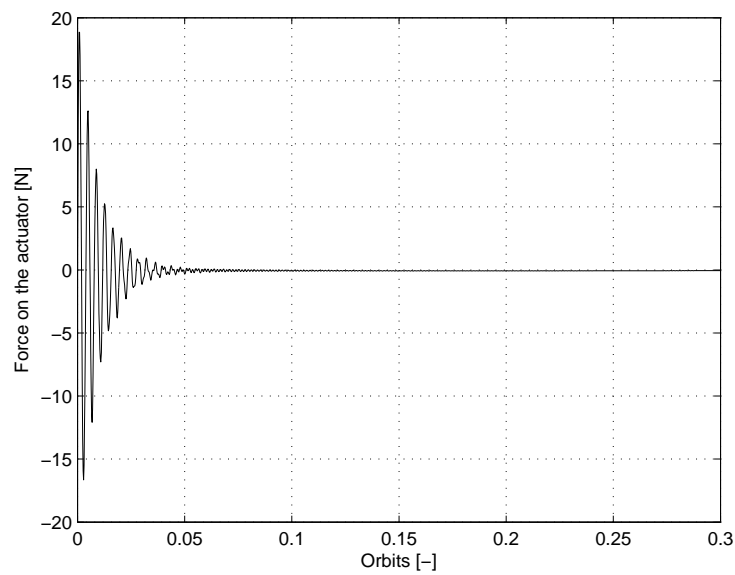


**Figure 7.31:** Force on the #2S actuator in the CSD condition, for the initial time interval.

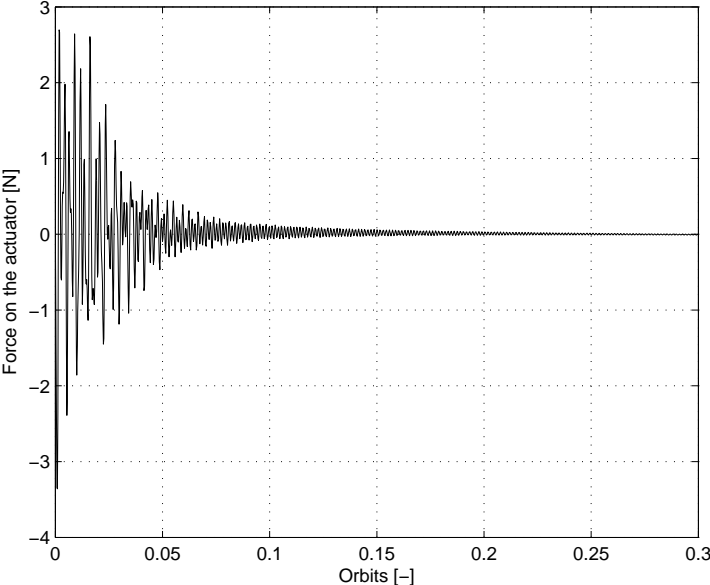


**Figure 7.32:** Force on the #3S actuator in the CSD condition, for the initial time interval.

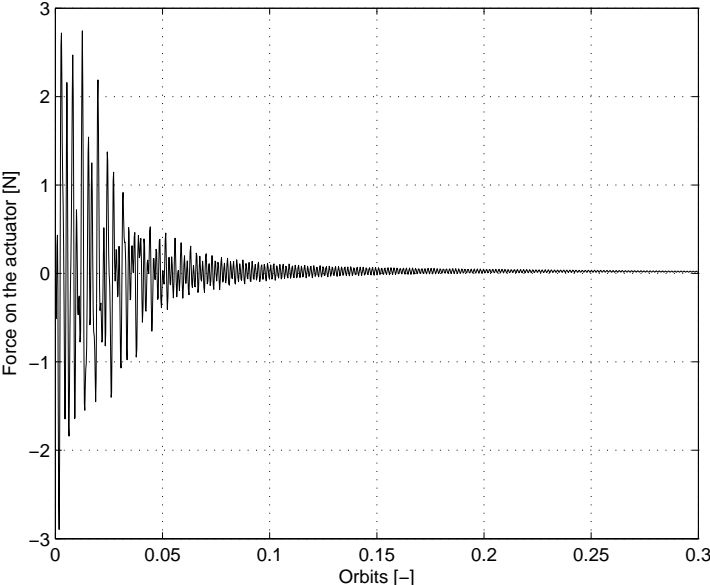


**Figure 7.33:** Force on the #4S actuator in the CSD condition, for the initial time interval.

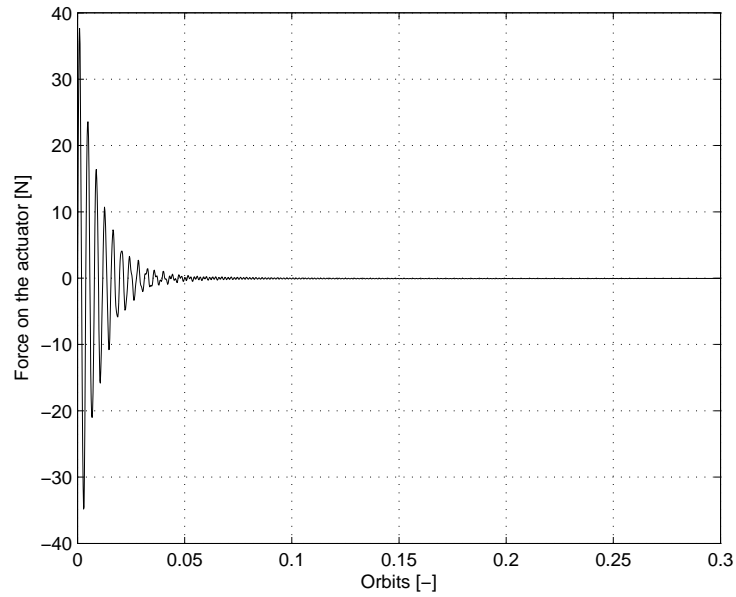


**Figure 7.34:** Force on the #5S actuator in the CSD condition, for the initial time interval.

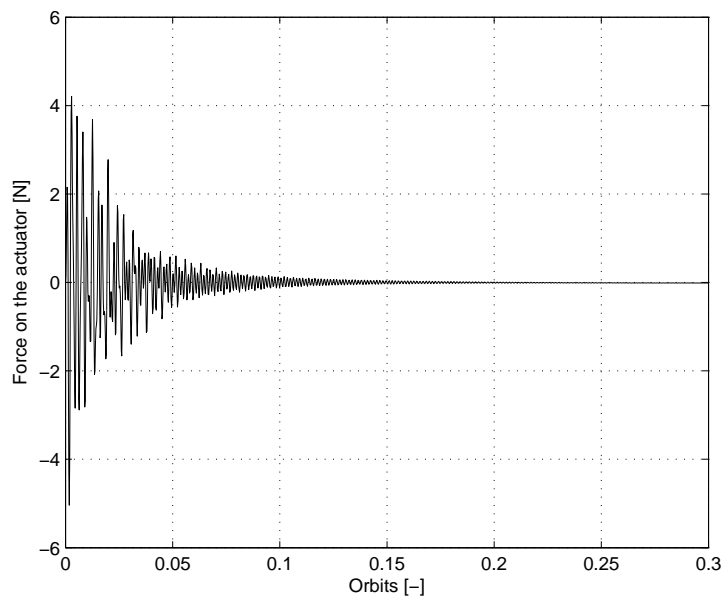


**Figure 7.35:** Force on the #6S actuator in the CSD condition, for the initial time interval.

system has been reasonably selected, the interactions with the neglected dynamics should be further investigated.

# Chapter 8

## Conclusions

### 8.1 Thesis Contributions

The objective of the present work is the study of the problems that may arise due to the interactions between the orbital/attitude control systems of a large flexible spacecraft and its structural vibrations. The reference model is the Abacus Reflector SSP concept, chosen because, thanks to its structural simplicity and high modularity, constitutes the basilar structure for a wider class of SSP concepts. Besides, its simple geometry enables a preliminary study of the behaviour of the structure when designing the orbital and attitude control systems of the satellite.

First of all, taking into account the main perturbing actions acting on a GEO satellite, the orbital and attitude control system has been designed to fulfil realistic requirements regarding the station keeping and pointing accuracies. Since the employment of chemical propulsion devices is unrealistic due to their low specific impulse, it is appropriate to exploit the efficiency of the low-thrust propulsion. It has been proven that a LQR approach for continuous control can maintain the position and the attitude of the satellite within the prescribed limits. The designed control systems utilize the same set of actuators to provide the necessary actions to counteract the external disturbances. As a consequence, the control forces are introduced into the structure and their effects need to be investigated.

To this concern, a FE model of the Abacus-like structure has been developed in order to characterize the modal behaviour of the structure. As expected, the first natural frequencies turn out to be lower than those of the common, much more compact, satellites.

An immediate solution, in order to avoid the interactions with the flexible modes of the structure, can be designing the orbital/attitude control system with a very low bandwidth. One drawback of this approach is that such low bandwidth regulators could not have the necessary authority to execute possible harder manoeuvres during the operational life of the spacecraft. Another disadvantage is the poor ro-

bustness of the whole system under unexpected or unmodelled disturbances which may excite the vibrations of the structure. For this reason, a preliminary study of a vibration suppression system has been carried out.

Since the numerical simulations of dynamical systems, such as FE analysis, usually results in complex high-order dynamic models, it is desirable to approximate them by simpler models with reduced order. For this purpose, several techniques of model reduction has been investigated. The choice has fallen onto the simple modal truncation because it allows the interpretation of the dynamical behaviour of the system in terms of modal coordinates, which give a direct physical insight. For large flexible structures it is unlikely to know the full state vector of the dynamical system. This consideration justifies the recourse to the class of the direct output feedback controllers in which the measures coming from collocated sensors are directly used to provide the feedback control action. The effectiveness of the designed regulator has been demonstrated in two significant situations: the satellite operative condition, and a perturbed initial condition. It has been exhibited that, for both the conditions, two kind of structural oscillations arise from these interactions: large very low frequency oscillations, that are the natural consequence of the structural flexibility due to the nominal trend of the orbit and attitude control force, and much higher frequency vibrations in correspondence to the modal frequencies of the structure. Although the first kind of oscillations present a large amplitude, they are not considered to be dangerous for the structure, while the second kind need to be damped.

It can be shown that, if the vibration suppression system is inactive, some of the modal coordinates are excited and the vibrations remain undamped. On the other hand, it has been proved that when the vibration control is active, those sparked oscillations are extinguished in a time of the order of the orbit, whit affordable actuation forces. Is is to be underlined that the aforementioned vibrations suppression system has been designed considering a reduced order structural model including the first seven flexible modes. Although the order of the reduced system has been reasonably selected, the interactions with the neglected dynamics should be further investigated.

## 8.2 Further Developments

Although the implemented controller are designed to be sufficiently robust with respect to external perturbations, the thermal distortion and structural vibrations due to solar heating need deeper studies. In particular, the thermoelastic interactions appear to be a critical issue in the development of such satellites and definitely deserve a future investigation.

The latter consideration leads to the necessity of refining the FE model of the

structure. This should include a model of the solar arrays and of the huge microwave transmitting system. Moreover, the FE model should be able to compute the stresses and the strains that result in the structure, in order to give precise requirements on the performances requested to the control systems.

A further important aspect that has been not deeply studied is the interactions of the structural system with the rest of the satellite and with the environmental perturbations. Among these, it should be considered a realistic model of the actuation system. In fact, the actuation stations are not punctiform and follow the structure when it is subjected to large vibrations. Thus, the movements of the actuators could potentially affect the performances of the control systems. Besides, the actual dynamics of the actuators and the fact that they cannot be perfectly collocated with sensors should be considered. Concerning the external disturbances, only the environmental quasi-deterministic perturbing forces have been considered. It is worthwhile to take into account possible sources of random, hardly predictable disturbances. Hence, a possible area for future works could be the employment of Linear Quadratic Gaussian (LQG) regulators.

Drawing from the results of the stability and robustness analysis of the direct output feedback controllers, a promising area for future studies may regard the possibility of structuring the gain matrix of such regulators. The selection of the gain matrix among the stabilizing family of positive definite matrices and its parametrization by means, for example, of the Cholesky decomposition, could be the first step leading to a direct numerical optimization exploited to minimize an appropriate performance index. At the same time, the increased controller design freedom given by the parametrization of the gain matrix, allows to impose several other constraints on the behaviour of the closed-loop system, e.g. directly assign the position of significant poles within the complex plane.

# Appendix A

## Electric Propulsion Systems

Electrical propulsion systems are based on accelerating an ionized mass by an electromagnetic or electrostatic field, where the ions leave the thruster nozzle at very high velocity. The common peculiar characteristics shared by the different typologies of electric systems are the high values of specific impulse  $I_{sp}$  and the possibility of adjusting the thrust level. Furthermore, a high  $I_{sp}$  entails a low propellant consumption and the reduction of the mass to take on-board per mission. In particular, minimization of propellant (and tanks) mass is essential for all large-scale space systems, since the amount of propellant and the dimensions of the related propulsion system needed if chemical propulsion was to be employed would be unaffordable. For these reason, in the present work the option of making use of chemical-based propulsion systems is not considered. Naturally, there are also numerous drawbacks concerning electric propulsion. The most awkward of them appear to be that the thrust levels that can be achieved are very low and that high voltages are required. In this section a brief survey of the different electrical thruster categories is given.

### A.0.1 Electrothermal propulsion

The acceleration is achieved heating a propellant gas by electrical heat addition and expanding it through a convergent/divergent nozzle. Resistojet and arcjet propulsion systems belong to this class.

**Resistojet** Resistojets heat propellant using an heated solid surface and have a low specific impulse, ranging from 100 to 400 s.

**Arcjet** Opposite to resistojets, arcjets heat propellant using an electric arc generated between an anode and a catode. They are less efficient at converting power to  $I_{sp}$  (20 to 30%) but higher specific impulses are achievable (500 to 1500 s).

---

## A.0.2 Electrostatic propulsion

It is based on the acceleration of an ionized propellant gas by the application of electric fields. Examples include gridded ion thrusters and Field Emission Electric Propulsion (FEEP).

**Gridded ion thrusters** Propellant atoms (of mercury, xenon or argon vapour) are injected into the ionization chamber where they are bombarded with electrons from a hollow cathode, causing the atoms to lose electrons and become ionized. The side of the exit of the ionization chamber is equipped with two high voltage electrodes that have a grid structure. The high voltage applied to the electrodes accelerates the ions to a high velocity thus forming the thrust beam. Electrons and ions must be injected in the thrust beam in equal numbers to maintain charge neutrality. For this reason electrons are shot from a cathode, called the neutraliser, towards the ions behind the ship to ensure that equal amounts of positive and negative charge are ejected. Neutralizing is needed to prevent the ship from gaining a net negative charge.

Gridded ion thrusters show a very high specific impulse, ranging from 3000 to 8000 s and very high thrust efficiency (more than 60%). Another interesting plus, when the thrusters are employed in a cluster configuration, is the low ion plume divergence, typically about 20°.

The primary performance degradation is due to grid erosion caused by high speed ion impingement on the acceleration grid. The consequent reduction in thrust efficiency and specific impulse due to hole enlargement and plume defocussing is the main lifetime limiting factor.

**FEEP** Thrust is produced by exhausting a beam of mainly singly-ionized caesium atoms, produced by field evaporation. Thrust level very low, ranging from 1 to 100 mN.

## A.0.3 Electromagnetic propulsion

It is based on the acceleration of an ionized propellant gas by the application of both electric and magnetic fields. Examples include Hall thrusters and Magneto-Plasma Dynamic thrusters (MPDT).

**Hall thrusters** Electrons are generated by an external cathode and injected into a dielectric annular chamber. A radial magnetic field is generated between inner/outer poles of magnets. The Lorentz force on electrons crossing radial magnetic field lines causes electron cyclotron motion in chamber, thus they follow a helical path towards the anode. Neutral gas (usually xenon) injected into chamber

collide with electrons.

The acceleration of ions is carried out by the self-established electric field created by the electron current induced by Lorentz force.

Additional electrons are emitted by an external cathode into the ion plume in order to neutralize the ions.

This class of thruster presents relatively low specific impulses, about 2000 s, and lower efficiency with respect to gridded ion thrusters.

The main issue is related with the erosion of ceramic insulation of the dielectric annular chamber. At current development stage, with currently used materials, thruster lifetime is reduced to a few thousands hours.

**MPDT** Ion acceleration is carried out by exploiting electromagnetic Lorentz forces. Very high current axial cathode produces electrons by thermionic emission. High radial electron discharge to anode poles on lip of cylindrical chamber, ionisation of propellant (solid lithium). Self-induced azimuthal magnetic field from high radial electric field causes axial acceleration of ions.

They show good  $I_{sp}$  levels, ranging from 1800 to 8000 s, but the high current needed in the cathode entails a high power level, in the order of the kW. On the other hand the peak thrust level achievable is at least one order of magnitude more than that attainable with the other electric propulsion systems.

The major drawback in employing the Magneto-Plasma thrusters is the high power requirement, due to which at present only experimental models have been developed for laboratory testing.

The electrostatic ion thrusters, in particular gridded ion engines, appear to be a kind of highly-efficient low-thrust propulsion systems running on electrical power that deserve particular attention in the context of this work because they could be the good candidates for geostationary station keeping and attitude control. In Figure A.1 is schematically illustrated the functioning principle of a gridded ion thruster and in Table A.1 are listed the characteristics of the reference thruster considered in this work.

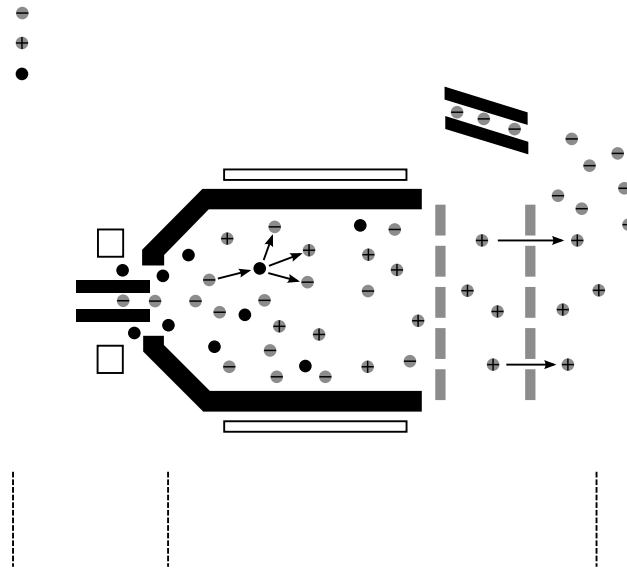


**Figure A.1:** Schematic diagram of an electrostatic ion thruster.

**Table A.1:** Reference electric propulsion system.

Thrust [N]	1
Specific impulse [s]	5000
Exhaust velocity [km/s]	50
Total efficiency [-]	0.8
Power to thrust ratio [kW/N]	30
Mass to power ratio [kg/kW]	5
Total peak thrust [N]	200
Total peak power [MW]	6
Total average thrust [N]	80
Total average power [MW]	2.5

# Appendix B

## Linear System Properties

This section will introduce several concepts and properties associated with linear systems that are of interest of the model reduction problem.

### B.1 Transfer Function Matrix

Considering the state-space representation of the LTI system  $\mathcal{S}$ , as in (5.1), the transfer matrix from  $u$  to  $y$  is defined as

$$Y(s) = G(s)U(s) \quad (\text{B.1})$$

where  $U(s)$  and  $Y(s)$  are the Laplace transforms of  $u(t)$  and  $y(t)$  with zero initial conditions. Hence,

$$G(s) = C(sI_n - A)^{-1}B + D \quad (\text{B.2})$$

Thus, the transfer function matrix provides a frequency domain description of the input-output behaviour of the system  $\mathcal{S}$ .

It can be seen that more than one realization  $(A, B, C, D)$  of  $\mathcal{S}$  can produce the same transfer function  $G(s)$ . That is, different system realizations can produce the same input-output behaviour. In particular, considering the state-space transformation

$$x = Tx' \quad (\text{B.3})$$

with  $T$  a non-singular matrix of dimension  $n \times n$ . Since such a transformation only amounts to rewriting the state variable in a new basis, it does not affect the input-output behaviour associated with  $\mathcal{S}$ . Thus the following can be stated

**Lemma 3.** If  $\mathcal{S}$  is represented as in (5.1), then the input-output behaviour of  $\mathcal{S}$  is equivalently represented by the state-space realization defined by

$$\dot{x}' = T^{-1}ATx' + T^{-1}Bu \quad (\text{B.4a})$$

$$y = CTx' + Du \quad (\text{B.4b})$$

The transformation  $A \rightarrow T^{-1}AT$  is called a similarity transformation of the matrix  $A$ . It has the property of leaving the eigenvalues of the  $A$  matrix invariant.

## B.2 State-Space Models Versus Transfer Functions

The most important differences between the state space representation and the transfer function representation of a given system are (see [Sil71]):

- The transfer function of an LTI system describes the relation between the input and the output of the system under the assumption that the system is initially relaxed (i.e. the initial state is zero). Hence, if this assumption does not hold, the description is not applicable. In contrast to the state space description, the transfer function representation does not reveal what happens if the system is not initially relaxed. For example observable modes can be excited due to a non-zero initial state but may not appear in the transfer function due to pole-zero cancellation.
- The transfer function formulation does not reveal the behaviour inside the system, such as unobservable unstable modes. Therefore, the transfer function matrix cannot always be used to study the stability properties of an LTI system.
- Although most results that are available for MIMO state space descriptions can also be obtained in the transfer function approach, the state space formulation stays the better way of dealing with generalizations like MIMO systems or non-linear systems. Moreover, in practice the state space formulation is very important for numerical computations and modern controller design (cf. Chapter 5 and Chapter 6).

## B.3 Controllability and Observability

**Theorem 4.** *Given a state-space realization of the LTI system  $\mathcal{S}$ , the following statements are equivalent*

- $(A, B)$  is controllable
- The controllability matrix

$$\mathcal{C} = [B \quad AB \quad A^2B \quad \dots \quad A^{n-1}B] \quad (\text{B.5})$$

*has full-row rank*

c) The controllability grammian  $W_c$ , solution of the Lyapunov equation

$$AW_c + W_cA^T + BB^T = 0 \quad (\text{B.6})$$

is positive definite

**Theorem 5.** Given a state-space realization of the LTI system  $\mathcal{S}$ , the following statements are equivalent

a)  $(C, A)$  is observable

b) The observability matrix

$$\mathcal{O} = \begin{bmatrix} C \\ CA \\ CA^2 \\ \vdots \\ CA^{n-1} \end{bmatrix} \quad (\text{B.7})$$

has full-column rank

c) The observability grammian  $W_o$ , solution of the Lyapunov equation

$$A^T W_o + W_o A + C^T C = 0 \quad (\text{B.8})$$

is positive definite

## B.4 Frequency Moments and Markov Parameters

Given a LTI system  $\mathcal{S}$ , its transfer function  $G(s) = C(sI_n - A)^{-1}B + D$ , is expanded in a Fourier power series,

$$G(s) = \sum_{i=0}^{\infty} M_i(j\omega) (s - j\omega)^i \quad (\text{B.9})$$

The matrices

$$M_i(j\omega) = C(j\omega I_n - A)^{-(i+1)} B, \quad i = 0, \dots, \infty \quad (\text{B.10})$$

are known as the low frequency moments of the transfer function  $G(s)$ . The high frequency moments

$$M_i(j\infty) = \lim_{\omega \rightarrow \infty} M_i(j\omega) = CA^i B, \quad i = 0, \dots, \infty \quad (\text{B.11})$$

are also called Markov parameters. It can be shown that the  $i$ -th Markov parameter is associated with the  $i$ -th time derivative of the impulse response at instant zero. Since the frequency moments are input-output properties, they remain invariant under a similarity transformation.

## B.5 Output Correlation and Power Moments

Another quantity related to the input-output behaviour of a linear system is the output correlation for impulsive inputs. It can be shown that it can be computed as

$$\hat{R}(t) = C e^{At} W_c C^T \quad (\text{B.12})$$

The output covariance can be Laplace transformed and expanded in a Fourier series obtaining

$$\hat{R}(s) = C (sI_n - A)^{-1} W_c C^T = \sum_{i=0}^{\infty} R_i(j\omega) (s - j\omega)^i \quad (\text{B.13})$$

The matrices

$$R_i(j\omega) = C (j\omega I_n - A)^{-(i+1)} W_c C^T, \quad i = 0, \dots, \infty \quad (\text{B.14})$$

are known as the low frequency power moments. The high frequency power moments

$$R_i(j\infty) = \lim_{\omega \rightarrow \infty} R_i(j\omega) = C A^i W_c C^T, \quad i = 0, \dots, \infty \quad (\text{B.15})$$

are also called covariance parameters. As the frequency moments, being also the frequency power moments input-output properties of the system  $\mathcal{S}$ , they remain invariant under a similarity transformation.

## B.6 $\mathcal{H}_2$ and $\mathcal{H}_\infty$ Norms

Let  $G(s) \in \mathcal{L}_2$ , the  $\mathcal{L}_2$  norm of  $G$  is defined as

$$\|G\|_2^2 = \frac{1}{2\pi} \int_{-\infty}^{\infty} \text{tr}(G^*(j\omega) G(j\omega)) d\omega \quad (\text{B.16})$$

It is worth noticing that the  $\mathcal{L}_2$  norm defined previously is finite iff the transfer matrix  $G$  is strictly proper, that is  $G(\infty) = 0$ . Although  $\|G\|_2$  can be computed from its definition (B.16), it is useful to have an alternative characterization of this norm to take advantage of the state-space representation of  $G$ .

**Lemma 4.** Given the transfer matrix of a strictly proper system

$$G(s) = \begin{bmatrix} A & B \\ C & 0 \end{bmatrix} \quad (\text{B.17})$$

then the  $\mathcal{L}_2$  norm of  $G$  can be computed as

$$\|G\|_2^2 = \text{tr}(B^* W_o B) = \text{tr}(C W_c C^*) \quad (\text{B.18})$$

where  $W_o$  and  $W_c$  are the observability and controllability grammians.

Another norm of interest is the  $\mathcal{H}_\infty$  norm, defined as

$$\|G\|_\infty := \sup_{\omega} \bar{\sigma}\{G(j\omega)\} \quad (\text{B.19})$$

where  $\bar{\sigma}(G)$  is the largest singular value of  $G$ . For SISO systems, a simple interpretation of the  $\mathcal{H}_\infty$  norm of a system can be given. For these systems the infinity norm of the scalar transfer function  $G$  appears as the peak value on the Bode magnitude plot of  $|G(j\omega)|$ .

# Acronyms

**LAST** Local Apparent Sidereal Time

**GAST** Greenwich Apparent Sidereal Time

**GMST** Greenwich Mean Sidereal Time

**UT** Universal Time

**UTC** Coordinated Universal Time

**RFCS** Reference Frame and Coordinate System

**ECI** Earth Centered Inertial

**ECEF** Earth Centered Earth Fixed

**GCW** Geostationary Clohessy-Wiltshire

**COEs** Classical Orbital Elements

**EOEs** Equinoctial Orbital Elements

**GEO** Geostationary Earth Orbit

**LQR** Linear Quadratic Regulator

**ARE** Algebraic Riccati Equation

**VOP** Variation Of Parameter

**LQG** Linear Quadratic Gaussian

**EEM** Euler Equation of Motion

**LQ** Linear Quadratic

**SSP** Space Solar Power

**BCSP** Body Centered Sun Pointing  
**BCSF** Body Centered Sun Facing  
**ECSF** Earth Centered Sun Facing  
**BPI** Body Principal Inertial  
**SP** Sun Pointing  
**SF** Sun Facing  
**AR** Abacus Reflector  
**EEM** Euler Equations of Motion  
**PID** Proportional Integrative Derivative  
**APIC** Attitude Perturbed Initial Condition  
**AZIC** Attitude Zero Initial Condition  
**ITP** Independent Transmitter Pointing  
**OART** One Axis Rotating Transmitter  
**LEO** Low Earth Orbit  
**MEO** Medium Earth Orbit  
**ARF** Abacus Reflector  
**STW** Solar Tower  
**TSP** Tethered Solar Power  
**SL** Structural Local  
**SG** Structural Global  
**FE** Finite Element  
**USD** Uncontrolled Structural Dynamics  
**CSD** Controlled Structural Dynamics  
**ZIC** Zero Initial Conditions  
**PIC** Perturbed Initial Conditions



# Bibliography

- [A<sup>+</sup>10] K. T. Alfriend et al. *Spacecraft Formation Flying*. Elsevier Ltd., 2010.
- [ASG] A. C. Antoulas, D. C. Sorensen, and S. Gugercin. A survey of model reduction methods for large-scale systems. In *AMS-IMS-SIAM Summer Research Conference on Structured Matrices*.
- [BB94] El Ghaoui L. Feron E. Boyd, S.P. and V. Balakrishnan. *Linear Matrix Inequalities in Systems and Control Theory*. SIAM, 1994.
- [BC71] R. A. Broucke and P. J. Cefola. On the equinoctial orbit elements. *Celestial Mechanics*, 1971.
- [CL] F. Casella and M. Lovera. High-accuracy orbital dynamics simulation through keplerian and equinoctial parameters. In *Modelica Conference 2008*.
- [coo]
- [dep79] Satellite power systems (sps), concept development and evaluation program, preliminary assessment. Technical report, U.S. Department of Energy, 1979.
- [DS00] B. De Schutter. Minimal state-space realization in linear system theory: an overview. *Journal of Computational and Applied Mathematics*, 2000.
- [dVS87] C. de Villemagne and R. E. Skelton. Model reductions using a projection formulation. *International Journal of Control*, 1987.
- [FC03] H. Feingold and C. Canington. Evaluation and comparison of space solar power concepts. *Acta Astronautica*, 2003.
- [GL94] M. Green and D. J. N. Limebeer. *Linear Robust Control*. Pearson Education, Inc., 1994.
- [Gla68] P. E. Glaser. Satellite solar power station. *Solar Energy*, 1968.

- [JK93] J. L. Junkins and Y. Kim. *Introduction to Dynamics and Control of Flexible Structures*. AIAA Education Series, 1993.
- [Jos89] S. M. Joshi. *Control of Large Flexible Space Structures*. Springer-Verlag, 1989.
- [Kai80] T. Kailath. *Linear Systems*. Prentice-Hall, 1980.
- [Kap81] G. H. Kaplan. The IAU Resolutions on Astronomical Constants, Time Scales, and the Fundamental Reference Frame. Technical report, United States Naval Observatory, 1981.
- [Los07] D. Losa. *High vs Low Thrust Station Keeping Maneuver Planning for Geostationary Satellites*. PhD thesis, École Nationale Supérieure des Mines de Paris, February 2007.
- [LQ03] G. R. Liu and S. S. Quek. *The Finite Element Method: A Practical Course*. Butterworth Heinemann, 2003.
- [M<sup>+</sup>88] J. G. Marsh et al. A New Gravitational Model for the Earth from Satellite Tracking Data: GEM-T1. *Journal of Geophysical Research*, 1988.
- [Man97] J. C. Mankins. A fresh look at space solar power: New architectures, concepts and technologies. *Acta Astronautica*, 1997.
- [Man99] J. C. Mankins. A technical overview of the suntower solar power satellite concept. *Acta Astronautica*, 1999.
- [NC05] T. S. No and Jung O. C. Analytical Solution to Perturbed Geosynchronous Orbit. *Acta Astronautica*, 56, 2005.
- [PC93] J. E. Prussing and B. A. Conway. *Orbital Mechanics*. Oxford University Press, 1993.
- [Sas06] S. Sasaki. A new concept of solar power satellite: Tethered-sps. *Acta Astronautica*, 2006.
- [Seb04] W. Seboldt. Space- and earth-based solar power for the growing energy needs of future generations. *Acta Astronautica*, 2004.
- [Sil71] L. M. Silverman. Realization of linear dynamical systems. *IEEE Transactions on Automatic Control*, 1971.
- [Val01] D. A. Vallado. *Fundamentals of Astrodynamics and Applications*. Microcosm Press and Kluwer Academic Publishers, 2001.

## BIBLIOGRAPHY

---

- [Wer99] J. R. Wertz. *Spacecraft Attitude Determination and Control*. Microcosm Inc., Torrance CA, 1999.
- [WR01] B. Wie and C. M. Roithmayr. Integrated Orbit, Attitude, and Structural Control Systems Design for Space Solar Power Satellites. Technical report, National Aeronautics and Space Administration, 2001.